Dense Gas, Massive Stars, and Ionising Radiation:

Simulating Stellar Feedback in Spiral-Arm Molecular Clouds

Thomas J. R. Bending

Submitted by Thomas Bending to the University of Exeter as a thesis for the degree of Doctor of Philosophy in Physics, December, 2020.

I certify that all material in this thesis which is not my own work has been identified and that no material has previously been submitted and approved for the award of a degree by this or any other University.

Signed: .....

T. J. R. Bending

Date: 24/07/2021

Abstract

Star formation (SF) has been continuous since the Universe was 200 million years old. It occurs in the interstellar medium (ISM) – the gas and dust between stars within galaxies. The majority of SF occurs inside giant molecular clouds (GMCs) – the most massive agglomerations of dense gas within the ISM – typically the stars form in clusters. Initially the SF is governed solely by a GMC's morphology, but, as stars form, the energy and momentum they inject into their surroundings – stellar feedback – affects ongoing SF within the GMC. The effects of this feedback not only help to break up the cloud, but affect the wider ISM, and hence influence both neighbouring GMC evolution and future GMC formation.

This thesis explores how two forms of stellar feedback – photoionisation and supernova (SN) – affect Milky Way-like spiral arm regions through the use of numerical hydrodynamic simulations. The numerical initial conditions are created by extracting a 500 pc^2 region from simulations of whole galaxies. This means the simulations begin with a 'realistic' arrangement of neighbouring GMCs. The ISM is affected by the warm (10^4 K) HII regions that form and expand around massive photoionising stars and the hot (10^6 K) SNe ejecta that are emitted from the same stars at the end of their lifetimes.

In these simulations photoionisation breaks GMCs and the denser clumps in their substructure up into a larger number of objects while, at the same time, increasing the total mass of dense ISM. This results in more rapid, and partially displaced, SF when compared with simulations without stellar feedback. The main cause of these effects is the compression of dense, but non-star forming, gas from multiple sides by HII regions. SNe have little effect on SF on spiral arm scales. However, SNe are able to heat large regions of the ISM to high temperatures, but only if the gas has already been exposed to photoionising feedback.

Contents

List of Figures

List of Tables

Declaration

This thesis contains the majority of a paper for which I am the first author (Bending, Dobbs & Bate, 2020). My own work from this paper is integrated throughout Chapters 1 to 4. Section 2.3.3 was written predominantly by Matthew Bate. Chapter 5 will form the basis for a future paper.

The numerical simulations were performed using the smoothed particle hydrodynamics code SPHNG (Benz, 1990; Benz, Bowers, Cameron & Press W.H., 1990; Bate, Bonnell & Price, 1995; Price & Monaghan, 2007). It has been modified for galactic scales (Dobbs, Bonnell & Pringle, 2006; Dobbs, Glover, Clark & Klessen, 2008). The column density figures throughout the thesis were made using SPLASH (Price, 2007).

I acknowledge the use of the University of Exeter high-performance computing (HPC) facility (ISCA) in carrying out the no feedback simulations. The photoionisation simulations were performed using the DiRAC Data Intensive service at Leicester, operated by the University of Leicester IT Services, which forms part of the STFC DiRAC HPC Facility (www.dirac.ac.uk). The equipment was funded by BEIS capital funding via STFC capital grants ST/K000373/1 and ST/R002363/1 and STFC DiRAC Operations grant ST/R001014/1. DiRAC is part of the National e-Infrastructure.

Acknowledgements

Thank you to my supervisor Clare. I have endlessly meandered, and sometimes lost my way completely, and she has continuously nudged me in sensible directions without ever making me feel blinkered. She has had enormous patience with me, particularly regarding deadlines. I am proud of what I have achieved, but I would not have got very far without her guidance.

Thank you to Matthew Bate for completing a photoionising feedback algorithm at a convenient moment, for spending the time to make it available, and for always being willing to answer questions while I was getting to grips with it. Also for giving me confidence when I made my first attempt at writing parallelised code.

I also need to thank James Wurster and Pablo who taught me smoothed particle hydrodynamics by answering hundreds of questions between them. Thank you to Adam, Aarynn, Brendan and Mark for always being willing to drop everything and share their hard won skills and knowledge during our two years of isolation downstairs, and for teaching me the power of branding. Thank you to Martin, Krisztian, and Dave for teaching me how to use computers in so many new ways and for keeping them functioning. Thank you to Anna for assisting my move back into academia and teaching me a little about observational astrophysics. Thank you to Emma for so often helping me understand mystical University procedures. And finally, thank you to everyone in the astrophysics group for their part in making it such a relaxed and vibrant place to work.

Finally thank you to my family, firstly to my parents who have provided me with unending support through life even though I have caused them many headaches. Without this I would not have been able to take my wayward route to a PhD. I apologise to my children for the evenings I have been absent and those on which I have been grumpy and poor company. I thank them for (nearly) always having such positive energy and a sense of fun when my own has ebbed. Most importantly thank you to my wife Catherine for her stoic support throughout, particularly in the very difficult final 9 months.

List of acronyms

AMR	adaptive mesh refinement
CNM	cold neutral medium
CSM	circumstellar medium
FUV	far-ultraviolet
GMC	giant molecular cloud
GPU	graphics processing unit
HIM	hot ionised medium
HPC	high-performance computing
IF	ionisation front
IMF	initial mass function
ISM	interstellar medium
ISRF	interstellar radiation field
MPI	message passing interface
PDF	probability distribution function
SF	star formation
SFE	star formation efficiency
SFR	star formation rate
SN	supernova
SNR	supernova remnant
SPH	smoothed particle hydrodynamics
UV	ultraviolet
WIM	warm ionised medium
WNM	warm neutral medium
YSO	young stellar object

Chapter 1

Introduction

This thesis explores the complex relationship between massive stars and the environment in which they form, through the use of numerical hydrodynamic simulations. We do this by considering how photoionising feedback and supernovae (SNe) affect neighbouring giant molecular clouds (GMCs), the star formation (SF) within them and the wider interstellar medium (ISM).

Hence in this introduction we will discuss the nature of the ISM (Section 1.1), GMCs themselves (Section 1.2), aspects of the process of SF within them (Section 1.3), and stellar feedback (Sections 1.4 to 1.6).

The details of numerical simulations are described in Chapter 2, along with motivations for the choice of computer code. How photoionisation affects SF is covered in Chapter 3, its effect on the ISM in Chapter 4, and the impact of SNe in Chapter 5.

1.1 The interstellar medium

The Milky Way has a mass of ~$10^{11} M_\odot$: ~$5 \times 10^{10} M_\odot$ stars, ~$5 \times 10^{10} M_\odot$ dark matter, and ~$7 \times 10^9 M_\odot$ interstellar gas (Draine, 2011). Of this gas ~70% by mass and ~90% by number is hydrogen, the remainder being predominantly helium. The next most abundant element accounts for no more than 0.1% by number. Of the hydrogen ~60% is atomic (HI), ~20% molecular (H_2), and ~20% ionised (H^+). The ISM is made up of the interstellar gas and a dust component ~1% of the gas mass. The dust, also known as solid grains, is made up of small solid particles mostly less than 1 μm across. The ISM may only account for a few percent of the Galaxy by mass but it provides the landscape for the work in this thesis.

While this work is predominantly interested in simulations of Milky Way-like

star forming regions, our understanding of the local ISM is coloured by observations of other local galaxies. Much of what we know about the Milky Way is learned from nearby galaxies.

1.1.1 Early history

At the turn of the 20$^{\text{th}}$ century the Milky Way was predominantly considered to be made up of stars in vacuum. Although observations of nebulae, such as Orion and Pleiades, had been made (Huggins & Miller, 1864; Keeler, 1899), they were not well understood and were considered as distinct objects bounding the vacuum.

The earliest evidence to disprove this vacuum came from discrepancies in the H and K Calcium lines seemingly produced by the binary star δ Orionis (Hartmann, 1904). These lines have constant wavelengths over time unlike the rest of the lines in the spectrum that oscillate with the binary system; the radial velocities of these lines are consistent with Galactic rotation. The strength of the calcium lines also increases with distance (Plaskett & Pearce, 1930), suggesting that the lines are not produced in or around the binary system. This was further confirmed by Trumpler (1930) who identified non-linearity between diameters and photometric distances for a sample of 100 open clusters.

Initially it was assumed that the ISM was uniform throughout the Galaxy. However, Beals (1936) showed that the h and k calcium lines could be made up of multiple components. Sanford, Merrill & Wilson (1938) showed the same for another set of stationary lines, the sodium D1 and D2 lines. These were the first pieces of evidence to suggest that the ISM was in fact far more complex, being made up of clouds with varying radial velocities.

It is now known that the ISM is a highly complex entity with large variations in temperature and kinetic energy throughout. The rest of this section deals with how this gas is arranged in such a way as to be ready to form new stars, and the role dust plays. First we look at some observational techniques for identifying the three forms of hydrogen (Section 1.1.2), then at the distinct phases that exist throughout the ISM (Section 1.1.3). Lastly we summarise the heating and cooling processes, the balance between which defines the properties of the phases (Section 1.1.4). The formation of dense molecular gas and the nature of the GMCs it forms is addressed in Section 1.2.

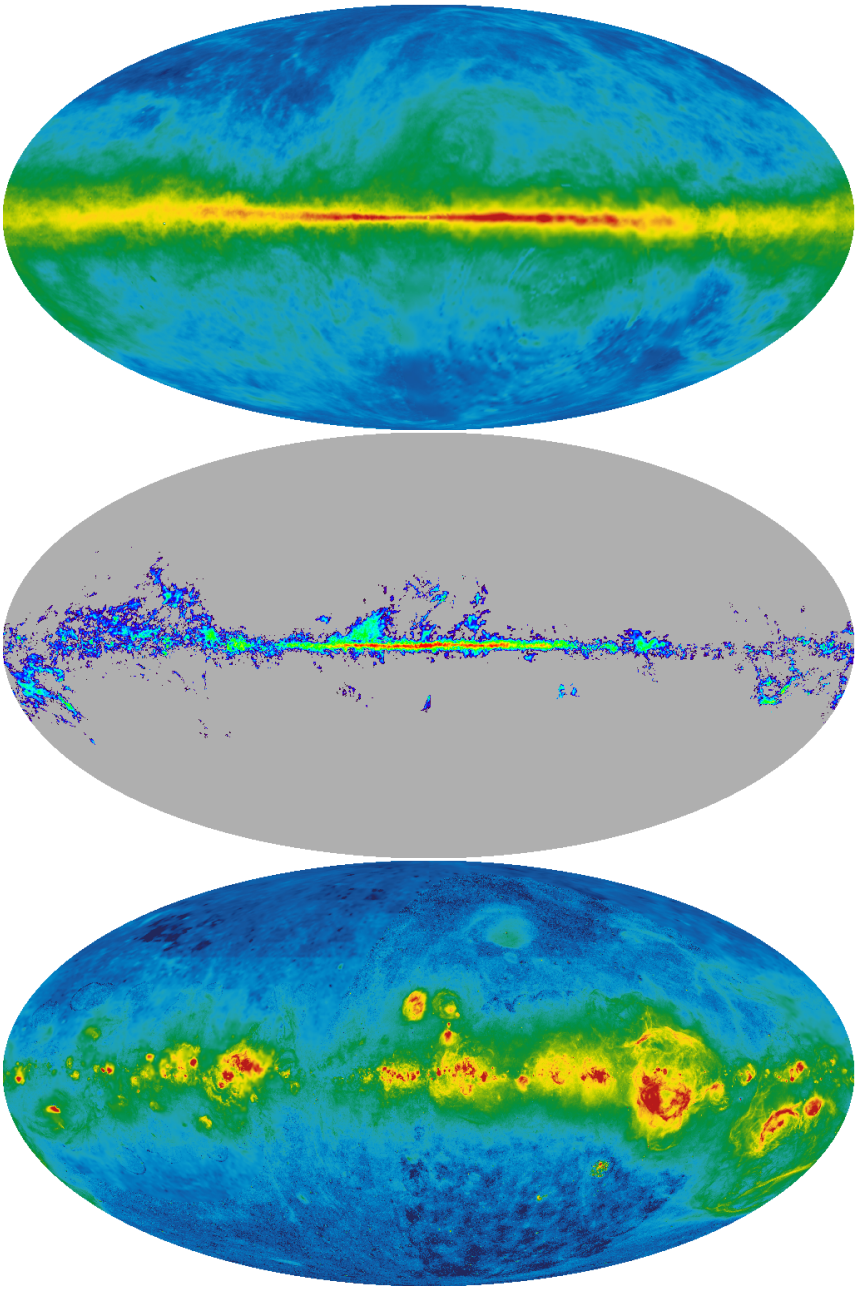

Figure 1.1. Top: 21 cm line map produced from the surveys of Dickey & J (1990) and Hartmann & Burton (1997). Indicates the abundance of HI. Middle: CO 115 GHz line map, composite of 37 surveys compiled by Dame et al. (2001). Bottom: Hα map combining data from WHAM, VTSS, and SHASSA, compiled by Finkbeiner (2003). All three of these images are versions from the Legacy Archive for Microwave Background Data Analysis (LAMBDA), part of the High Energy Astrophysics Science Archive Center (HEASARC). HEASARC/LAMBDA is a service of the Astrophysics Science Division at the NASA Goddard Space Flight Center.

1.1.2 Observing the ISM

A summary of all the most pivotal observations of the ISM is beyond the scope of this thesis. Here we set out to describe the most common ways in which the three forms of hydrogen in the ISM are observed.

21 cm hyperfine emission from HI was the first spectral line to be observed at a radio frequency (Ewen & Purcell, 1951; Muller & Oort, 1951). The line arises due to the energy difference between hydrogen atoms with spin alignment or dis-alignment between the proton and electron. It was first predicted by van de Hulst (1945) and formulae for its derivation can be found in English in Wild (1952). While it is a rare transition, for observing neutral hydrogen, it is an incredibly powerful tool owing to its position in the radio and the large distances that HI spans across the Galaxy. The top panel of Figure 1.1 shows that HI is found throughout the Milky way with a strong correlation to distance from the Galactic mid-plane.

Molecular hydrogen (H_2) is much harder to observe owing to the fact that all of its transitions are either highly improbable or require high energies. This means that H_2 is practically 'invisible' at low temperatures, which is a problem since it requires low temperatures to form at significant concentrations. H_2 is found mostly through detection of other molecular species, the most common being ^{12}CO. The rotational J $= 1 \rightarrow 0$ line at 115 GHz is a frequently used tracer, first observed by Wilson, Jefferts & Penzias (1970). Since then many other molecular species have been detected. Using tracers is not a simple approach due to the difficulty in determining the relative abundance of a given molecular tracer to molecular hydrogen. The middle panel of Figure 1.1 shows that molecular gas is limited to the Galactic midplane and densities fall off far more rapidly than HI at radii of less than 10 kpc.

Ionised hydrogen (H^+) is the most easily observed component of ISM hydrogen. The most well known method is the Hα line corresponding to the Balmer series transition from n=3 $\rightarrow$ 2. Photons from transitions to n=1, the Lyman series, are re-absorbed by the ISM and hence not useful. Hα is the brightest spectral line in the visible spectrum and so has a rich history in astronomy. The bottom panel of Figure 1.1 is an all sky Hα image showing that there is some ionised hydrogen along every line of sight. H^+ can also be identified in the radio thanks to free-free emission (Bremsstrahlung) from decelerated electrons.

The observations presented in Figure 1.1 give a solid picture of the vertical and radial distribution of each form of hydrogen in the Milky Way, however, to get a better idea of the clumping of gas in the x-y plane, observations of other galaxies are more useful. Leroy et al. (2008) did this at resolutions high enough to isolate

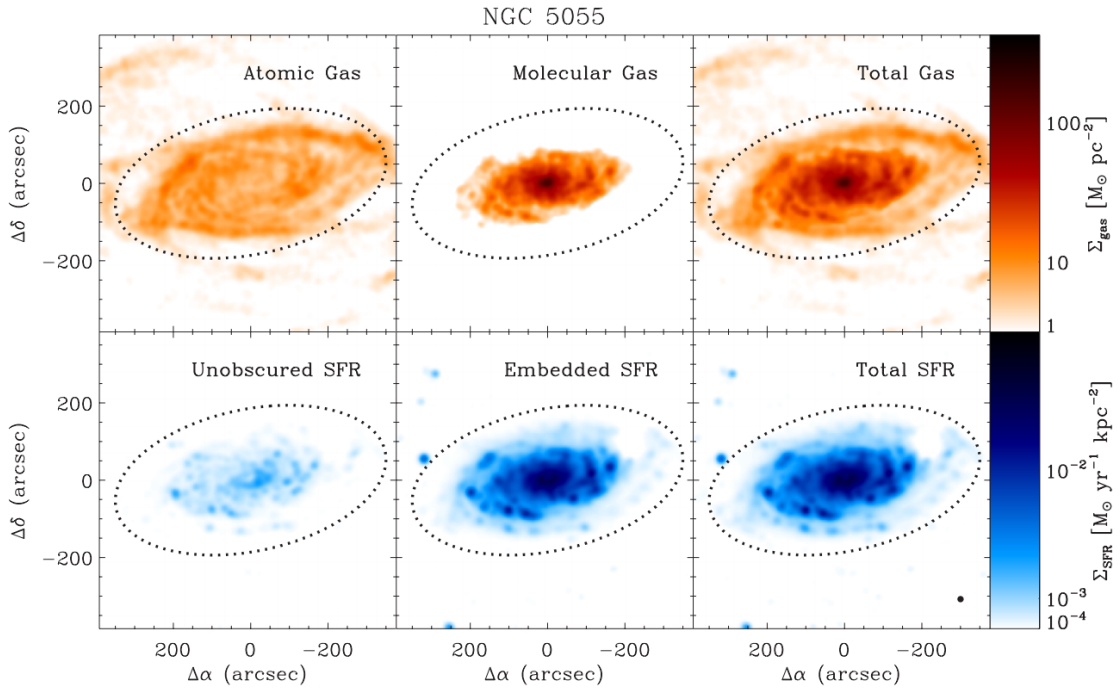

Figure 1.2. Top panel: surface density of atomic and molecular hydrogen for NGC 5055 (The sunflower galaxy - M63). Bottom panel: star formation rates (SFRs) at equivalent locations. Taken from Leroy et al. (2008)

the GMC complexes for a number of galaxies, Figure 1.2 shows their results for NGC 5055. The atomic and molecular gas frames in Figure 1.2 are produced from observations of the same lines described above using the BIMA and THINGS surveys (Helfer et al., 2003; Walter et al., 2008). However, they are more interested in SF than ionised gas, so they use far-ultraviolet (FUV) data from the GALEX survey (Gil de Paz et al., 2007) and infrared data from the SINGS survey (Kennicutt et al., 2003) instead of Hα.

While star formation does often correlate with ionised gas, as discussed further in Section 1.4, this is not always the case. FUV is therefore a better tracer of unobscured star formation since O-type stars output the majority of Ultraviolet (UV) radiation produced by star forming galaxies, and since they are so short lived they can always be associated with star forming regions. However, much UV radiation is unable to escape the dense regions where SF occurs so infrared observations are used to identify the gas that is affected by SF within.

GLIMPSE (Galactic Legacy Infrared Mid-Plane Survey Extraordinaire, Benjamin et al., 2003; Churchwell et al., 2009) is an example of an infrared survey of the Milky way, with one of its main goals being to improve understanding of star formation. It is a survey of the inner Milky Way using the Spitzer Space Telescope at 4 wavelengths

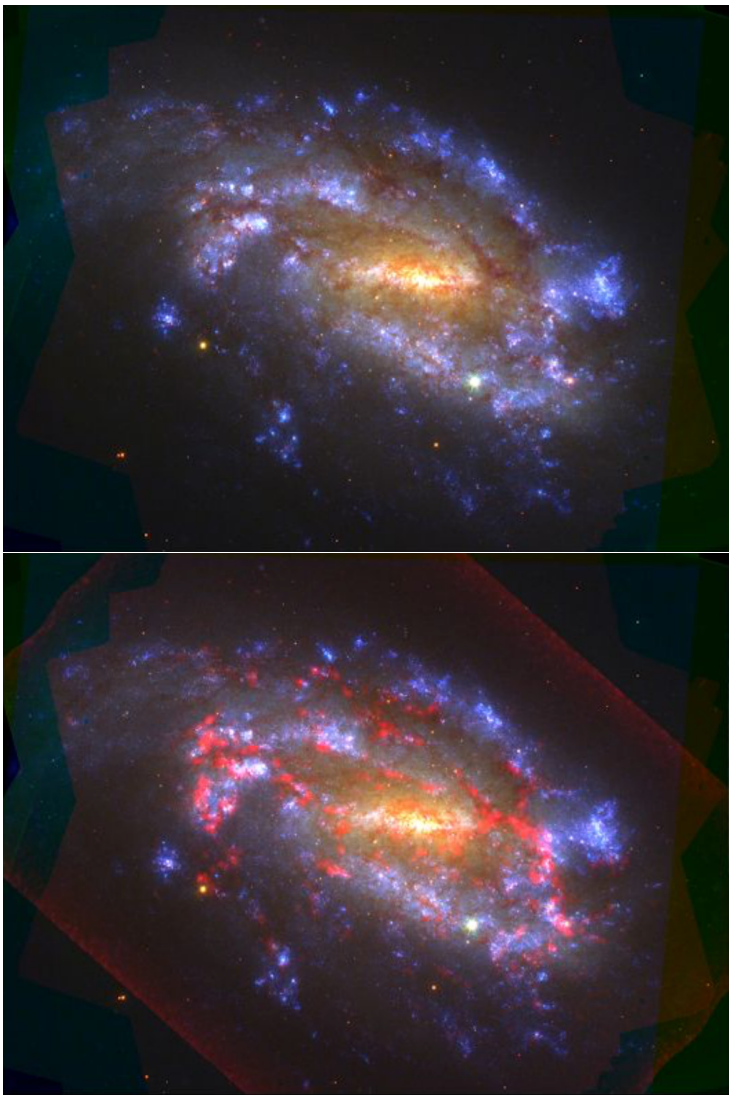

Figure 1.3. PHANGS images of NGC1559 (Schinnerer et al., 2019). Top panel: optical light from PHANGS-HST, near UV in blue, and infrared H band in green. Bottom panel: molecular gas found using PHANGS-ALMA observations overlayed onto top panel.

(3.6, 4.5, 5.8, and 8 μm), 72 million stars from the survey have been catalogued. Most recently the PHANGS collaboration (Physics at High Angular resolution in Nearby GalaxieS) has been able to identify individual GMCs in other galaxies. We discuss GMCs in some detail in Section 1.2. The collaborations main aim is to link young stars with molecular gas by imaging nearby galaxies using HST and ALMA, see Figure 1.3.

1.1.3 Phases of the ISM

The ISM is considered to be made up of multiple distinct phases which arise predominantly as a result of the relative significance of many heating and cooling processes

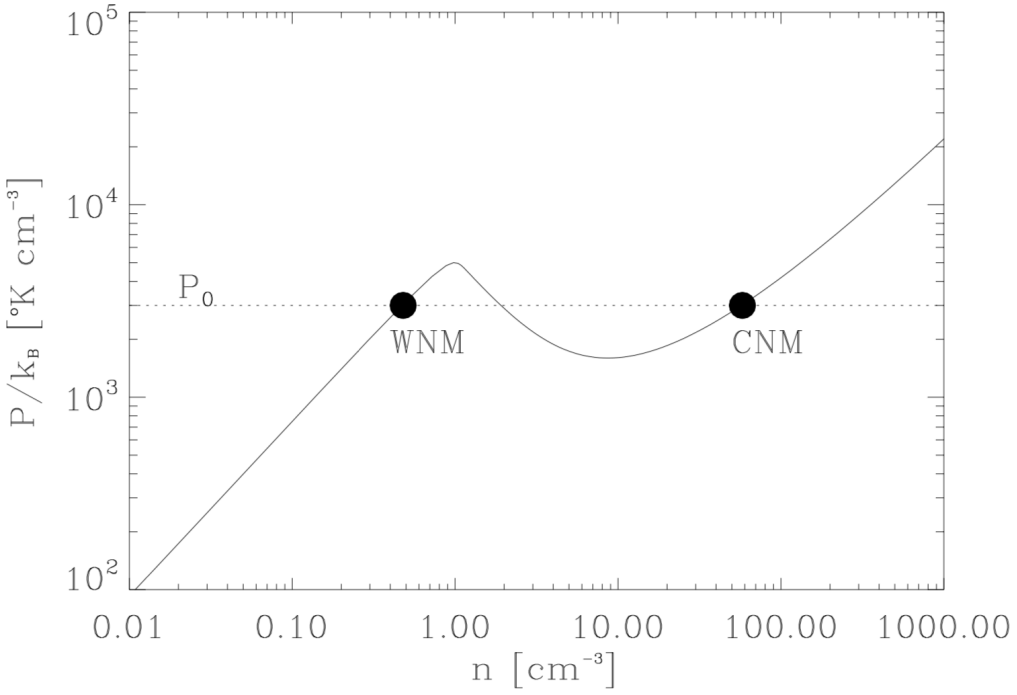

Figure 1.4. Formation of a two phase ISM: the thermal pressure at which heating and cooling processes in the atomic ISM are in equilibrium as a function of gas density, taken from Vázquez-Semadeni (2012). The heating and cooling function used is described in Koyama & Inutsuka (2002). P_0 represents some mean ISM pressure; if this value falls between the maxima and minima, two distinct phases of gas, the warm and cold neutral media, form in pressure balance.

at a variety of densities and temperatures. This concept of a multi-phase ISM began as a two phase model proposed by Clark (1965) and Field, Goldsmith & Habing (1969), in which the ISM is considered to consist of distinct regions of cold ($\approx$ 100 K) and warm ($\approx$ 8000 K) neutral gas in pressure balance, these are known as the cold neutral medium (CNM) and warm neutral medium (WNM) respectively. Figure 1.4 shows how this two phase medium forms as a result of the pressure at which heating and cooling in the ISM is balanced, as a function of density.

The reality is more complex with significant amounts of ionised gas and molecular gas also observed as discussed in Section 1.1.2. The ionised gas typically has temperatures of 10^4 K, the warm ionised medium (WIM), or 10^6 K, the hot ionised medium (HIM). McKee & Ostriker (1977) following on from Cox & Smith (1974) proposed a three phase model, also in pressure balance, consisting of the CNM, a warm phase (made up of both the WNM and the WIM) and the HIM. The HIM, sometimes called coronal gas, occupies low density SNe bubbles (superbubbles) which often join up forming a network of hot ionised material; it accounts for the majority of the gas in the Galactic halo.

The molecular medium is not a part of the three phase model – while its mass is significant – by volume it makes up a very small fraction of the ISM. The molecular medium is located in sub-regions within the CNM and it is discussed further in Section 1.2. All five phases are summarised in Section 1.1.3.

A lot of work has been done attempting to improve the models. Ikeuchi, Habe & Tanaka (1984) show that the ISM is strongly dependent on the SN rate, with two-phase and three-phase steady states being possible. They also show that it is possible to create a cyclic state (alternating over time between two and three phase states) or a runaway state in which SNe feedback is sufficient to ionise and heat the entire ISM.

The two and three phase models highlight the physics central to understanding the ISM as observed, but is still a long way from providing the complete picture. Shull (1987) point out some of the three phase model's shortcomings, such as assuming a uniform distribution of SNe explosions. Gazol, Vázquez-Semadeni, Sánchez-Salcedo & Scalo (2001) question the idea of discontinuous phase transitions. Using 2D simulations they identify that if additional physics is added to the two phase model, more gas is found at unstable temperatures. Gazol et al. (2001) point out that their conclusions agree with Arecibo 21 cm line observations by Heiles (2001), which suggest that a large fraction, >47%, of the WNM is at unstable temperatures. Hennebelle & Iffrig (2014) present simulations of galaxies with self-gravitation, galactic potential and magnetism, in which feedback is regulated by SNe. They compare random placement of SNe to placement correlated to star formation and find that the latter results in simulations that are closer to observations.

There is also a significant amount of 8000 K ionised gas present in the ISM, known as the WIM. It is predominantly ionised and warmed by O-type stars, existing in either HII regions directly around the stars or as diffuse H^+ in the wider ISM. HII regions are discussed in more detail in Section 1.4.

1.1.4 Heating and cooling in the ISM

There are a wide range of processes that regulate the temperature of the ISM and they are highly dependent on both the local gas and dust properties and the ambient radiation. Here we summarise the most important according to Draine (2011).

The most prevalent heating mechanism is photoelectric emission from dust. High energy photons from the interstellar radiation field (ISRF) (typically below 13.6 eV in the UV) can cause photoelectric emission from solid grains (and large molecules). As these photoelectrons thermalise they heat the local gas, although some of the

Table 1.1. Phases of the interstellar medium based on Stahler (2004) and Draine (2011). All values are approximations.

Phase	Number density [cm^{-3}]	Temperature [K]	Volume filling factor
cold neutral (CNM)	30	100	0.01
warm neutral (WNM)	0.6	5×10^3	0.4
hot ionised (HIM)	4×10^{-3}	$> 3 \times 10^5$	0.5
warm ionised (WIM)	0.3	10^4	0.1
molecular	> 100	10-50	0.01

energy will go to exciting/ionising hydrogen, reducing heating efficiency. This is a significant form of heating, in all but the ionised phases of the ISM, since an ionised dust grain or molecule will emit lower energy electrons for an equivalent photon energy. The effectiveness of this form of heating is slightly less in molecular gas since there are many more excited states available. Heating of ionised gas is described further in Section 1.4.1

For cooling, there is a lot of overlap between the physical processes discussed in Section 1.1.2 and those that govern the cooling physics in the ISM. Any photons emitted in the ISM will both carry away energy and be potentially observable. The cooling processes include the following (Draine, 2011).

- Collisionally excited emission lines
- Collisional ionisation and excitation of hydrogen
- Recombination of cooling hydrogen
- Bremsstrahlung
- Molecular cooling
- Emission from dust

1.2 Giant molecular clouds

The largest agglomerations of dense molecular gas, GMCs, are the most important component of the ISM to this work, since they are the sites of the majority of star formation and hence also stellar feedback (Kennicutt & Evans II, 2012). GMCs are clumpy regions of cold gas (10-50 K) with very high molecular fractions. It is in these structures that the lion's share of star formation occurs and in turn they are the sites of most O and B type stars which emit the vast majority of stellar feedback.

1.2.1 Formation of H_2

There are two reactions through which H_2 can form from H in isolation. Direct radiative attachment is the binding of two hydrogen atoms and the release of the binding energy as a photon. This is, however, an unlikely event since the excited molecule is far more likely to dissociate before it relaxes. Associative detachment (McDowell, 1961; Dalgarno & Mccray, 1973), involving a negatively charged hydrogen atom (H^-), obeys the following two step process,

$$\begin{aligned} H + e^- &\rightarrow H^- + h\nu \\ H^- + H &\rightarrow H_2 + e^-. \end{aligned} \tag{1.1}$$

This allows the electron to carry away the binding energy and is an order of magnitude faster than direct radiative attachment. Although, it still cannot account for the amount of H_2 present in the ISM.

It is now thought, however, that the vast majority of H_2 is formed via interactions with dust through a mechanism known as grain-surface catalysis (McCrea & McNally, 1960; Gould & Salpeter, 1963). As long as both a hydrogen atom and a dust grain are cool enough (< 100 K), the probability that they will 'stick' on collision is high. When bound to a grain, H atoms will migrate to energetically stable positions (created by valence or van der Waals forces). Here they are likely to come into contact with other H atoms and react, forming H_2. The binding energy can be absorbed by a number of processes as a result of interaction with the dust grain.

1. Direct heating of the dust grain.
2. Breaking free from the potential binding the molecule to the grain.
3. Vibrational energy states in the H_2 atom itself.

It is thought that most H_2 formation occurs on larger grains, since although they have a lower surface area per unit mass, they are more likely to be involved in multiple collisions with H^0 (Draine & Bertoldi, 1996).

1.2.2 H_2 dissociation

Molecular hydrogen in the ISM is constantly at threat of dissociation via a number of processes. Collisional dissociation occurs when temperatures rise above 4000 K (Dalgarno & Roberge, 1979). Photodissociation can occur either directly, or via UV fluorescent photodissociation (Black & Dalgarno, 1976). Direct photodissociation requires photons with energies above 14.7 eV which are rare since the majority of > 13.6 eV photons are more likely to ionise HI due to its greater cross section

(Section 1.4). This makes UV fluorescent photodissociation the predominant mode of dissociation in the ISM; Lyman and Werner band photons excite H_2 into one of various vibrational levels from which dissociation is possible.

1.2.3 Forming clouds

The molecular medium does not consist of gas at fixed temperatures and densities, but rather a continuous transition from the CNM through to the densest and coolest gas. Snow & Mccall (2006) define two intermediate stages between the CNM and dense molecular clouds being 'diffuse molecular clouds' and 'translucent clouds'.

The CNM is mostly un-shielded from the ISRF, meaning that all H_2 is typically short lived and found at low concentrations due to photodissociation (Draine, 2011). If a region of CNM is large enough, the centre becomes partially shielded from the ISRF. This allows for a more significant H_2 fraction. In these 'diffuse molecular clouds' the molecular fraction of CO remains low, with more than half of the atomic carbon being ionised.

If the shielding level for some gas in the cloud is high enough, translucent clouds can form. In translucent clouds H_2 and CO fractions are both increased although the CO fraction still lags behind. As more molecules are present, the chemistry of translucent clouds is vastly more complex than less dense regions of the ISM, thus a host of new molecular cooling reactions become possible. Molecular chemistry in the ISM remains a very active area of study in which much is still unclear (Öberg, 2016; Van Dishoeck, 2018; Cuppen et al., 2017).

As translucent clouds cool further and densities increase, the shielding continues to increase until nearly all carbon is in the form of CO. The largest of these dense regions are known as GMCs. The gas in GMCs is self-gravitating and can begin to collapse beyond the rate that steady cooling and pressure balance with surroundings would allow.

1.2.4 Cloud fragmentation

GMCs are hierarchical in their structure, being very clumpy objects. The origins of this structure lie in the process of fragmentation. Any (approximately spherical) region of gas can be found to be stable or unstable against collapse depending on its pressure, density and size (Jeans, 1902). The Jeans length, the size scale at which such a region of gas switches between pressure support and gravitational collapse,

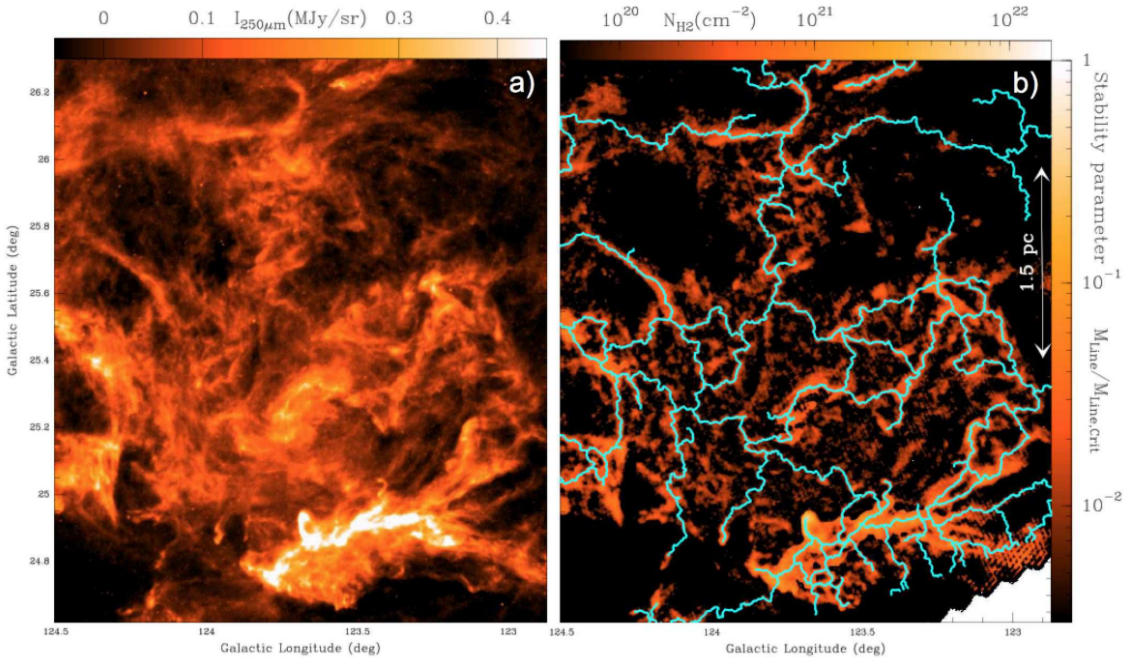

Figure 1.5. Filamentary fragmentation in the Polaris flare translucent cloud. (a) dust continuum map from Herschel/SPIRE 250 μm. (b) Corresponding column density map in which the filaments have been identified using DisPerSE (Sousbie, 2011). Taken from André et al. (2014).

is given by

$$\lambda_{\rm j} = \left(\frac{15 k_{\rm B} T}{4\pi G m_p \mu \rho} \right)^{\frac{1}{2}}, \tag{1.2}$$

where $k_{\rm B}$ is Boltzmann's constant, T is the gas temperature, G is the gravitational constant, m_p is the proton mass, μ is the atomic weight of the gas, and ρ is the density. For any region collapsing under gravity, turbulent flows in the gas can cause interior pockets to form which are larger than their own Jeans length.

Turbulence cascades through multiple size scales, and as a result so does fragmentation due to Jeans collapse; this causes the hierarchical structure of GMCs'. As the densest fragments exceed $\approx 10^{-13}$ g cm^{-3}, the gas becomes optically thick to the cooling radiation. This defines a lower limit for the fragmentation process known as the opacity limit (Low & Lynden-Bell, 1976; Rees, 1976). As can be seen in Figure 1.5, this fragmentation process is not limited to spherical structures and most often leads to the formation of filaments of dense gas running through GMCs. The densest regions typically form at intersections of filaments.

1.2.5 Identifying GMCs

Identifying GMCs and the clumps within them, from observations and simulations, can been done using algorithms such as CLUMPFIND (Williams, de Geus & Blitz, 1994) and CPROPS (Rosolowsky & Leroy, 2006). These are powerful and simple tools able to highlight regions by density using both 2D and 3D data. However, such tools are highly dependent on the input parameters and resolution, which can lead to inconsistent identification of clumps particularly from observed data (Pineda, Rosolowsky & Goodman, 2009).

Some more sophisticated approaches to analysing GMC structure have been made that break down the hierarchical structure and present it as a dendrogram such as Rosolowsky, Pineda, Kauffmann & Goodman (2008); Goodman et al. (2009) and more recently SCIMES (Spectral Clustering for Interstellar Molecular Emission Segmentation, Colombo et al., 2016; Colombo et al., 2015; Duarte-Cabral & Dobbs, 2016). These tools look at the entire density continuum and build a dendrogram of the objects' substructures, rather than choosing some boundary criterion to define objects on different scales.

1.2.6 Properties of clouds

GMCs are loosely defined as clouds of predominantly molecular gas of mass 10^4 to $10^7 M_\odot$ (Blitz, 1993). Larson (1981) identified the following relationships between properties of GMCs.

1. The velocity dispersion in clouds, σ_v, is related to the size scale of the cloud, R, by $\sigma_v \approx R^{0.38}$. The relationship suggests the clouds are highly turbulent.
2. The clouds are supported against gravity by internal turbulence, which is approximated via measurements of the velocity dispersion.
3. The mean density, n, of clouds is related to their size by $n \approx R^{-1.1}$. This also suggests that cloud column densities (and hence surface densities) are not dependent on size.

The relationships were subsequently confirmed by Solomon et al. (1987) and have been fundamental in guiding the community. However, more recently these relationships have been challenged by Heyer, Krawczyk, Duval & Jackson (2009) and Miville-Deschênes et al. (2017), who demonstrate the dependence of $\sigma_v / R^{0.5}$ on the GMC surface density, Σ. Figure 1.6 shows this dependence for clouds with $\Sigma > 10$ $\mathrm{M_\odot pc^{-2}}$, however, clouds with lower surface densities show little correlation.

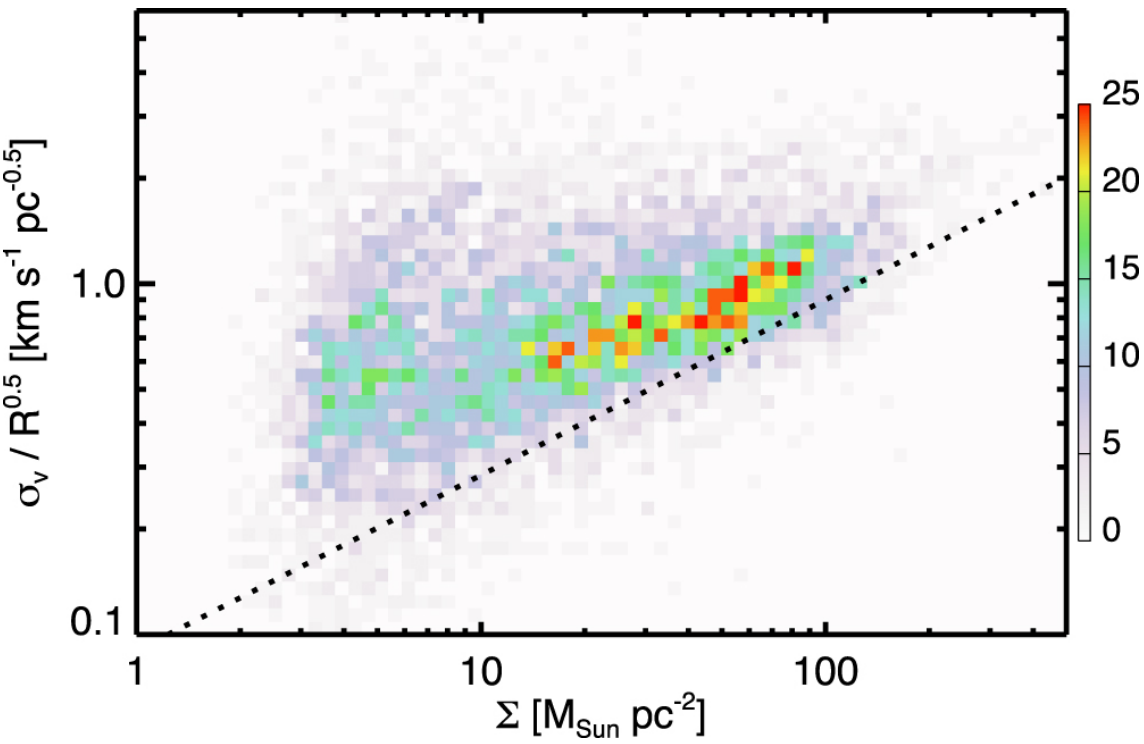

Figure 1.6. Histogram in $\sigma_v/R^{0.5}$ and Σ space, the colour axis gives the bin frequency for a catalogue of 8107 clouds. The dotted line represents the positions of gravitationally bound clouds. Taken form Miville-Deschênes et al. (2017)

.

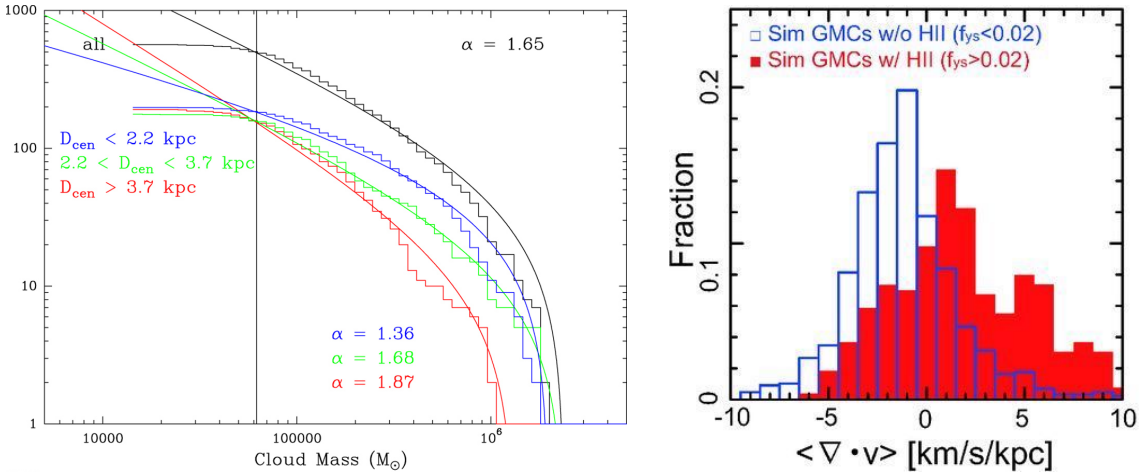

Figure 1.7. Left panel: cloud mass functions for clouds in M33 (Braine et al., 2018). The black line is the sum of all clouds and the coloured lines are clouds grouped by galactic radius. The vertical black line shows the survey completeness limit, GMCs of masses below this limit are under-represented. The α values give the slope of the mass function (Equation 1.3). Right panel: fraction of clouds in a galaxy simulation at given volume weighted velocity divergence, $\langle \nabla \cdot \mathbf{v} \rangle$, for clouds with and without heating due to HII regions (Baba et al., 2017). Clouds with $\langle \nabla \cdot \mathbf{v} \rangle$ below zero are collapsing and those above zero are expanding.

GMC mass functions can typically be described by a power law

$$\frac{\mathrm{d}N}{\mathrm{d}M} = M^{-\alpha}, \tag{1.3}$$

where N is the number of clouds and M is their mass. The α value is dependent on a GMC's host galaxy and its location within the galaxy. In the Milky Way α is between 1.5 and 2.0. (Solomon et al., 1987; Kramer & Stutzki, 1998; Roman-Duval et al., 2010; Miville-Deschênes et al., 2017). Most of the molecular mass in the milky Way is found in the larger clouds (90% in GMCs $>10^5 M_\odot$)

Observations of M33 show that the fraction of high mass GMCs decreases with galactic radius (left panel, Figure 1.7). This behaviour has been observed throughout the local group (Rosolowsky, 2005). This trend can also be seen in the Milky Way, with the inner Galaxy containing 60% of the GMCs but 85% of their mass (Miville-Deschênes et al., 2017).

Maeda, Ohta, Fujimoto & Habe (2020) compare observations of the strongly barred galaxy NGC 1300 to work by Colombo et al. (2014) on the spiral galaxy M51 (the whirlpool galaxy). They find that the star formation efficiency (SFE) in the bar is low compared to the arm, but that the physical properties of the GMCs do not vary, other than their peak temperatures. They suggest that mechanisms such as fast cloud-cloud collisions may control the SFE in NGC 1300, rather than GMC properties.

1.2.7 Lifetimes

The lifetimes of GMCs are difficult to determine observationally due to the lack of an exact definition of a GMC and the need for indirect methods owing to their long lifetimes. Elmegreen (2000) and Murray (2011) calculate GMC lifetimes of one to a few free-fall times ($\approx$ 10-30 Myr), by inference from the timescales of SF within them. The existence of GMCs in inter-arm regions has been used to suggest that clouds could have lifetimes upt to 100 Myr (Scoville & Hersh, 1979; Koda et al., 2009). However, Meidt et al. (2015) find that GMCs in M51's inter-arm regions have lifetimes around 20-30 Myr, by using cloud number statistics and the gas travel time between sprial arms. Galaxy simulations by Dobbs & Pringle (2013) find cloud lifetimes of between 4 and 25 Myr, but it should be noted that direct comparisons with lifetimes calculated by observers should be made carefully as a result of the differences between the methods used. Chevance et al. (2020) measure GMC lifetimes of 10-30 Myr, they suggest that GMCs spend 75-90% of their lives

without forming stars, after which they are dispersed, by stellar feedback, within 1-5 Myr of massive stars forming.

A useful quantity, often used as metric when describing cloud lifetimes, is the free-fall time (t_{ff}), i.e. the time for a GMC to collapse under its own gravity. For a spherical cloud at uniform intitial density (ρ_0), it is given as,

$$t_{ff} = \sqrt{\frac{3\pi}{32G\rho_0}}, \tag{1.4}$$

where G is the gravitational constant. It can be derived by considering the motion of a single gas particle from the edge of the cloud to the centre. Whilst being a useful tool to compare the lifetimes of clouds it is a particulalry crude approximation to reality since few GMCs are close to being spherical, it ignores the clouds internal pressure, and the energising effects of stellar feedback are not considered. It also does not consider a cloud's rotation or internal turbulence. It is comparible in magnitude to the sound speed crossing time of a cloud.

1.3 Star formation

Star formation occurs in dense cores, the smallest and densest fragments in GMCs (Section 1.2.4). These cores collapse under gravity and, since at these densities they are opaque to cooling radiation, they can no longer remain cool. The dense core collapses into a protostar and surrounding gas, and dust, fall onto the plane defined by its mean angular momentum, forming a pre-stellar disc. Further detail of individual star formation is beyond the scope of this work, it is well reviewed by Shu, Adams & Lizano (1987) and Zinnecker & Yorke (2007).

While this work is not concerned with the formation of individual stars, it is critical for us to understand, the observed distribution of young stars by mass, the SFRs and SFEs of star forming regions, and the properties and behaviour of main sequence stars of $> 20M_{\odot}$.

1.3.1 The initial mass function

A great deal of effort has gone into establishing an analytic distribution of stars by mass – the mass function – in the Milky Way and beyond. The mass function is biased towards the low mass stars as a result of the mass dependence of stellar lifetimes. By correcting for this bias, Salpeter (1955) made the first attempt to tie the observed distribution of field star masses to the initial mass function (IMF) –

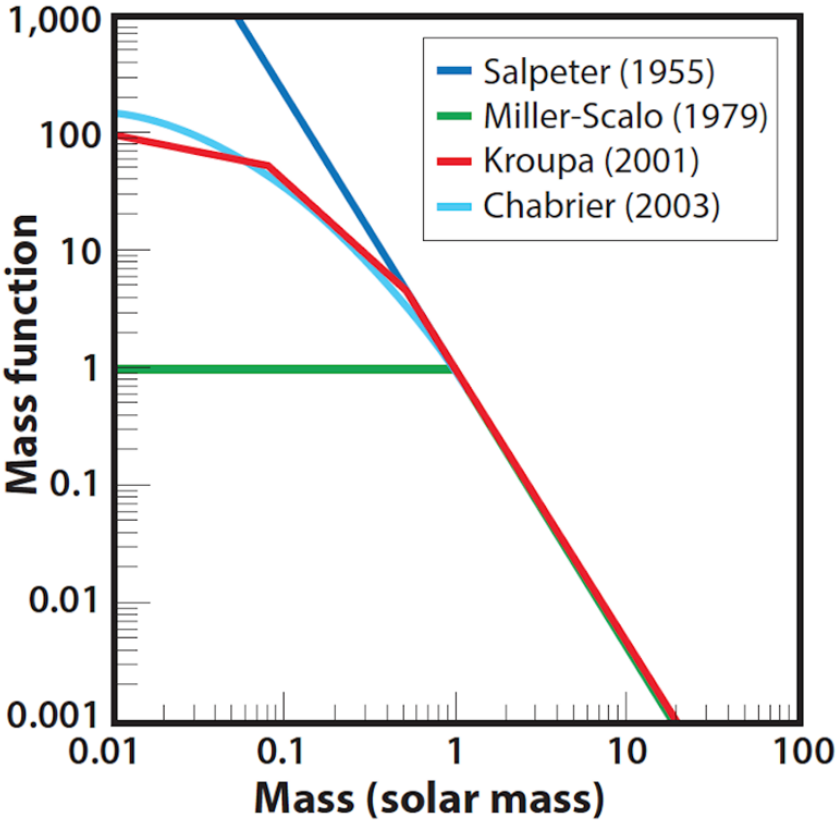

Figure 1.8. Four IMFs where the mass function (y-axis) is the number stars per element of mass, $N(m)\,\mathrm{d}m$.

the global mass function for populations of newly formed stars.

Mass functions are typically power laws taking the form $N(m)\,\mathrm{d}m$, where N is the number of stars and m their mass. A typical distribution of stars can be produced by finding the stars in some a set of ranges given by m to $m + \mathrm{d}m$. The Salpeter (1955) IMF takes the form

$$N(m) = 0.03 \left(\frac{m}{M_\odot} \right)^{-2.35} . \tag{1.5}$$

Miller & Scalo (1979) identified that the Salpeter (1955) IMF over-sampled stars at the low mass end, they used a broken power law to address this.

One of the major difficulties in developing accurate IMFs, is unresolved multiple systems. These affect the IMF both through their quantity and the relative masses of their members. Chabrier (2003) present two separate IMFs, one considering single observed objects and the other attempting to correct for some binary fraction. All the IMFs discussed here have very similar functional forms for stars above 1 $M_\odot$ as

can be seen in Figure 1.8. In this work, since we have little interest in low mass stars, we use the Kroupa (2001) IMF since it takes a simplistic form that is convenient to implement. The Kroupa (2001) IMF is given by,

$$\begin{aligned} &N(m) = m^{-\alpha}, \text{ where} \\ &\alpha = 0.3 \qquad\qquad 0.01M_{\odot} < m < 0.08M_{\odot} \\ &\alpha = 1.3 \qquad\qquad 0.08M_{\odot} < m < 0.5M_{\odot} \\ &\alpha = 2.3 \qquad\qquad m > 0.5M_{\odot}. \end{aligned} \tag{1.6}$$

There is some evidence to suggest that the origin of the IMF can be found by looking at dense cores. Alves, Lombardi & Lada (2007) find that observed dense core masses correlate with the IMF with a gas mass to star mass efficiency of 30%.

1.3.2 Global star formation efficiencies

Krumholz et al. (2012) compile SF data from a wide variety of star forming regions (Galactic and extra-galactic) shown in Figure 1.9. The gradient of this graph gives an approximation to a universal SFR per free fall-time, where the free fall time is the time for a GMC to collapse under its own gravity, which they call the local SF law. They find a clear correlation between surface density and star formation per free fall time averaging 1% of the cloud mass per free-fall time ($\epsilon_{\rm ff}$). This relationship appears to hold for all star-forming regions. In Figure 1.9, the grey band shows a factor 3 variation in $\epsilon_{\rm ff}$, the most distant outliers are within a factor of 10.

This value for $\epsilon_{\rm ff}$ suggests SFEs much lower than those found in early simulations of star formation that resolved down to the opacity limit (Bate, Bonnell & Bromm, 2003). This suggests that turbulence alone is not enough to regulate star formation and determine the final SFE.

1.3.3 Stellar feedback

Over the course of their lifetimes all stars release mass and energy back into their surroundings, all the processes by which this occurs are collectively known as stellar feedback. Typically the energy budgets and ejected mass fractions are far higher per unit star mass for O and B type stars. The lifetimes of massive stars ($> 8M_{\odot}$) range from ≈ 3 to 35 Myr (from the stellar evolution code SeBa, Portegies Zwart & Verbunt, 2012)[1], being three times shorter to three times longer than the lifetimes

[1]The SeBa code uses the stellar evolution models presented in Portegies Zwart & Verbunt (1996). More recent updates are described in Toonen, Nelemans & Portegies Zwart (2012)

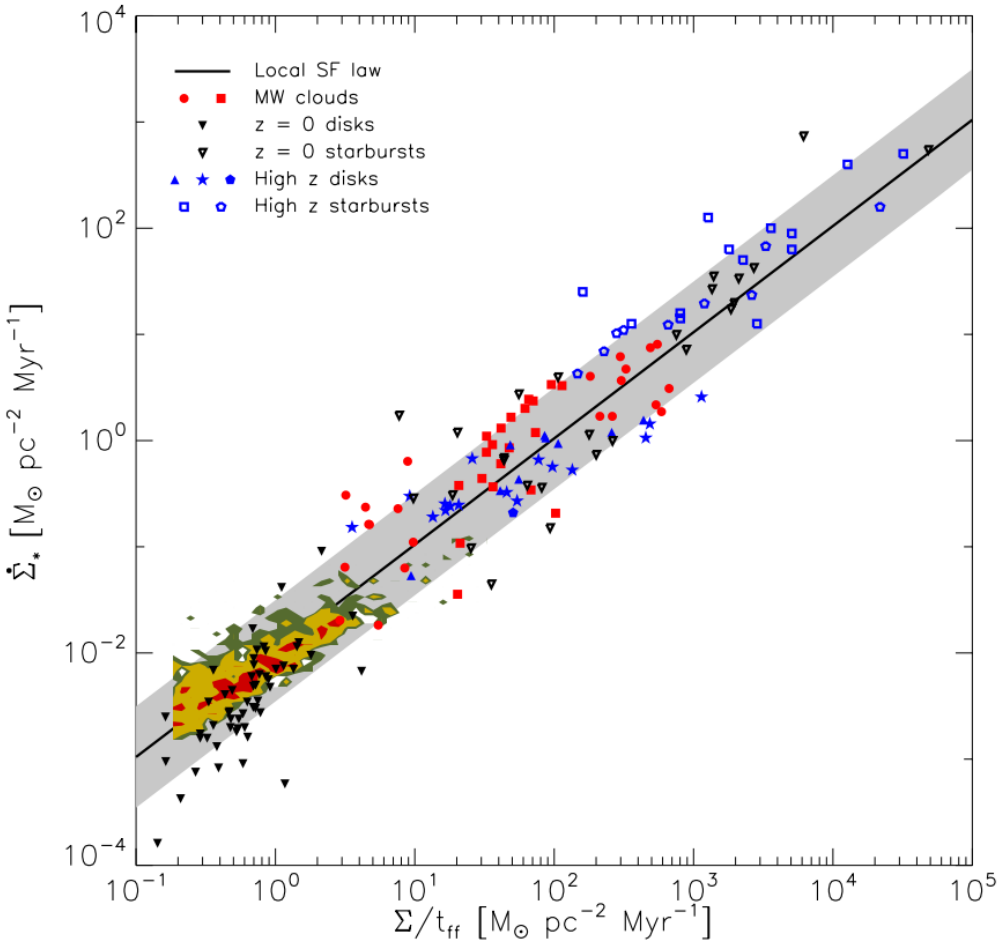

Figure 1.9. SFR per square parsec Vs gas surface density over free fall time for a range of Milky Way and external objects. Shapes correspond to source of data, colours to type of object. From Krumholz et al. (2012)

of GMCs (Section 1.2.7). This means that their feedback is best considered a part of the star formation process.

Stellar feedback affects the ISM by injecting energy and momentum by a multitude of processes. These processes can have axial dependence – such as protostellar outflows emitted from a young star's poles, or relative axial uniformity – such as the radiation emitted by a star. The feedback can be momentum driven as a result of gas being able to cool at a rate comparable to that at which it is heated or explosive if gas is heated by a significant amount. Some feedback is considered to be purely thermal in that it heats gas but does not affect the momentum of the gas at all – such as non-ionising radiation.

From numerical simulations, there have also been many studies of the role of stellar feedback in individual molecular clouds (discussed in the following sections). These have shed light on the role and relative importance of different feedback mech-

anisms in different environments. However, there remain many questions relating to their collective role, especially over larger size and longer time scales.

The simulations presented in Chapters 3 to 5 only model two forms of stellar feedback, photoionisation and SNe, and only for stars of mass greater than 20 $M_{\odot}$; we discuss these in some detail in Sections 1.4 and 1.5. The time release of energy between photoionisation and SNe is very different. Photoionising radiation is emitted from stars throughout the main sequence, however, SNe release their energy effectively instantaneously at the end of the star's lifetime which ranges from 3 Myr to 10 Myr for stars $> 20M_{\odot}$. In Section 1.6 there is a briefer summary of other feedback mechanisms – protostellar outflows, radiation pressure, and stellar winds – which are less relevant to this work.

1.4 Photoionisation

Strömgren (1939) proposed that bright nebulae were ionised regions around massive stars. O and B type stars generate enough Lyman continuum photons ($h\nu$ >13.6 ev) to ionise large regions around them. When a young star begins emitting Lyman flux, the ionised region rapidly grows to the Strömgren radius ($R_{\rm S}$) at which equilibrium forms between the rate of ionisation and recombination within the HII region – this is known as the R-type expansion phase. The gas in these regions undergoes a constant cycle of ionisation and recombination which leads to an increase in temperature, which drives a second, slower, D-type expansion phase.

1.4.1 HII region temperature

The heating and cooling processes in HII regions are well described in Draine (2011), here we briefly discuss some of the most important. The predominant heating effect within these regions results from the surplus energy of the ionising photons above the ionisation energy of hydrogen and helium. Every ionisation event produces an electron with $h\nu - h\nu_0$ surplus kinetic energy, where $h\nu_0$ is the ionisation energy. Some heating also occurs through photoelectric emission from dust, although this is highly dependent on both the dust abundance and the intensity of lower energy photons. Cosmic rays can also heat HII regions both by direct interaction with free electrons and ionisation, resulting in very high energy electrons.

Every recombination event that does not result in a direct transition to the ground state results in the loss of the ionisation energy. Lower energy electrons are more likely to recombine. Free-free emission and collisionally excited line radiation

from heavier elements are also important cooling processes in HII regions.

Draine (2011) suggest that this leads to thermal equilibrium occurring at T $\approx 8,050$ K in Orion like HII regions and up to $\approx 15,600$ K in low-metallicity galaxies. Observed HII region temperatures in the Orion Nebula typically fall in the 8,000 to 11,000 K range (Baldwin et al., 1991; Jamet et al., 2005; Rodríguez & García-Rojas, 2010).

1.4.2 Impact on star formation

While the theoretical Strömgren sphere is a very useful tool, in practice the contours of HII regions are determined by the morphology of their surroundings as much as by the Lyman flux that sculpts them. Figure 1.10 shows two adjacent, almost interconnecting, HII regions in the Orion nebula. Where one is almost spherical (if partially obscured by a filament), the other has nearly broken out of the cloud on one side and is highly asymmetric.

Some observations suggest that photoionising feedback and the resulting HII regions are thought to play a vital role in determining the sites of star formation through triggering. Most notably this is expected to happen via the collect and collapse model (Elmegreen & Lada, 1977), where shells of gas are swept up in front of ionisation fronts (IFs) and fragment into star forming clumps, which has been observed by Deharveng, Zavagno & Caplan (2005), Pomarès et al. (2009) and Zavagno et al. (2010). Within HII regions, bright rimmed clouds are often created by radiation-driven implosion (Bertoldi, 1989; Morgan, Thompson, Urquhart & White, 2008). Both of these mechanisms, that can potentially trigger star formation, have been observed on scales of up to several pc, yet surveys of extragalactic HII regions show that OB associations are capable of creating shells many tens of pc across (Anderson et al., 2014; Hindson et al., 2016). This suggests that there could be further-reaching, but harder-to-observe, effects of photoionisation.

Numerical simulations of single clouds have the advantage that the gas and feedback are well resolved, but have the disadvantage that once the feedback reaches the edge of the cloud, it is completely free to escape outside the computational domain. For many of these simulations, there is one single massive star, for example Ali, Harries & Douglas (2018) and Ali & Harries (2019) include a 34 $M_\odot$ star, Haid, Walch, Seifried, Wünsch, Dinnbier & Naab (2018) examine the effects from three different mass stars, Geen, Hennebelle, Tremblin & Rosdahl (2016) investigate clouds with different ionising sources. Others such as Dale, Ngoumou, Ercolano & Bonnell (2014) and Zamora-Avilés et al. (2019) consider more massive (10^5 $M_\odot$)

Figure 1.10. Two HII regions in the Orion nebula, the source of photoionisation is four massive stars known as the Trapezium. Ionised gas is represented in shades of green, and molecular gas in shades of red and orange. One of the HII regions is well contained within molecular gas, the other has almost broken out of the cloud entirely on one side. Image taken with NASA's Spitzer and Hubble Space telescopes (credit: NASA/JPL-Caltech/STScI).

clouds including multiple sources.

These simulations tend to find that photoionisation has a major role in disrupting the cloud, even if the SFR is still high compared to those observed (Dale et al., 2014). As would be expected, smaller clouds subject to higher ionising sources are more efficiently dispersed by ionisation (e.g. Gavagnin, Bleuler, Rosdahl & Teyssier, 2017).

1.5 Supernovae

SNe are classified by their optical spectra (Filippenko, 1997), however, for this work it is more useful to think in terms of the mechanisms that cause them. We are

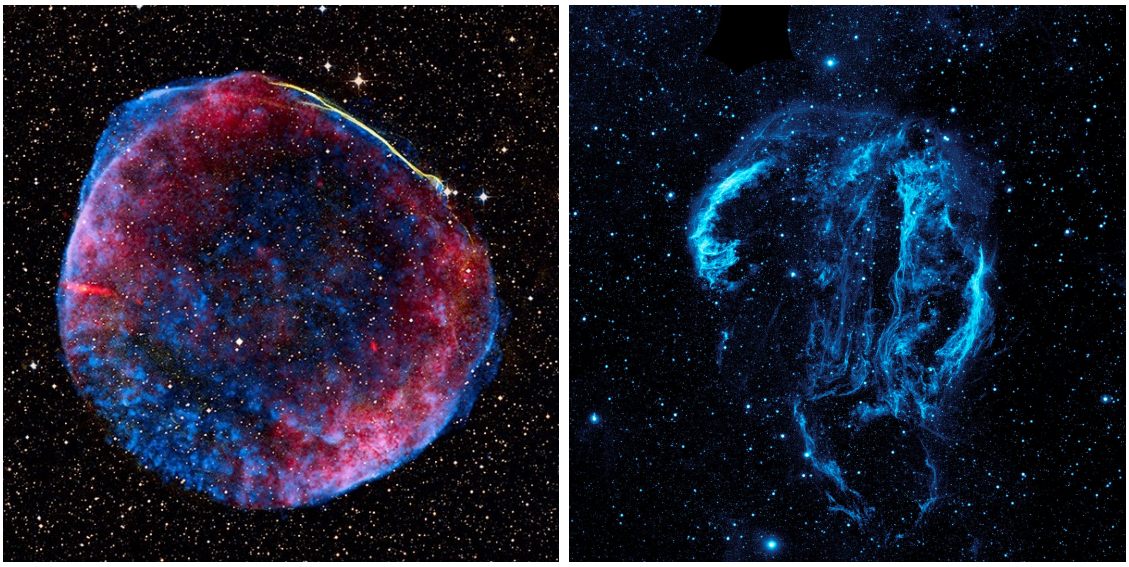

Figure 1.11. Left panel: SN 1006 was the brightest SN in recorded history, as viewed from Earth in 1006 AD. The remnant has a diameter of around 20 pc. Its expansion rate varies around the shell from 3000-7500 km s^{-1} (Winkler et al., 2014). Credit: NASA, ESA, Zolt Levay (STScI) Right panel: The Cygnus Loop nebula, a later stage SNR that has evolved for approx. 5000-8000 years. The remnant has a diameter of around 40 pc. Credit: NASA/JPL-Caltech.

interested in SNe that result from the core collapse of massive stars when they reach the end of their lifetime – those that are tied to the star formation process – as opposed to type Ia SNe, in which core collapse is initiated by accretion onto a white dwarf or the collision of two white dwarfs. Such a SN occurs as fusion slows and the core is no longer able to support itself against gravity. The exact mechanisms vary a great deal depending on the progenitors mass and metallicity (Janka, 2012). Here we will only discuss the evolution of the supernova remnant (SNR) – i.e. the effect that SNe have on the ISM.

1.5.1 Supernova remnant expansion

The SNR evolves through three distinct phases: the free expansion phase, the adiabatic phase, and the pressure-driven snowplough phase, before merging with the ISM.

Initially the SN ejecta advances with little resistance sweeping up material as it goes. A contact discontinuity forms between the ejecta and the swept up material. The shocked material's pressure is greater than the thermal pressure in the growing cavity and a reverse shock builds in the ejecta. Once the mass of the swept up material begins to be comparable to the mass of the ejecta, it is able to decelerate the expansion. The reverse shock begins to move inwards heating the ejecta as it

goes. The free expansion phase is defined to end when the ejecta and swept up material are equal in mass. This sweep-up radius is therefore defined as

$$R_{\rm SW} = \left(\frac{3M_e}{4\pi\rho_0}\right)^{1/3}, \tag{1.7}$$

where M_e is the ejecta mass and ρ_0 is the initial density of the circumstellar medium (CSM) (Draine, 2011). The free expansion phase depends only on the initial energy released by the SN and typically takes a few hundred years.

As the swept up mass increases, the reverse shock heats the growing cavity to very high temperatures. Although the temperatures are high, the density inside the SNR cavity is very low meaning that cooling is very inefficient. Sedov (1959) and Taylor (1950) derived expressions for the subsequent pressure driven expansion – the Sedov-Taylor (ST) phase – which can be treated as entirely adiabatic. The ST phase is treated as a temperature injection only problem or a point explosion. This stage lasts for the order of thousands of years.

Once the shock cools to around 10^6 K, radiative cooling becomes significant. This moves the SNR out of the adiabatic phase and the temperature, that was previously driving the pressure driven expansion, drops. During this final phase – known as the pressure-driven snowplough phase – the sweep up mass is significantly larger than the ejecta mass and the pressure difference across the shock drops, leading to deceleration. This phase is discussed in more depth in Section 2.3.5. Eventually as the shock velocity drops to the sound speed of the post-shock gas, the SNR merges with the ISM – at around 10^4 K, the temperature of the warm media. Figure 1.11 shows two SNRs: the SN 1006 remnant, still in the ST phase, and the Cygnus Loop nebula in the snowplough phase.

1.5.2 Simulating supernovae

SNe are massively energetic single events, although for $> 20M_\odot$ stars, they release less energy than the contributions from photoionisation over a star's lifetime. Studies of the effect of SNe feedback on the ISM on Galaxy scales have shown that they are important in defining many Galactic properties. They drive the turbulence that provides the vertical support for the Galactic disk (De Avillez & Breitschwerdt, 2005; Kim, Ostriker & Kim, 2013) and they are also able to determine the structure of the ISM (Dalla Vecchia & Schaye, 2008; Dobbs & Pringle, 2013).

Radiative cooling has a large effect in SNe simulations, and simulations that do not include it likely over-estimate the ability of SNe to disperse molecular clouds

(Walch & Naab, 2015). Lucas, Bonnell & Dale (2020) re-run the simulations of Dale, Ercolano & Bonnell (2013) with supernova feedback and find that SNe interact with the ISM very differently when either winds or photoionisation have created a low density bubble around the SN progenitor. Lucas et al. (2020) and Walch & Naab (2015) find that if clouds are subjected to photoionising feedback first, super-bubbles can form from just a single SN event. The latter of these authors find that without pre-supernovae feedback, superbubbles only form in well timed cascades of SNe.

Seifried et al. (2018) find that SNe external to clouds can drive turbulence within them but only temporarily (a few hundred kyr). This external driving of turbulence is most significant if the SNe are close to the GMCs (< 25 pc) and occur as it is forming. They consider it likely that internal effects, such as local gravitational collapse and stellar feedback, are more important in driving turbulence as the cloud matures.

1.6 Other forms of stellar feedback

While it can be a useful exercise to compare the relative energy budget of different feedback mechanisms their different coupling efficiencies with the CSM and ISM mean that the most energetic feedback mechanism, is not necessarily the most important to a problem. While feedback mechanisms are very well understood analytically, their exact impact on the ISM is hard to determine owing to the lack of symmetry in realistic environments. Numerical simulations are becoming increasingly good at showing the effects of one or maybe a few feedback processes. However, how all feedback mechanisms work together over many size scales is still relatively poorly understood.

1.6.1 Protostellar outflows

Many astronomical objects exhibit outflows that are typically, but not always, collimated. The most common cause of such outflows is accretion onto the object. Accretion occurs due to many processes, such as symbiotic stars, protoplanetary nebulae, accreting neutron stars, and accreting black holes, to name a few. The most relevant to this work, due to our focus on star forming regions, are protostellar outflows that are caused by accretion on to young stellar objects (YSOs).

It is not only the causes of outflows that vary, but also their nature. Outflow velocities from YSOs vary from several km s^{-1} to more than 10^3 km s^{-1}, however, outflows from neutron stars and black holes can be relativistic (Bally, 2016). While

the majority are highly collimated jets, they can also take the form of bi-polar lobes or even almost spherical winds (Nakamura et al., 2012; Arce, Mardones, Corder, Garay, Noriega-Crespo & Raga, 2013).

Protostellar outflows are one of the earliest forms of feedback to affect gas in star forming regions and are capable of affecting the CSM on scales of several pc (Heyer et al., 1992; Feddersen et al., 2018). They are, however, short lived compared to the timescales of the simulations presented in this work. While they no doubt have a significant effect on star forming regions, we consider them negligible on large size and long time scales compared to photoionisation.

1.6.2 Radiation pressure

All radiation emitted from a star will exert a force on gas or dust if it is absorbed or scattered. The relative importance of this radiation pressure force is dependent on the optical depth of any given species. Dust typically has a high radiation pressure cross-section and, as such, radiation pressure on dust is dominant over gas.

Since both gravity and radiation pressure drop off with the inverse square law, a radius independent relationship between them can be found. If the Luminosity (L) over the mass (M) of a star is $> 30 L_{\odot}/M_{\odot}$, the radiation pressure exceeds the gravity (Draine, 2011).

Since the effect of radiation pressure is proportional to a stars luminosity, it is most important for massive stars. Radiation pressure is only of significant importance for the most massive stars ($>20 M_{\odot}$) and clusters ($>10^{3.5} M_{\odot}$) (Krumholz & Matzner, 2009; Krumholz & Thompson, 2012, 2013). It is only in the largest and densest star forming regions that the early expansion of HII regions is dominated by radiation pressure (Kim, Kim & Ostriker, 2018).

More recently it has been suggested that some previous papers studying radiation pressure are likely to have over-estimated its ability to halt accretion owing to resolution criteria attached to the scale of the dust sublimation front (Krumholz, 2018). There are also resolution criteria associated with the mean free path of the radiation, very high resolutions are typically required to achieve convergence (Hopkins & Grudić, 2019). Hopkins & Grudić (2019) present methods to correct for insufficient resolution, but they involve integrations across the faces of neighbouring volume elements, meaning they are only feasible in adaptive mesh refinement (AMR) and moving mesh codes and not appropriate for pure smoothed particle hydrodynamics (SPH).

In this work the effects of radiation pressure are not simulated. While this is

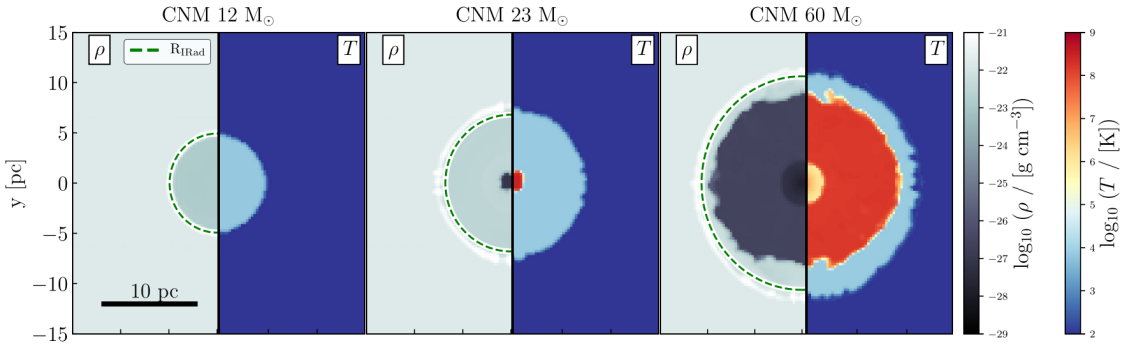

Figure 1.12. Stellar wind bubbles forming inside HII regions for 12, 23 and 60 $M_{\odot}$ stars in the CNM at a number density of 100 cm^{-3} and a temperature of 20 K. The LHS of each panel shows density and the RHS temperature. The dotted green line shows the theoretical extent of the HII region (Haid et al., 2018)

a practical decision for the reasons described above, it can be justified since the simulations do not resolve the small scales at which radiation pressure is sometimes found to dominate compared with photoionisation.

1.6.3 Stellar winds

The causes of stellar winds vary by stellar mass and age. Here we focus on main sequence winds from massive O and B type stars. In these stars the winds are driven by radiation pressure on heavy elements in the stellar atmosphere (Castor, Abbot & Klein, 1975) and are ejected at very high temperature and velocities. Around massive stars, winds are able to create large bubbles of heated gas such as the emission nebula M17, observed by Dunne et al. (2003).

Several studies have shown that feedback from winds alone is able to disrupt clouds before supernovae take effect (.e.g. Rogers & Pittard, 2013; Rey-Raposo, Dobbs, Agertz & Alig, 2017). However, the reality for the majority of massive stars is that wind bubbles form inside HII regions (Figure 1.12). While wind bubbles are distinct and observable hot (up to 10^7 K) regions, whether they have a significant impact on the wider ISM when compared to photoionisation is a crucial question. A simple comparison of the energy budget of winds and photoionisation would suggest that winds would be negligible, however, winds couple to gas more efficiently.

Haid et al. (2018) and Geen, Pellegrini, Bieri & Klessen (2020) perform spherically symmetric simulations with a range of massive stars. Haid et al. (2018) suggest that the effectiveness of stellar winds is highly dependent on the CSM, they embed a star into different phases of the ISM modelling both winds and photoionisation. They find that the momentum transferred to the ISM exceeds that of photoionisa-

tion, if the CSM is made up of the WIM. For the CNM and WNM photoionisation is dominant, although still relevant for the most massive stars. Geen et al. (2020) summarise that winds only dominate stellar feedback on the smallest of size scales, although again suggest that they are non-negligible when considering the dynamics of the ISM in at least some environments.

Dale et al. (2014) investigate the combined effect of both ionisation and winds, concluding that ionisation is dominant over winds, however, winds can still have a significant role in determining the morphology of low mass clouds. The computational expense and complexity of including both of these feedback mechanisms means that this work only includes photoionisation.

Chapter 2

Numerical methods

In this chapter we begin with a discussion of various numerical approaches to hydrodynamics (Section 2.1), we then detail the smoothed particle hydrodynamics (Gingold & Monaghan, 1977; Lucy, 1977) approach used in this work (Section 2.2), and next we discuss the additional physics that is included in the simulations (Section 2.3). Lastly, we describe our method for increasing resolution in smoothed particle hydrodynamics (SPH) simulations for the purpose of re-simulation (Section 2.4).

2.1 Numerical astrophysical hydrodynamics

Simulating star formation is fundamentally a problem of modelling the fluid dynamics of interstellar gas. Three dimensional numerical simulations are by far the most desirable approach. While analytical models are incredibly useful for understanding individual aspects of the star formation process, particularly when the processes involve high degrees of symmetry, they cannot well describe the behaviour of gas spanning many parsecs. 1D and 2D models, that can be very effective in describing the behaviour of stars and discs are not well suited to problems lacking symmetry.

On cloud scales and above, star formation is a problem that, unlike core collapse and disc accretion, lacks any form of symmetry. It is therefore typically simulated numerically in 3 dimensions. Here we discuss the motivations behind the choice of our hydro-dynamical approach.

2.1.1 Numerical methods for hydrodynamics

There are two fundamental approaches to numerical simulations of hydrodynamics: Eulerian approaches; known as grid methods, and Lagrangian approaches; most

commonly smoothed particle hydrodynamics. We have worked with SPH throughout this work and discuss our motivations for this below.

Grid methods discretise space into cells, typically on a Cartesian geometry, and approximate the flow of fluid properties between the boundaries of these cells using a finite difference method. In SPH, mass is discretised into particles and the force exerted on each particle by its near neighbours is approximated. In each of these two methods the resolution is tied to the method of discretisation. In grid codes the spatial resolution is fixed and the mass resolution varies, while the opposite is true in SPH. This means that SPH is highly suited to problems that are centred on dense regions, such as star formation (SF), since dense regions are intrinsically well resolved. GADGET (Springel et al., 2001), SEREN (Hubber et al., 2011), SWIFT (Schaller, Gonnet, Chalk & Draper, 2016), and PHANTOM (Price et al., 2018) are examples of SPH codes that have been designed specifically to perform astrophysical simulations. Astrophysical grid codes such as FLASH (Fryxell et al., 2000), RAMSES (Teyssier, 2001), and ENZO (Bryan et al., 2014) ensure improved resolution at high densities by using a method called adaptive mesh refinement (AMR) which subdivides the grid in regions of interest (Löhner, 1987; Berger & Colella, 1989).

While these two approaches have been used for the vast majority of numerical astrophysical simulations to date, there is a great deal of effort being put into hybrid schemes in an attempt to achieve the 'best of both worlds'. Two examples of this are AREPO (Springel, 2010) and GIZMO (Hopkins, 2015). The former uses a moving mesh around a Lagrangian set of particles that is constructed using Voronoi tessellations while the latter remains mesh free and uses a hydrodynamic Riemann solver to evaluate forces between each pair of particles. Both of these codes achieve better results for many problems in hydrodynamics but at the cost of greater computational expense.

2.1.2 Why use smoothed particle hydrodynamics?

Advantages

As described above SPH intrinsically resolves high density regions which is beneficial for simulations of SF. In AMR codes the expense to subdivide grids is high and low density cells still need to be evolved.

The Lagrangian scheme in SPH allows for the fluid's evolution to be tracked to a high precision since the location and properties of each particle can be tracked through the entire simulation history. An N-body implementation for gravity is rel-

atively straight forward owing to the particle nature of the code. Mass conservation is intrinsically conserved since all of the particles maintain a constant mass.

Disadvantages

The cell structure in AMR leads to the approximations being a sequence of matrix operations, this is simple to code and also lends itself very well to modern High-performance computing (HPC) architectures such as, vectorisation and graphics processing units (GPUs). By contrast SPH rarely performs operations on naturally contiguous data, although, the SPH code SWIFT (Schaller et al., 2016) has been designed with modern computer architectures in mind and is considerably faster but to date it lacks much additional physics. In SPH lists need to be maintained to assist the code to find particles quickly. Magnetohydrodynamics is more difficult to implement in SPH but this is not an aspect of this work. Radiative transfer is also more complex in SPH since lines of sight can be traced very easily through a fixed grid.

2.1.3 Codes used in this work

All of the results presented in this work derive from simulations performed using SPHNG, a highly parallel SPH code that originated from W. Benz (Benz, 1990; Benz et al., 1990). It has since been substantially modified (Bate, Bonnell & Price, 1995; Price & Monaghan, 2007) and has been parallelised using both OPENMP and the message passing interface (MPI). The code also includes implementations of radiative transfer, non-ideal MHD, and dust drag (Whitehouse, Bate & Monaghan, 2005; Whitehouse & Bate, 2006), but these elements are not relevant for this work. The SPH code PHANTOM (Price et al., 2018) was used for some early tests and benchmarking.

2.2 The fundamentals of SPH

SPH, first considered by Gingold & Monaghan (1977) and Lucy (1977), is a Lagrangian scheme that evolves the hydrodynamics of a system of gas particles by approximating the fluid properties of each particle by interpolation between other particles. Only a small subset of particles provide non-negligible contributions to the properties of the particle of interest; this subset is defined by a volume of compact support around each particle.

The process begins with finding the density of each particle (Sections 2.2.1 to 2.2.5) and then evaluating other quantities and the resulting forces on those particles (Sections 2.2.6 to 2.2.7). Then particles can be advanced using an appropriate numerical integrator combined with a time interval selection method (Section 2.2.11). In SPHNG this is achieved by looping over the particles twice, finding the density in the first loop and forces in the second loop.

2.2.1 Approximating density at a point

The density $\rho(\mathbf{r})$, at a position $\mathbf{r}$, in a continuous mass distribution $m(\mathbf{r})$ can be calculated exactly as,

$$\rho(\mathbf{r}) = \frac{\mathrm{d}m(\mathbf{r})}{\mathrm{d}V}, \tag{2.1}$$

where $\mathrm{d}V$ is the volume element associated with $\mathrm{d}m$. However, SPH does not provide a continuous mass distribution but rather a set of discrete point masses, hence we must instead interpolate a value from a subset of nearby point masses (b). In the absence of smoothing this can be approximated as the sum of particle masses within a volume of compact support (V) divided by that volume –

$$\rho(\mathbf{r}) = \frac{\sum_b m_b}{V}. \tag{2.2}$$

Such an approach is in practice flawed since the accuracy of the approximation is both poor in regions with high density gradients and overly sensitive to particles that fall just to one side of the boundary of the volume. Therefore contributions follow a functional dependence on the separation of the point to each particle in the subset ($|\mathbf{r} - \mathbf{r}_b|$). The function reduces the contribution from more distant particles and is denoted ($W(|\mathbf{r} - \mathbf{r}_b|, h)$), where h, known as the smoothing length, is used to define a region of compact support. This function is subsequently referred to as the smoothing kernel, its properties are described in the next section. This leads to the density estimator in SPH

$$\rho(\mathbf{r}) = \sum_b m_b W(|\mathbf{r} - \mathbf{r}_b|, h). \tag{2.3}$$

2.2.2 Nature of the smoothing kernel

The smoothing kernel must be a function that meets the following criteria (Gingold & Monaghan, 1982; Monaghan, 1992).

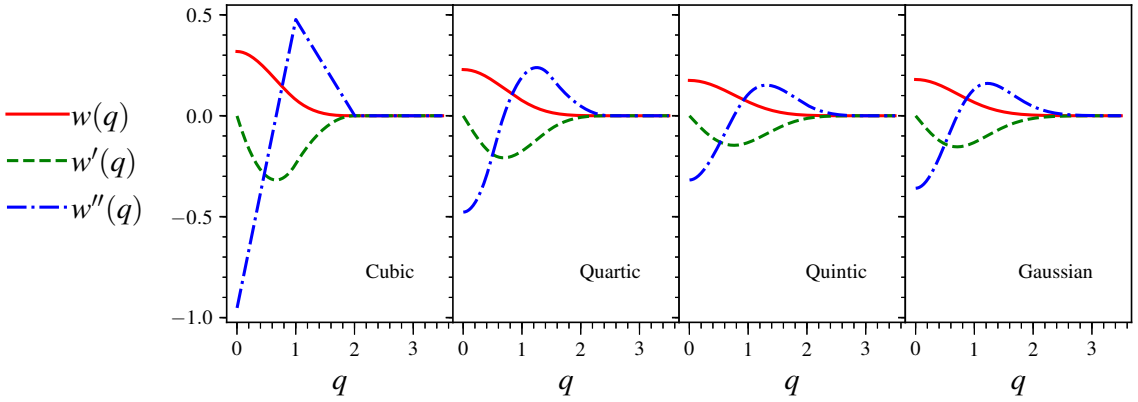

Figure 2.1. The cubic to quintic B-spline functions and a Gaussian function in 3 dimensions. The spline functions are truncated at radii of 2h, 2.5h and 3h respectively plotted in red (solid line), where h is the truncation radius. The corresponding first and second order derivatives are plotted in green (dashed) and blue (dot dashed) respectively.

1. It must have units of inverse volume.
2. It must monotonically decrease with increasing separation.
3. At low values of separation the gradient must be small to prevent small motions of nearby particles having too much impact on density.
4. It must have smooth derivatives.
5. It must be normalised such that its integral with respect volume over the whole volume is equal to unity

$$\int_V W(|\mathbf{r} - \mathbf{r}_b|, h)\, \mathrm{d}V = 1. \tag{2.4}$$

6. In the limit $h \to 0$ the smoothing kernel must tend to a dirac delta function

$$\lim_{h \to 0} W(|\mathbf{r} - \mathbf{r}_b|) = \delta(\mathbf{r} - \mathbf{r_b}). \tag{2.5}$$

An obvious choice of kernel function – that was used in early SPH (Gingold & Monaghan, 1977) – is the Gaussian; its form when normalised for 3-D SPH is,

$$W(|\mathbf{r} - \mathbf{r}_b|, h) = \frac{1}{\pi\sqrt{\pi}h^3} e^{-\frac{|\mathbf{r}-\mathbf{r}_b|^2}{2h^2}} \tag{2.6}$$

however, this does not intrinsically provide a truncation radius for compact support, even though h does allow the scale of the smoothing to be adjusted. Since Monaghan (1985) the Fourier transform generated B-spline functions (Schoenberg I. J., 1946) have predominantly been used. Of these, the M4 cubic spline is most common and is the only kernel function used in this work. The M5 quartic and M6 quintic splines

are employed for problems in which the smoothness of higher order derivatives is important since they are better approximations to the Gaussian as seen in Figure 2.1; they also have larger radii of compact support for equivalent h and are therefore more appropriate if a larger subset of particles is required for the density approximation (Price, 2012). The splines' truncation radii are calculated as ζh, with ζ being 2, 2.5 and 3 for the M4, M5 and M6 splines respectively.

The M4 cubic spline used in this work, not yet in its normalised form is

$$w(q) = \begin{cases} \frac{1}{4}(2-q)^3 - (1-q)^3, & 0 \geq q < 1; \\ \frac{1}{4}(2-q)^3, & 1 \geq q < 2; \\ 0. & q \leq 2, \end{cases} \tag{2.7}$$

where q is the ratio of the separation and smoothing length given by

$$q = \frac{|\mathbf{r} - \mathbf{r}_b|}{h}. \tag{2.8}$$

In this form the kernel function does not meet criteria 1 and 5.

2.2.3 Setting the smoothing length

In practice density approximations in SPH are made at the site of an individual gas particle (a); we will subsequently refer to the subset of particles within a's truncation radius as its neighbours. In early SPH the smoothing length was constant throughout a simulation, this led to a particle's number of neighbours being dependent on the local density. Gingold & Monaghan (1982) proposed inter-dependency between the smoothing length and density such that each particle has its own smoothing length that can be calculated directly from density as

$$h_a = \eta \left(\frac{m_a}{\rho_a} \right)^{1/3}, \tag{2.9}$$

where η is used to set the smoothing length scale and hence set a more consistent number of neighbours for every particle.

In three dimensions the number of neighbours is approximated by

$$N = \frac{4}{3}\pi(\zeta\eta)^3. \tag{2.10}$$

This work uses η of 1.2 and the cubic spline for the smoothing kernel which leads to

approximately 58 neighbours for each SPH particle. Poor choices of η can lead to instabilities, such as the pairing instability, details of which can be found in Price (2012).

The inter-dependence of h and ρ creates the need to simulataneously solve equations Equation 2.9 and Equation 2.12. In this work this is done using a Newton-Raphson solver backed up by a more computationally expensive bisection approach if the former fails.

2.2.4 Final estimate of density

Subsequently the subscript ab will be used to denote the difference between to quantities that individually have subscripts a and b e.g. $\mathbf{r}_a - \mathbf{r}_b$ becomes $\mathbf{r}_{ab}$ and similarly $|\mathbf{r}_a - \mathbf{r}_b|$ becomes r_{ab}. It is also used when expressing the kernel evaluated for particle a and one of its neighbours b such that $W(|\mathbf{r}_a - \mathbf{r}_b|, h_a)$ becomes $W_{ab}(h_a)$. Performing the integral in Equation 2.4 provides the normalisation constant $\frac{1}{\pi h^3}$ for the normalised cubic spline in three dimensions Equation 2.7 giving

$$W_{ab}(h_a) = \frac{1}{\pi h_a^3} w(q_{ab}), \tag{2.11}$$

where q_{ab} is $\frac{|\mathbf{r}_a - \mathbf{r}_b|}{h_a}$. At this point it is useful to re-write Equation 2.3 in its final form that approximates the density for particle a,

$$\rho(\mathbf{r}_a) = \sum_b m_b W_{ab}(h_a). \tag{2.12}$$

Now that density can be calculated from a set of neighbours it is necessary to find those neighbours as efficiently as possible.

2.2.5 Finding neighbours

The practical reality of finding each particle's neighbours is highly computationally expensive, $\mathcal{O}(N^2)$, without some form of optimisation. Typically SPH codes that do not include self gravity use a neighbour list approach to neighbour finding. In codes that do include self-gravity a tree structure for the particles is needed, in this case the tree is used for both gravity and neighbour finding. In this work the tree is also used for finding particles that overlap lines of sight to calculate column densities between two points for modelling photoionisation (Section 2.3.3).

In a neighbour list approach particles are grouped into a grid in which cells

have size $2h$, it is then only necessary to search a particle's own cell and each adjacent cell to guarantee finding all of the particle's neighbours. Linked lists of the particles in each cell are kept to optimise the search. Depending on the consistency of h throughout the simulation this can lead to order $\mathcal{O}(N)$ neighbour finding. Domínguez, Crespo, Gómez-Gesteira & Marongiu (2011) provide a good comparison of various neighbour list approaches.

There are several different tree based approaches to ordering the particles. In SPHNG, and hence this work, a binary tree is used (Press, 1986). To set up the binary tree all particles – the leaves of the tree – that share a mutual nearest neighbour are paired; the properties of each pair are combined into a node. The nodes, along with particles that have not yet been paired, are then passed through the same process until the final two nodes are paired into the root node. Each node stores the maximum possible radial extent of its most distant leaf (particle). The neighbour search 'walks the tree' ignoring any nodes for which the sphere of influence does not come within the truncation radius (ζh) of particle a.

Another commonly used tree structure in SPH is the oct-tree (Barnes & Hut, 1986) used by GADGET (Springel et al., 2001) and SEREN (Hubber et al., 2011). This method builds from the root node, splitting the entire domain into 8 cells recursively until only 1 or 0 particles are in a sub-domain. Tree method neighbour finding is of order $\mathcal{O}(N \log N)$. Makino (1990) present a useful comparison of these two tree methods.

2.2.6 Finding other quantities

To find other quantities, SPH uses the interpolation theory described by Lucy (1977), Gingold & Monaghan (1977, 1982) and, Monaghan (1985). In this theory the exact interpolant for any given quantity A, at a point, is given by

$$A(\mathbf{r}) = \int A(\mathbf{r}')\delta(\mathbf{r} - \mathbf{r}')\,\mathrm{d}\mathbf{r}', \tag{2.13}$$

where δ denotes the Dirac delta function. An approximation of this equation is made by replacing the delta function with the smoothing kernel, hence the need for the final constraint on the kernel given in Section 2.2.2. The integral interpolant therefore becomes

$$A(\mathbf{r}) = \int \frac{A(\mathbf{r}')}{\rho(\mathbf{r}')} W(\mathbf{r} - \mathbf{r}', h)\rho(\mathbf{r}')\,\mathrm{d}\mathbf{r}'. \tag{2.14}$$

Since $\rho(\mathbf{r}')\,\mathrm{d}\mathbf{r}'$ can be approximated as the sum of all m_b in a summation approximation, the summation interpolant for SPH is,

$$A_a = \sum_b m_b \frac{A_b}{\rho_b} W_{ab}(h_a). \tag{2.15}$$

For $A_b = \rho_b$ this equation becomes Equation 2.12 demonstrating that the density estimate described in Section 2.2.1 yields the same result as the interpolation theory.

No properties of an SPH particle are dependent on the particle's spatial coordinates, but only on relative positions to their neighbours. This means that any differential of a particle quantity will be zero. This leads to the advantage that to differentiate an interpolant only the kernel need be operated on, which can be done analytically. Therefore the associated product rule can be used to express the gradient, divergence, and curl summation interpolants as

$$\nabla A_a = \sum_b m_b \frac{A_b}{\rho_b} \nabla W_{ab}(h_a), \tag{2.16a}$$

$$\nabla \cdot \mathbf{A}_a = \sum_b m_b \frac{\mathbf{A}_b}{\rho_b} \cdot \nabla W_{ab}(h_a), \quad \text{and} \tag{2.16b}$$

$$\nabla \times \mathbf{A}_a = \sum_b m_b \frac{\mathbf{A}_b}{\rho_b} \times \nabla W_{ab}(h_a). \tag{2.16c}$$

2.2.7 Equations of fluid dynamics

Once the density has been found the equations of hydrodynamics need to be solved within the chosen formalism of SPH, in this case that of SPHNG. SPHNG solves the same set of equations as PHANTOM (Price et al., 2018). The three central equations of fluid dynamics, discussed in the next three sections, are Lagrangian derivatives of a scalar or vector field. The Lagrangian derivative gives the flow rate of a fluid property A, as a function of both position and time. It takes the form

$$\frac{\mathrm{d}A}{\mathrm{d}t} = \frac{\partial A}{\partial t} + \mathbf{v} \cdot \nabla A, \tag{2.17}$$

where $\mathbf{v}$ is the velocity of the fluid[1]. This is a good moment to re-iterate that SPH is a Lagrangian scheme in which the properties of a moving fluid element are tracked. Whereas Eulerian schemes describe how the properties of a fixed location vary over

[1]It is worth noting that the Lagrangian derivative goes by many names: substantial, advective, convective, particle, and hydrodynamic derivative being a few. It is also commonly notated with a capitalised differential operator, $\frac{\mathrm{D}}{\mathrm{D}t}$.

time. Equation 2.17 can act as a link between the two schemes.

Rosswog (2009) derives the mass, momentum and energy equations from the Lagrangian of a perfect fluid, the first law of thermodynamics, and the interpolation scheme described above. This Lagrangian takes the form

$$L = \int \rho \left(\frac{v^2}{2} - u(\rho, s) \right) \mathrm{d}V, \tag{2.18}$$

where u is the internal energy and s is the entropy of a fluid element. The solutions take the form of summations over pairs of particles; The derivations presented here are for a fixed smoothing length and give an idea of how the interpolation scheme is applied to find gradients. SPHNG, however, follows a variable h formalism, i.e. the particle pairs in the summations do not share a value of h. This means that additional, 'grad-h', terms are required. Every particle is assigned an Ω value which accounts for the variation in the gradient of h, across all of its neighbours. This value is calculated as,

$$\Omega_a = 1 - \frac{\partial h_a}{\partial \rho_a} \sum_b m_b \frac{\partial W_{ab}(h_a)}{\partial h_a}, \tag{2.19}$$

and it is derived along with the complete solutions in Rosswog (2009). We present the solutions for the variable h formalism after the derivations for the fixed h approach. The Ω values for every particle are calculated during the density loop so that they are available throughout the force loop.

2.2.8 Mass equation

The mass equation or continuity equation

$$\frac{\mathrm{d}\rho}{\mathrm{d}t} = -\rho \nabla \cdot \mathbf{v}, \tag{2.20}$$

gives the rate of change of density for a fluid element. There is no need to solve this to evolve a particle's density since density is calculated directly from the particle positions using Equation 2.3. However, the solution is used in Section 2.2.10 so it is included here.

Applying the golden rule of SPH (Monaghan, 1992), by expanding with the product rule such that the density ends up inside the operators, means that the

right hand side of Equation 2.20 can be expressed as

$$-\rho\nabla\cdot\mathbf{v} = \nabla\cdot(\rho\mathbf{v}) - \mathbf{v}\cdot(\nabla\rho). \tag{2.21}$$

Then discretising with the corresponding summation interpolants (Equations 2.16a and 2.16b) we get,

$$\frac{\mathrm{d}\rho_a}{\mathrm{d}t} = -\sum_b m_b\mathbf{v}_b\cdot\nabla W_{ab}(h_a) - \sum_b m_b\mathbf{v}_a\cdot\nabla W_{ab}(h_a), \tag{2.22}$$

which can be expressed as,

$$\frac{\mathrm{d}\rho_a}{\mathrm{d}t} = -\sum_b m_b\mathbf{v}_{ab}\cdot\nabla W_{ab}(h_a), \tag{2.23}$$

where $\mathbf{v}_{ab}$ is shorthand for $\mathbf{v}_b - \mathbf{v}_a$.

2.2.9 Momentum equation

The flow of momentum in fluid dynamics is described by the Navier Stokes equation, also known as the Euler equation. In general it is dependent on pressure, viscosity, and gravitational terms and is given by

$$\frac{\mathrm{d}\mathbf{v}}{\mathrm{d}t} = -\frac{\nabla P}{\rho} - \nu\nabla^2\mathbf{v} + \nabla\Phi_g, \tag{2.24}$$

where P is pressure, ν is the kinematic viscosity of the fluid, and Φ_g is the gravitational potential.

Pressure

If the gradient summation interpolant (Equation 2.16a) is substituted for ∇P a trivial solution is reached. While this solution yields good results for many hydrodynamical problems it violates Newton's 3$^{\mathrm{rd}}$ law. It is therefore more common to again apply the golden rule of SPH and expand the term, this time via the quotient rule. This yields a result that conserves momentum by ensuring that pressure forces arise in pairs

$$\frac{\nabla P}{\rho} = \frac{P}{\rho^2}\nabla\rho + \nabla\left(\frac{P}{\rho}\right). \tag{2.25}$$

Substituting the gradient summation interpolant (Equation 2.16a) for $\nabla(P_a/\rho_a)$ and $\nabla\rho_a$ gives the acceleration of an SPH particle in a non-viscous fluid in the absence

of gravity,

$$\frac{\mathrm{d}\mathbf{v}_a}{\mathrm{d}t} = \frac{P_a}{\rho_a^2}\sum_b m_b \nabla W_{ab}(h_a) + \sum_b \frac{m_b P_b}{\rho_b^2}\nabla W_{ab}(h_a). \tag{2.26}$$

This can be expressed as follows by placing all quantities inside the summations,

$$\frac{\mathrm{d}\mathbf{v}_a}{\mathrm{d}t} = -\sum_b m_b \left(\frac{P_a}{\rho_a^2} + \frac{P_b}{\rho_b^2}\right)\nabla W_{ab}(h_a). \tag{2.27}$$

The solution in the case of variable smoothing length, including terms for viscosity and gravity becomes

$$\frac{\mathrm{d}\mathbf{v}_a}{\mathrm{d}t} = -\sum_b m_b \left(\frac{P_a}{\rho_a^2\Omega_a}\nabla W_{ab}(h_a) + \frac{P_b}{\rho_b^2\Omega_b}\nabla W_{ab}(h_b)+\right) + \Pi_{\mathrm{AV}} + \nabla\Phi_g, \tag{2.28}$$

where Ω_a is defined in Equation 2.19 and Π_{AV} is an artificial viscosity term discussed later in this section.

Gravity

It is vital to be aware, when evaluating gas-gas gravitational forces in SPH, that the particles do not represent point masses but are interpolation points that approximate to a continuous distribution of gas. If a particle resides inside the smoothing length of another, the overlap of the gas mass that the particle pair represents must be considered. This is done through the use of gravitational force softening, described in Dehnen (2001), the variable smoothing length case is discussed by Price (2007). Here only the equations that are required to recreate the approach used by SPHNG are presented.

Force and potential kernels are derived from the smoothing kernel, $w(q)$, in this case the cubic spline (Equation 2.7). The force kernel is calculated as

$$F(q) = \frac{4}{q^2h^2}\int_0^q w(q')q'^2 dq', \tag{2.29}$$

and the potential kernel is calculated from the force kernel as

$$\phi(q) = h\int F(q)dq. \tag{2.30}$$

The constants of integration, set by the boundary condition that $\phi \to 0$ as $r \to \infty$, are $-\frac{7}{5}, -\frac{8}{5}$, and 0 for q $0 \leq q < 1, 1 \leq q < 2$, and $q \geq 2$ respectively for the M4 cubic spline. It is worth pointing out that these kernels simplify to $\frac{1}{r^2}$ and $-\frac{1}{r}$ respectively

in the case that $q \geq 2$.

The gravitational contribution to the SPH momentum equation is given by

$$\nabla\Phi_g = -G\sum_b m_b \left[\frac{F_{ab}(h_a) - F_{ab}(h_b)}{2}\right]\hat{\mathbf{r}}_{ab} - \frac{G}{2}\sum_b m_b \left[\frac{\zeta_a}{\Omega_a}\nabla W_{ab}(h_a) + \frac{\zeta_b}{\Omega_b}\nabla W_{ab}(h_b)\right], \tag{2.31}$$

where G is the gravitational constant and ζ is the gradient of the variable softening length given by,

$$\zeta_a = \frac{\partial h_a}{\partial \rho_a}\sum_b m_b \frac{\partial \phi_{ab}(h_a)}{\partial h_a}. \tag{2.32}$$

The first term in Equation 2.31 is the softened gravitational force; the second term is a result of variable smoothing lengths and also leads to improvements in force accuracy at low resolution and energy conservation, both of which are discussed in detail in Price (2007).

The contributions of particles at large separations are calculated using the binary tree described in Section 2.2.5. Using the particle groups already existing in the tree's node structure to reduce the number of force components that need to be summed. The additional forces that arise from cluster sink particles (Section 2.2.12) are dealt with by direct N-body summation.

Artificial viscosity

The treatment of shocks produces problems in numerical hydrodynamics. Shocks lead to discontinuities in the simulated fluid that are only present because, inevitably, the fluid is not resolved down to the length scale of the mean free path of the gas. Viewed on a small enough scale any fluid pressure gradient will be seen to be continuous; this is is a result of the viscosity present in all non-ideal fluids. The impact of unresolved viscosity on the macroscopic scale of any simulation must be found using a sub-grid approximation commonly known as artificial viscosity. SPHNG imposes an artificial viscosity term that adds additional pressure terms to the fluid equations. This approach was first suggested by VonNeumann & Richtmyer (1950) and is the most commonly used approach in SPH. SPHNG uses the formulation described by Monaghan (1997), it is as follows,

$$\Pi_{AV} = -\sum_b \frac{m_b}{\rho_{ab}^2}\left[\frac{q_{ab}^a}{\Omega_a}\nabla W_{ab}(h_a) + \frac{q_{ab}^b}{\Omega_b}\nabla W_{ab}(h_b)\right] \tag{2.33}$$

where ρ_{ab} is the mean density of particles a and b and the q terms are given by,

$$q^a = \begin{cases} -\frac{1}{2}\rho_a v_{\text{sig}.a}\mathbf{v}_{ab}\cdot\hat{\mathbf{r}}_{ab}, & \mathbf{v}_{ab}\cdot\hat{\mathbf{r}}_{ab} < 0 \\ 0 & \text{otherwise,} \end{cases} \tag{2.34}$$

where the signal velocity is,

$$v_{\text{sig}} = \alpha_{AV}c_s + \beta_{AV}|\mathbf{v}_{ab}\cdot\hat{\mathbf{r}}_{ab}|, \tag{2.35}$$

where α_{AV} is 1, β_{AV} is 2 and c_s is the sound speed. In the simplest sense this means that artificial viscosity applies dissipation of kinetic energy in the case that two particles are approaching each other, and does nothing when they are moving apart. This dissipation leads to a corresponding increase in the interanl energy of the gas, this is discussed at the end of the next section.

2.2.10 Energy equation

The first law of thermodynamics gives the change in energy of a fluid element as $\mathrm{d}U = \mathrm{d}Q - P\,\mathrm{d}V$, where $\mathrm{d}Q$ is the energy exchanged with the element's surroundings and $P\,\mathrm{d}V$ the work done. In SPH it is more convenient to divide this equation by mass since the system consists of a set of discrete masses. Initially ignoring the first term, and only considering an adiabatic equation of state the first law can be re-written as

$$\frac{\mathrm{d}u}{\mathrm{d}t} = \frac{P}{\rho^2}\frac{\mathrm{d}\rho}{\mathrm{d}t}, \tag{2.36}$$

where u is energy per unit mass and $1/\rho$ is substituted for V/m. This is discretised by substituting the solution to the continuity equation (Equation 2.23) as follows,

$$\frac{\mathrm{d}u_a}{\mathrm{d}t} = \frac{P_a}{\rho_a^2}\sum_b m_b\mathbf{v}_{ab}\cdot\nabla W_{ab}(h_a) + \frac{\mathrm{d}u_a^{\text{diss}}}{\mathrm{d}t} + \frac{\mathrm{d}u_a^{\text{ISM}}}{\mathrm{d}t}, \tag{2.37}$$

where u_a^{diss} and u_a^{ISM} are non adiabatic heat exchange terms for artificial dissipation and interstellar medium (ISM) physics respectively. The dissipation term is a result of artificial viscosity discussed in Section 2.2.9 and is given by,

$$\frac{\mathrm{d}u_a^{\text{diss}}}{\mathrm{d}t} = \frac{1}{2}\sum_b m_b\Pi_{ab}\mathbf{v}_{ab}\cdot\nabla_a W_{ab}(h_a). \tag{2.38}$$

The ISM term is covered in more detail in Section 2.3.1. Now that all the quantities' rates of change can be estimated it is time to advance the system in time.

2.2.11 Evolving the system

The system is evolved by using an integration scheme to approximate the solutions to the equation of motion,

$$\mathbf{a} = \dot{\mathbf{v}} = \ddot{\mathbf{r}}, \tag{2.39}$$

numerically. An appropriate time interval – timestep – needs to be chosen at which to perform this integration. The choice of this timestep needs to be a carefully selected balance between accuracy and computational speed. In this section the terms force and acceleration are interchangeable since all SPH particles have the same mass.

Choosing timesteps

In these simulations three key constraints on the timestep are considered: the maximum velocity at which hydrodynamical effects can propagate, the magnitude of the forces on a particle, and the rate of change of internal energy.

The Courant-Friedrichs-Lewy (CFL) condition (Courant, Friedrichs & Lewy, 1928), which is ubiquitous in timestepping numerical differential equation solvers, determines the hydrodynamic timestep. The timestep is set as

$$\Delta t_{\mathrm{CFL}} = C_{\mathrm{CFL}} \left(\frac{h}{v_{|\mathrm{sig}|}} \right), \tag{2.40}$$

where $v_{|\mathrm{sig}|}$ is the signal velocity and C_{CFL} is the Courant number which is set at 0.3 in SPHNG.

The force condition, calculated from the ratio of smoothing length to the maximum acceleration magnitude (F_{max}) on a particle, is given by

$$\Delta t_{\mathrm{F}} = C_{\mathrm{F}} \sqrt{\frac{mh}{|\mathbf{F}_{\mathrm{max}}|}}, \tag{2.41}$$

where C_{F} is 0.3 and m is the particle mass. This condition reduces the timestep of high acceleration particles for which increasing velocities could make Δt_{CFL} too high.

In a purely hydrodynamic scheme there is no need to have an additional criterion for internal energy (U). However, these simulations include additional physics for

heating and cooling processes in the ISM (Glover & Mac Low, 2007) which we discuss in Section 2.3.1. As a result the internal energy can vary at a higher rate than with hydrodynamics alone necessitating the need for a check of the relative rate of change in internal energy in the previous timestep

$$\Delta t_{\rm therm} = C_{\rm therm} \left| \frac{U}{\dot{U}} \right|, \tag{2.42}$$

where $C_{\rm therm}$ is 0.05. Glover & Mac Low (2007) suggest a guide value of 0.3 but simulations with feedback require a more robust choice owing to the resulting rapid changes in temperature.

The timestep for each particle is set as the minimum of each of the above conditions,

$$\Delta t_{\rm min} = \min\left(\Delta t_{\rm CFL}, \Delta t_{\rm F}, \Delta t_{\rm therm}\right). \tag{2.43}$$

Either a 'global timestep', the minimum $\Delta t_{\rm min}$ across all particles, can be set, or each particle can be evolved on its own 'individual timestep'.

Integration scheme

Many integration schemes for advancing particles have been used in SPH, the two most common are the leapfrog approach and Runge-Kutta methods. The leapfrog approach advances particles by one times step using the velocities calculated at the midpoint position, hence the position and velocity calculations 'leapfrog' each other.

The SPHNG code uses a first order Runge-Kutta-Fehlberg integrator (Fehlberg, 1969) to integrate a set of ordinary differential equations with respect to time. The first step is to evaluate k_0, the rate of change of particle quantities (discussed in Section 2.2.7) at t_0, the start of the timestep,

$$k_0 = \dot{\mathbf{A}}(t_i, \mathbf{A}_i), \tag{2.44}$$

where i is the timestep counter and A continues to be some particle quantity. The particles' predicted quantities at half timestep are then calculated using the rate of change from Equation 2.44 and the derivatives are then re-evaluated as,

$$k_1 = \dot{\mathbf{A}}(t_i + \frac{\Delta t_{\rm g}}{2}, \mathbf{A}_i \frac{\Delta t_{\rm g}}{2}). \tag{2.45}$$

This makes k_1 the predicted gradient at a half timestep.

Improved estimates of the derivatives are calculated using a weighted average of

k_0 and k_1 and used to update particle quantities for the entire timestep

$$\mathbf{A}_{i+1} = \mathbf{A}_i + \left(\frac{1}{256}k_0 + \frac{255}{256}k_1\right)\Delta t_{\mathrm{g}}. \tag{2.46}$$

An advantage of the Runge-Kutta-Fehlberg integrator is that the third term in the equivalent second order integrator is equivalent to the k_0 on the following timestep. While SPHNG strictly speaking uses a first order integrator, it gains additional accuracy by using second order terms to calculate error and shorten subsequent timesteps if appropriate.

Individual timesteps

In an individual timestep scheme all particles are advanced at intervals appropriate for their own environment. In SPHNG a maximum time interval (Δt_{max}) is chosen in advance of the simulation; Δt_{max} is divided into a set of 30 binary bins allowing the smallest individual timestep bin to be $\approx 10^9$ times smaller than Δt_{max}. At any point between t and $t + \Delta t_{\mathrm{max}}$ each particle is classed as active or inactive depending on its own Δt_{min}.

The integration scheme for individual timesteps is unchanged but it is important when calculating forces to ensure that all inactive particles that are neighbours of active particles are temporarily moved to the current time before calculating derivatives. Predictions are made using the last calculated forces for each particle. In a simple realisation of SPH, advancing particles is an $\mathcal{O}(N)$ expense compared to $\mathcal{O}(N \log N)$ for calcualting forces. i.e. forces are only updated for an individual particle's Δt_{min} but all particles are advanced using their last calculated force at the smallest Δt_{min} of their neighbours.

A consequence of this is that all particles are only advanced to an equivalent time at intervals of Δt_{max}. Therefore Δt_{max} is the minimum time interval that data on all particles can be extracted from the simulation.

2.2.12 Sink particles

Simulations of star formation span many order of magnitudes in density. It is simply not possible to model gas once it reaches densities typical within stars. The numerical hydrodynamics community overcome this problem through the use of sink particles (Bate et al., 1995), which are a sub-grid approach combining the properties of many gas particles into a sink particle. Sink particles only interact with each other and gas particles through gravity. A set of boundary conditions is applied around

sink particles to mitigate the lack of pressure exerted on neighbouring gas.

On the scale of the simulations presented in this work, each sink particle represents a cluster or sub-cluster of stars, hereafter when we refer to sink particles we are referring to cluster sink particles. The sink particles form as described in Bate et al. (1995), whereby gas particles are tested once they exceed a threshold density, and a sink particle is created if the following conditions are satisfied for the ≈ 50 SPH neighbours:

1. ratio of thermal to gravitational energies is $\leq \frac{1}{2}$.
2. the sum of the thermal and rotational energies over the gravitational energy is ≤ 1.
3. total energy of the particles is negative.
4. divergence of the particles' accelerations must be negative.

The critical number density, the maximum density at which the Jeans mass can be resolved (Bate & Burkert, 1997), is 1.2×10^4 cm^{-3} at a temperature of 30 K in the HR runs. We use this as the threshold density in all our simulations, however, we find that gas routinely exceeds this threshold without forming sink particles, as it does not meet the other criteria listed above. We therefore also introduce a second criteria of 1.2×10^6 cm^{-3} where automatic sink creation occurs, preventing gas densities becoming exceptionally high. In reality we would expect that star formation would occur at these densities, but potentially we lack the resolution such that gas in a region matches all the criteria listed above.

The Jeans radius for gas at this density in the SR initial conditions is 0.45 pc which is the accretion radius we used in the SR_2 runs. A larger accretion radius, and hence sink particle resolution, of 0.78 pc is used in the SR and HR runs.

The close approach of sink particles leads to very short timesteps and hence considerable computational expense, particularly in runs containing many sink particles. To avoid this we use a relatively large separation criterion at which sink particles are merged of 0.01 pc. Since stellar dynamics are of secondary interest in this work, we consider the resulting decrease in computational cost a reasonable payoff for the loss in sink dynamics.

2.3 Additional physics

Such simulations require the addition of carefully selected physics including gravity, chemistry, and radiation transport. All of the simulations presented in this work were completed using SPH; in this chapter we lay our motivations for its use, its

methodology and details of the implementation of additional physics.

2.3.1 Heating, cooling and galactic potential

We use the same galactic potential, heating and cooling as Dobbs & Pringle (2013). The potential includes a logarithmic component which produces a flat rotation curve (Binney & Tremaine, 2008) and a two armed spiral perturbation (Cox & Gomez, 2002). Full details of the potentials are also provided in Dobbs et al. (2006). Self gravity is included in all the simulations presented in this work.

The heating and cooling of the ISM are described in Dobbs et al. (2008), which is based on the work of Glover & Mac Low (2007). The method accounts for the following cooling processes: fine-structure emission lines of C^+,O and Si^+, ro-vibrational emission from H_2, gas-grain energy transfer and recombination on grain surfaces. We also consider collisional dissociation of H_2, the collisional ionisation of atomic hydrogen and emission from atomic resonance lines and bremsstrahlung. The heating processes include, photoelectric emission from dust grains, H_2 photodissociation, and the pumping of excited vibrational states of H_2 by the background ultraviolet field or during the formation process of the molecules.

The code tracks the abundances of Ionised hydrogen (p), electrons(e^-), carbon monoxide (CO), atomic hydrogen (H), and molecular hydrogen (H_2). The changes in abundance of H_2 and the resultant self-shielding are applied as described in Bergin, Hartmann, Raymond & Ballesteros-Paredes (2004). For the shielding we use a constant length scale of 35 pc, which is in line with the progenitor simulations. The treatment of CO is covered in Nelson & Langer (1999).

We use an assumed ionised gas temperature of 10^4 K for gas ionised as a result of photoionisation, this is discussed in more detail in Section 2.3.3.

2.3.2 Sampling of massive stars

To account for ionisation we need to track the formation of massive stars in our simulation. To do this, we sample 3×10^6 $M_\odot$ using a Kroupa (2001) initial mass function (IMF) into mass bins using the approach presented by Sormani, Treß, Klessen & Glover (2017). Our bin boundaries are defined such that the representative mass of each bin corresponds to the 15 luminosity class V stars presented by Sternberg et al. (2003), with a 16^{th} bin for all less massive stars. Ignoring the 16^{th} bin gives us a pre-sampled list of bin numbers (1-15) of stars above 18 $M_\odot$, where each bin has an associated ionising flux. We have re-created the relevant parts of the table

Table 2.1. Data from Sternberg et al. (2003) along with the bin boundaries used. The upper bin boundaries correspond to the lower bin boundaries for the previous bin number. Q_h is the representative ionising flux of a star in a given bin, we ignore ionisation from stars in the 16^{th} bin.

Bin number	Spectral type	Representative bin mass [$M_\odot$]	Upper bin boundary [$M_\odot$]	$\log Q_h$ [$\log s^{-1}$]
1	O3	87.6	107.5	49.87
2	O4	68.9	72.8	49.68
3	O4.5	62.3	65.5	49.59
4	O5	56.6	59.5	49.49
5	O5.5	50.4	53.7	49.39
6	O6	45.2	47.7	49.29
7	O6.5	41.0	43.0	49.18
8	O7	37.7	39.3	49.06
9	O7.5	34.1	36.0	48.92
10	O8	30.8	32.4	48.75
11	O8.5	28.0	29.4	48.61
12	O9	25.4	26.7	48.47
13	O9.5	23.3	24.3	48.26
14	B0	21.2	22.2	48.02
15	B0.5	19.3	20.3	47.71
16	All other	0.3	18.4	N/A

from Sternberg et al. (2003) in Figure Table 2.1 along with our bin boundaries.

Similarly to Geen, Watson, Rosdahl, Bieri, Klessen & Hennebelle (2018) we define ΔM_i, the massive star injection interval, as the total mass of all stars in the pre-sampled list (stars <18 $M_\odot$) over the total mass of the sample (3×10^6 $M_\odot$). Every time the total sink particle mass in a simulation passes a multiple of ΔM_i, we inject the next massive star in the pre-sampled list. Each injected massive star is assigned to the sink particle with the greatest mass made up of stars less than 18 $M_\odot$; if there is no sink particle massive enough to accommodate the star then injection is delayed.

2.3.3 Photoionisation

Theory

The ionisation of a uniform-cloud cloud of HI was studied first by Strömgren (1939), then by Kahn (1954), and subsequently by many others. Kessel-Deynet & Burkert (2000) and Dale, Ercolano & Clarke (2007b) both presented methods for modelling photoionisation within the SPH method based on computing the Strömgren radius

along lines of sight. Dale et al. (2007b) improved the basic method to take account of the fact that in a dynamical situation, neutral gas may enter an HII region from outside, and ionised gas may leave an HII region or be cut-off from the supply of photons that keep it from recombining. The method presented below follows the basic method of Dale et al. (2007b), with some modifications primarily to do with how the line of sight integrals are calculated.

If an ionising source is placed in a cloud of neutral hydrogen, the ionising photons cause an ionisation front (IF) to propagate outward from the source at highly supersonic speed leaving behind an HII region. This is known as the R-type expansion phase. Taking hydrogen with number density n, if the gas is fully ionised the number densities of ions and electrons are $n_{\rm i} = n_{\rm e} = n$. The recombination rate per unit volume is then $\alpha n_{\rm i} n_{\rm e} = \alpha n^2$, where α is the recombination coefficient. SPHNG considers any photon whose energy exceeds 13.6 eV as ionising and defines the ionising photon luminosity as $Q_{\rm H}$ (measured in ionising photons emitted per unit time). For a static cloud surrounding an ionising source with an arbitrary radial density profile and consisting of fully ionised hydrogen (i.e. within the HII region), the flux of ionising photons passing through radius r can be written as

$$4\pi r^2 F(r) = Q_{\rm H} - 4\pi \int_0^r r'^2 n(r')^2 \alpha_{\rm B} {\rm d}r', \tag{2.47}$$

which accounts for geometric dilution of the ionising photons and the photons required to balance recombination of ionised gas. In setting the recombination rate, the 'on-the-spot' (OTS) approximation is used which assumes that photons produced from recombinations directly to the hydrogen ground state are re-absorbed within the HII region. The ionising photons produced by such recombinations are assumed to be absorbed elsewhere and not to contribute to the local ionisation equilibrium. Thus, we take the temperature-dependent 'case B' recombination coefficient to be $\alpha_{\rm B} = 2.7 \times 10^{-13}$ cm^3 s^{-1}. This is justifiable when the optical depth of the HII region to secondary ionising photons is smaller than the dimensions of the HII region.

As the IF expands into neutral gas, the integral in Equation 2.47 becomes equal to $Q_{\rm H}$ and the IF cannot proceed any further. In a uniform-density cloud, $n = n_0$, the radius at which this happens is known as the Strömgren radius which is defined by integration of the above equation

$$R_{\rm S} = \sqrt[3]{\frac{3Q_{\rm H}}{4\pi n_0^2 \alpha_{\rm B}}}. \tag{2.48}$$

Later expansion is driven by the pressure difference between the ionised gas and the surroundings and is known as D-type expansion.

Equation 2.47 gives the net ionising flux as a function of radius if the intervening gas is fully ionised. However, it will not capture the time dependence of the initial R-type expansion phase. Neither will it treat the case of neutral gas entering the intervening region where some ionising photons will be used up ionising the intervening gas, or if the ionising source is reduced or blocked.

Instead, following Dale et al. (2007b), the number of ionising photons that passes through radius r in time δt can be written in the form

$$\delta t \left(Q_{\rm H} - 4\pi \int_0^r r'^2 \; n(r')^2 \alpha_{\rm B} {\rm d}r' \right) - 4\pi \int_0^r r'^2 n(r')[1 - H_{\rm II}(r')]{\rm d}r', \tag{2.49}$$

where $H_{\rm II}$ is the ionisation fraction of the gas (from 0 to 1).

Finally, ionised gas that is not subject to ionising radiation will recombine and eventually cool. we take the characteristic timescale for the recombination to be $(\alpha_{\rm B} n)^{-1}$.

Implementation

The main difference between this method and that of Dale et al. (2007b) is the way in which the integrals along the line of sight between the ionising source and a particular gas particle are calculated. Dale et al. (2007b) used a method similar to that developed by Kessel-Deynet & Burkert (2000) which approximates the integrals using the density and ionisation state of the closest SPH particles to the line of sight. Instead, SPH interpolation is used to determine the line of sight integrals using all SPH particles whose smoothing lengths overlap with the line of sight. This is done by walking the tree structure that is used to determine SPH neighbours and self-gravity. For example, the second integral in Equation 2.49 becomes

$$\int_0^r r'^2 n(r')[1 - H_{\rm II}(r')]{\rm d}r' = \sum_j r_j^2 \chi(x_j, h_j) \frac{2 m_j}{\mu m_{\rm H} h_j^2} (1 - H_{{\rm II},j}), \tag{2.50}$$

where μ is the mean molecular weight of the unionised molecular gas, and $m_{\rm H}$ is the mass of a hydrogen atom. The sum is done over all particles that overlap with the line of sight from the ionising source to the particle in question, r_j is the distance

from the ionising source to particle j, and m_j, h_j, and $H_{\mathrm{II},j}$ are the mass, smoothing length, and ionisation fraction of particle j, respectively. The function $\chi(x_j, h_j)$ is the line integral through the SPH kernel function $W(r_j, h_j)$ at an impact parameter of x_j divided by the radius of the smoothing kernel (e.g. $2h_j$).

For each gas particle, the ionisation fraction is evolved as

$$\frac{\mathrm{d}H_{\mathrm{II}}}{\mathrm{d}t} = \frac{h^2}{r^2}\left(\frac{Q_{\mathrm{H}}}{4\pi} - \int_0^r r'^2 n(r')^2 \alpha_{\mathrm{B}} \mathrm{d}r' - \frac{1}{\delta t}\int_0^r r'^2 n(r')[1 - H_{\mathrm{II}}(r')]\mathrm{d}r'\right), \tag{2.51}$$

as long as this quantity is positive. The factor h^2/r^2 accounts for the fact that the ionising flux is distributed over 4π steradians and only a fraction of this is intercepted by a particular SPH particle. Although an SPH particle has a total extent given by the SPH kernel (which, for the standard cubic spline has a radius of $2h$), these regions overlap so, although the effective solid angle subtended by the particle should scale as h^2, the coefficient is unclear. Empirically we find that h^2 gives good results (Section 2.3.4).

For gas particles for which the net change in ionised fraction is zero, we set

$$\frac{\mathrm{d}H_{\mathrm{II}}}{\mathrm{d}t} = -n\alpha_{\mathrm{B}} H_{\mathrm{II}}^2. \tag{2.52}$$

This allows ionised gas that does not receive ionising flux to recombine.

The columns for every particle-to-sink line of sight below a distance threshold are calculated, and H_{II} values are evolved, on the same individual timesteps as all other derivatives. The distance threshold can be set dependent on the nature of a simulation. Long range radiation is more important in the inter-arm where there is less dense gas and larger distances between Giant molecular clouds (GMCs).

Photoionisation affects the hydrodynamics of the gas via heating. We apply a minimum temperature calculated as the ionised gas fraction of a particle by 10^4 K if the particle has received any amount of ionising flux within its last timestep. HII regions are typically observed to have temperatures from 8,000 to 11,000 K (Baldwin et al., 1991; Jamet et al., 2005; Rodríguez & García-Rojas, 2010) and similar temperatures are found in simulations that consider all of the heating and cooling processes arising from photoionisation (Haworth & Harries, 2012).

Multiple ionising sources

Photoionisation from multiple sources is treated by summing the positive contributions to fractional change in $H_{\rm II}$ from all ionising sink particles. Some line of sight methods track the number of ionising sources that contribute flux to each ionised gas particle. Then the contribution to column densities of particles that receive contributions from more than a single source can be reduced appropriately. This leads to significant additional computational expense since the column densities need to be iteratively solved down to some tolerance. An alternative to iteration is to use the number of ionising sources from the previous timestep, we plan to implement this in the future.

Optimisation and parallelisation

Many attempts have been made to optimise radiative transfer methods. Two examples are TREVR (Grond, Woods, Wadsleyand & Couchman, 2019), which is designed to be implemented with any AMR or SPH code, and FERVENT (Baczynski, Glover & Klessen, 2015), a module for the FLASH AMR code.

TREVR uses a gas tree structure to estimate column densities without needing to sum the contributions of every individual particle. It also uses a sink particle tree to adaptively group sinks if the distance between them is small relative to the line of sight. However, since this means that the number of sources irradiating any given particle between timesteps is variable the multiple source approximation used to avoid iteration discussed in Section 2.3.3 cannot be applied.

FERVENT calculates column densities along HEALPIX (Gorski, Hivon, Banday, Wandelt, Hansen, Reinecke & Bartelmann, 2005) rays moving out radially from each source. At large distances from the sources one ray contains the column densities for many cells. For any given cell all that then remains is to determine the HEALPIX ray it is in, and the column density can be found trivially. This means there is an overhead expense for each timestep to find the HEALPIX rays.

Our method does not take advantage of either of these approximations but instead, for every active particle-sink pair, sums the contribution from every particle whose radius of compact support intersects the line of sight (Section 2.3.3). As a result the column densities are calculated highly accurately, but at a high computational cost. Our method does, however, scale particularly well when the shortest timestep bin contains a small number of particles, since there is no overhead. This is a significant advantage when supernovae (SNe) are switched on, since the minimum timestep is reduced heavily by the injected energy. It will also be simple to improve

treatment of multiple sources, avoiding the iterative approach, since the number of ionising sources stays constant.

Parallelisation for computer infrastructures that do not share memory (in this case MPI), inevitably puts constraints on the methods used to solve problems or vice versa. The fundamental issue in this case is calculating column densities of gas along lines of sight that cross large fractions of the simulated region. Photoionisation is a long range effect in a code otherwise designed to deal with short range interactions (with the exception of self-gravity). This leads to issues with increasing message sizes between MPI processes and optimisation of calculations.

For MPI every active particle on a given process must be passed to every other process once per timestep. At this point the column density contributions are calculated and sent to the active particle's host MPI process. We have ensured that only required contributions are sent, reducing the message size by a factor of ≈ 100. In SPHNG the MPI domains are only updated at the end of each max timestep, which reduces the amount of time spent checking domains. However, it also means that between max timesteps particles from neighbouring domains begin to overlap. This lack of clear boundaries makes the approach used by TREVR unfeasible

Moving forward we plan to use an adaptive maximum line of sight distance which will speed up the code in the case young and low flux sink particles, due to a reducing the number of lines of sight to be calculated. We also plan to group sink particles, at the beginning of each $\Delta t_{\rm max}$, that occupy the same HII region and are within some separation threshold. Hence reducing the number of ionising sources.

2.3.4 Choice of SPH mass resolution

We perform multiple single source tests of the photoionisation algorithm at a variety of resolutions in order to determine a lower limit to mass resolution for these SPH simulations. Three factors determine whether an ionised source produces an adequately resolved HII region: the SPH mass resolution, the ambient density around the sink particle and the ionising flux of the source(s). In summary, in our simulations at 1 $M_\odot$ per SPH particle, 94% of all ionising photons emitted contribute to HII regions that will reach at least 98% of the size they would reach if resolved to convergent precision.

The challenges of implementing a rigorous photoionisation algorithm at resolutions low enough to simulate such a large region are significant. In this section we quantify the limitations and uncertainties that result from our choice of resolution. To do this we run a set of single source test simulations in uniform density with no

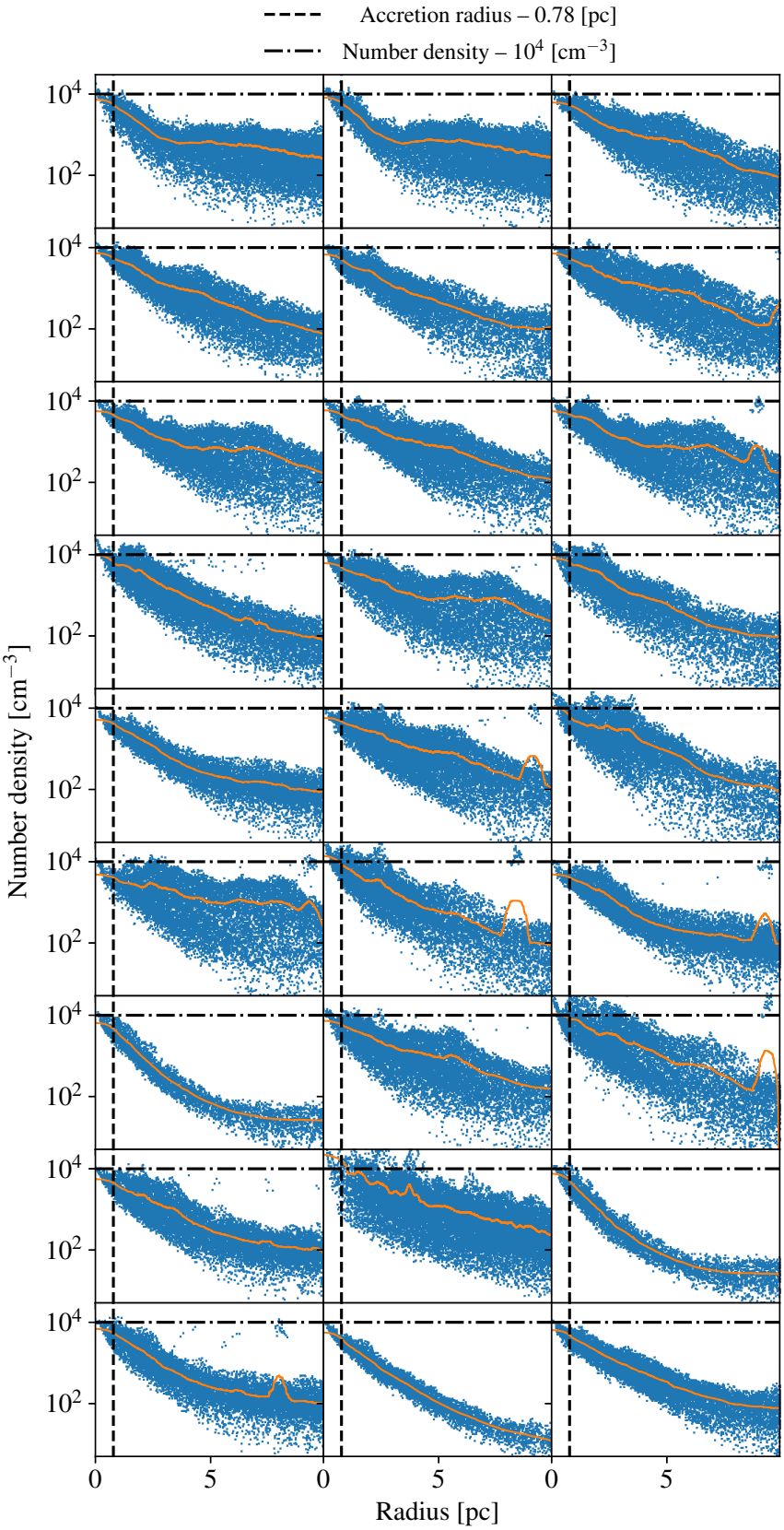

Figure 2.2. Here we show the surroundings of the first 27 cluster sink particles immediately before they form in the SR_ion run. The blue dots each represent an SPH particle and the orange line is a mean of the radial profile. The vertical dashed lines mark the accretion radius (0.78 pc) of the sink particles and the horizontal dot-dash lines are at 10^4 cm^{-3}, which appears to be a characteristic particle number density upper boundary around nearly all of the sink particles at formation.

velocity field at a variety of mass resolutions. We choose an initial number density of 10^4 cm^{-3}, since this is the typical environment in which Strömgren spheres form within our simulations, as shown in Figure 2.2. We use an ambient temperature of 100 K which is slightly higher than our simulations but reduces the computational expense of these tests.

We found the STARBENCH paper (Bisbas et al., 2015) to be very useful in testing the photoionisation method. We use their nomenclature to identify the following analytical solutions to the D-type expansion phase, they are each dependent on the Strömgren radius ($R_{\rm S}$ Equation 2.48):

- Raga-I – Raga, Cantó & Rodríguez (2012b) consider a 'thin' shock to be in pressure balance with the ionised gas inside the IF and derive the IF radius over time by considering the relative velocities of the shock and the material outside,
$$\frac{1}{c_{\rm i}}\frac{{\rm d}R_{\rm RI}(t)}{{\rm d}t} = \left(\frac{R_{\rm S}}{R_{\rm RI}(t)}\right)^{3/4} - \frac{c_{\rm o}^2}{c_{\rm i}^2}\left(\frac{R_{\rm S}}{R_{\rm RI}(t)}\right)^{-3/4}, \tag{2.53}$$
where $c_{\rm i}$ and $c_{\rm o}$ are the sound speeds inside and outside the IF and t is time. It is important to note that fully ionised gas has half the mean molecular weight compared to completely neutral gas.
- Spitzer – The Spitzer solution (Spitzer, 1978, p. 333) can be reached by ignoring the right hand term in Equation 2.53 which is small at early times,
$$R_{\rm Sp} = R_{\rm S}\left(1 + \frac{7}{4}\frac{c_{\rm i}t}{R_{\rm S}}\right)^{4/7}. \tag{2.54}$$
- Raga-II – Raga, Cantó & Rodríguez (2012a) add the momentum of the expanding shell to their model from Raga et al. (2012b),
$$\ddot{R}_{\rm RII} + \left(\frac{3}{R_{\rm RII}}\right)\dot{R}_{\rm RII}^2 = \frac{3R_{\rm S}^{3/2}c_{\rm i}^2}{R_{\rm RII}^{5/2}} - \frac{3c_{\rm o}^2}{R_{\rm RII}}. \tag{2.55}$$
- Hosokawa-Inutsuka – Hosokawa & Inutsuka (2006) derive the radius from the equation of motion of the shock, but do not consider the pressure outside the IF,
$$R_{\rm HI} = R_{\rm S}\left(1 + \frac{7}{4}\sqrt{\frac{4}{3}}\frac{c_{\rm i}t}{R_{\rm S}}\right)^{4/7}. \tag{2.56}$$
- Bisbas et al. (2015) present a semi-empirical equation of their own referred to as the STARBENCH equation intended as a tool for benchmarking, for further detail we recommend referring to their paper.

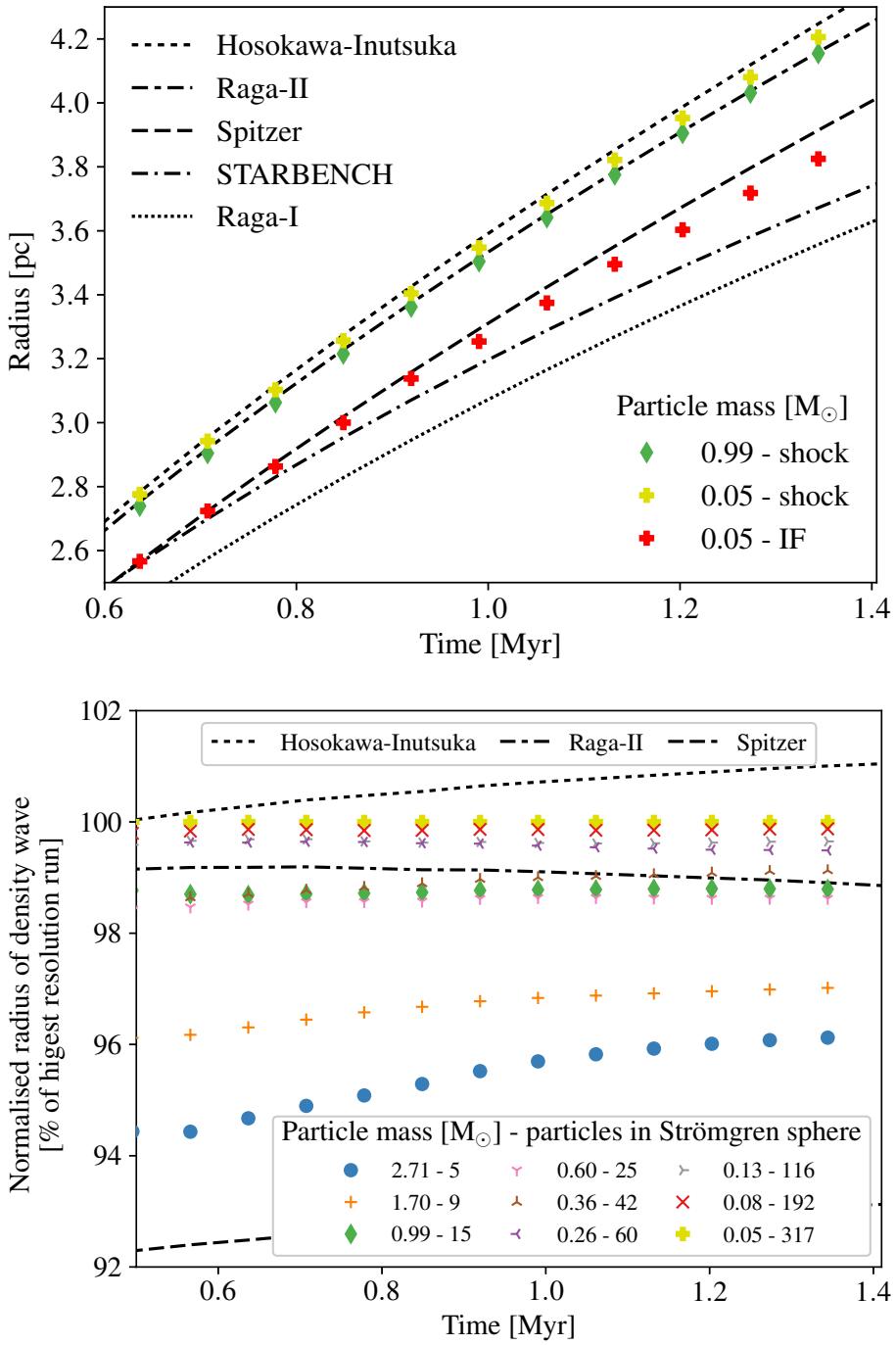

Figure 2.3. The top panel shows the D-type expansion of an HII region around a source of Lyman flux $5 \times 10^{49} s^{-1}$ for simulations at two resolutions. The diamonds (dark green) at a resolution of $\approx 1 M_{\odot}$ per sph particle and the crosses (light green) at the highest resolution test run (20 times more particles) a number of analytical solutions are also plotted. We also plot the location of the ionisation front approximated using the ionised fractions of gas particles for the highest resolution run (red crosses). The lower panel shows the same shock data normalised using the 0.05 $M_{\odot}$ run, including 7 additional resolutions. Each run is defined by its mass per particle and the number of SPH particles that make up the initial Strömgren sphere after the R-type expansion phase. The initial uniform number density in all these simulations is 10^4 cm^{-3}.

The location of the ionisation front is difficult to accurately identify using the ionisation fraction of each SPH particle, particularly when the resolution is poor. Instead we approximate the radius of the resulting shock using a weighted average of the radii of all the particles (N) above the ambient density (ρ_0),

$$R_{\rm shock} = \frac{1}{\rm N}\sum_{i=1}^{\rm N}(\rho_i - \rho_0)r_i, \tag{2.57}$$

where ρ_i and r_i are the density and radius of each particle in the shock above ρ_0 respectively. We plot these radii for a number of resolutions over time in Figure 2.3 for a uniform gas distribution at 10^4 cm^{-3} irradiated by a sink particle with a Lyman flux of 5×10^{49} s^{-1}. In the bottom panel of Figure 2.3 we show the convergence with increasing resolution of the shock radius, the green triangles correspond to the particle mass used in the SR simulations. In the top panel we also plot the five previously discussed analytical radii for the ionisation front and shock radius. This test evolves well past the STARBENCH early phase test but ends before stagnation, the point at which an HII region regains pressure balance with its surroundings. This can be seen since Raga-1 does not become flat in Figure 2.3 (top panel). We note that our highest resolution run is larger than Raga-II, since they consider the shock to have no thickness, and smaller than Hosokawa-Inutsuka, since they do not consider external pressure.

The accuracy of the numerical approximation to the shock radius is dependent on both the SPH particle mass and the Lyman flux of the source, because of this it is useful to define the resolution relative to both of these quantities. We do this by calculating the number of SPH particles that are equivalent to the gas mass in the Strömgren sphere after the R-type expansion phase. We notice that the accuracy of the shock radius reaches 99% consistently around the point at which the initial Strömgren sphere contains $\approx$ 50 SPH particles. This is not surprising since the nominal resolution in SPH using a cubic spline is 50 particles. In Figure 2.4 we show the gas densities at which a given Lyman flux will form a Strömgren sphere containing mass equal to that of 50 SPH particles for a range of particle masses.

The Lyman fluxes of sink particles in the SR_ion simulation vary from 5×10^{47} s^{-1} to 1.3×10^{51} s^{-1}. 90% of sink particles have a flux above 10^{49} s^{-1}, for which the shock wave radii around ionising sink particles in the SR_ion run with photoionisation are approximated to an accuracy above 95%. These estimates are conservative since the 10^4 cm^{-3} is an upper limit on the typical initial sink surroundings and number densities decrease with radius unlike the test runs. If we consider the total ionising

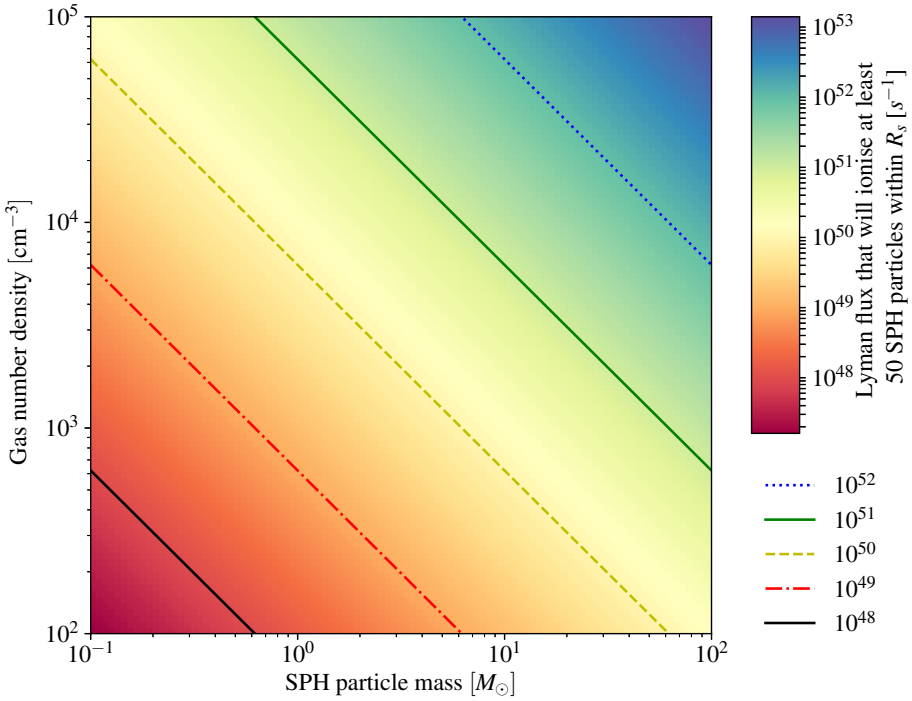

Figure 2.4. A plot indicating the locations at which Strömgren spheres will contain mass equal to 50 SPH particles in gas density – resolution space for a range of Lyman fluxes. The lines are contours for Lyman flux.

flux, rather than the number of sinks, more than 94% of the flux contributes to the formation of HII regions which are at least 98% accurate. A small number of sink particles in the simulations – corresponding to a tiny fraction of the overall flux – are poorly resolved (less than 90% accuracy). However, we note that many large scale Strömgren volume approaches do not resolve individual HII regions at all. If the resolution is too low HII region sizes are underestimated and the density wave is broader and less well defined. This likely leads to lower densities in shells and hence possibly less displaced/triggered SF. These estimates do not consider the cases in which two ionising sinks lie close to one another, in such situations the accuracy would likely be improved.

2.3.5 Supernovae

It is worth noting that the SNe simulated in this work are all considered to be the result of the core collapse of a star of mass $> 20 M_\odot$, while less massive stars also undergo SN, they do so over timescales longer than these simulations.

The stages of the expansion of a supernova remnant (SNR) are summarised in Section 1.5, both the free expansion phase and Sedov-Taylor phases are unresolved in these simulations. We therefore implement supernovae directly in the pressure-

driven snowplough phase using the same approach as Dobbs, Burkert & Pringle (2011).

We identify the number of massive stars that have undergone SNe ($N_{\rm SN}$), in each sink particle, over the last $\Delta t_{\rm max}$. An expansion energy of $N_{\rm SN}10^{51}$ erg is assigned to each sink particle. For sinks with non-zero expansion energies, we identify the radius (R_{shock}) which contains the nearest 80 SPH particles. We then approximate the age of the SNR (t), in years, at this shock radius by rearranging the analytical description of the snowplough phase from Ikeuchi et al. (1984),

$$R_{\rm shock} = 1.13 E_{51}^{115/511} n_0^{-135/511} t^{2/7}, \tag{2.58}$$

where E_{51} is the expansion energy in units of 10^{51} erg and n_0 is the number density of the circumstellar medium (CSM), in units of pc^{-3}. The density is calculated as the average over the 80 particles. We then calculate the SNR cavity temperature using

$$T_{\rm cavity} = 2.82 \times 10^8 E_{51}^{134/511} n_0^{-24/511} t^{-4/7}, \tag{2.59}$$

also from Ikeuchi et al. (1984).

Cioffi, Mckee & Bertschinger (1988) derive analytical expressions for the snowplough phase that take into account the radiative cooling of the cavity. They also perform tests comparing analytical solutions to numerical simulations. They find that the pressure-driven snowplough phase begins at

$$t_{\rm PDS} = \frac{3.61 \times 10^4}{e} \frac{E_{51}^{3/14}}{n_0^{4/7}}, \tag{2.60}$$

where e is the base of the natural logarithm and we have left out the metallicity term, which is unity at solar metallicity. The velocity at the start of the snowplough phase, again omitting the metallicity term, is given by

$$V_{\rm PDS} = 413 n_0^{1/7} E_{51}^{1/14} \text{ km s}^{-1}, \tag{2.61}$$

which is derived as the end of the Sedov-Taylor phase. The shock velocity during the pressure-driven snowplough phase decreases as

$$V_{\rm shock} = V_{\rm PDS} \left(\frac{4}{3} \frac{t}{t_{\rm PDS}} - \frac{1}{3} \right)^{-7/10}, \tag{2.62}$$

where t is the SN injection time calculated through rearrangement of Equation 2.58.

Dobbs et al. (2011) find that this numerical approach agrees well with analytic solutions of SNR as long as the timesteps are not too long. Saitoh & Makino (2009) point out the dangers of neighbouring particles being on very different individual timesteps when dealing with explosive problems. We therefore implement a timestep limiter to ensure timesteps are small enough for gas affected by SNe.

2.4 Increasing particle resolution

Here we describe our method for increasing the resolution in smoothed particle hydrodynamics (SPH) for the purposes of re-simulation (as opposed to modifying resolution locally during a simulation). All the methods which we discuss here, along with our own, involve distributing N-1 new daughter particles around each original parent particle and reducing the mass of all particles by a factor N; daughter particles inherit all other quantities from their parent. The methods vary in the number and locations of daughter particles.

Dobbs (2015) overlay a body centred cubic lattice with the original particles in the centre. The cubes are of side length $1.2h$, where h is smoothing length of the original particle, which leads to the daughter particles sitting $0.6\sqrt{2}h$ from the original particle which is just under half way across the region of compact support. This process is repeated a second time giving a final resolution increase factor of 81.

Kitsionas & Whitworth (2002) use a similar approach, but for increasing resolution on the fly locally; they use a hexagonal close-packed grid consisting of 12 daughter particles. They place these particles $1.5N^{-1/3}h$ from the parent particle which places these particles slightly closer to the parent than in Dobbs (2015).

Both these methods leave a clear visual imprint on the initial conditions, however, after a short relaxation time the density profile is smoothed. They have the distinct advantage that they are incredibly simple to implement, however, they are not so well suited for large increases in resolution (we use $N = 311$ and 823). For large N they require multiple iterations and provide a limited set of possible values for N.

Rey-Raposo, Dobbs & Duarte-Cabral (2014) distribute N-1 particles within $2h$ of each original particle. The daughter particles are placed through an inverse sampling method. They approximate the truncated SPH kernel to a Gaussian since its inverse function is simpler to work with. This means that the radial positions of their added particles follow the SPH smoothing kernel's density distribution. This has the advantage of working for any value of N. While their sampling method avoids large clumps of particles there is still a stochastic element to the locations of the

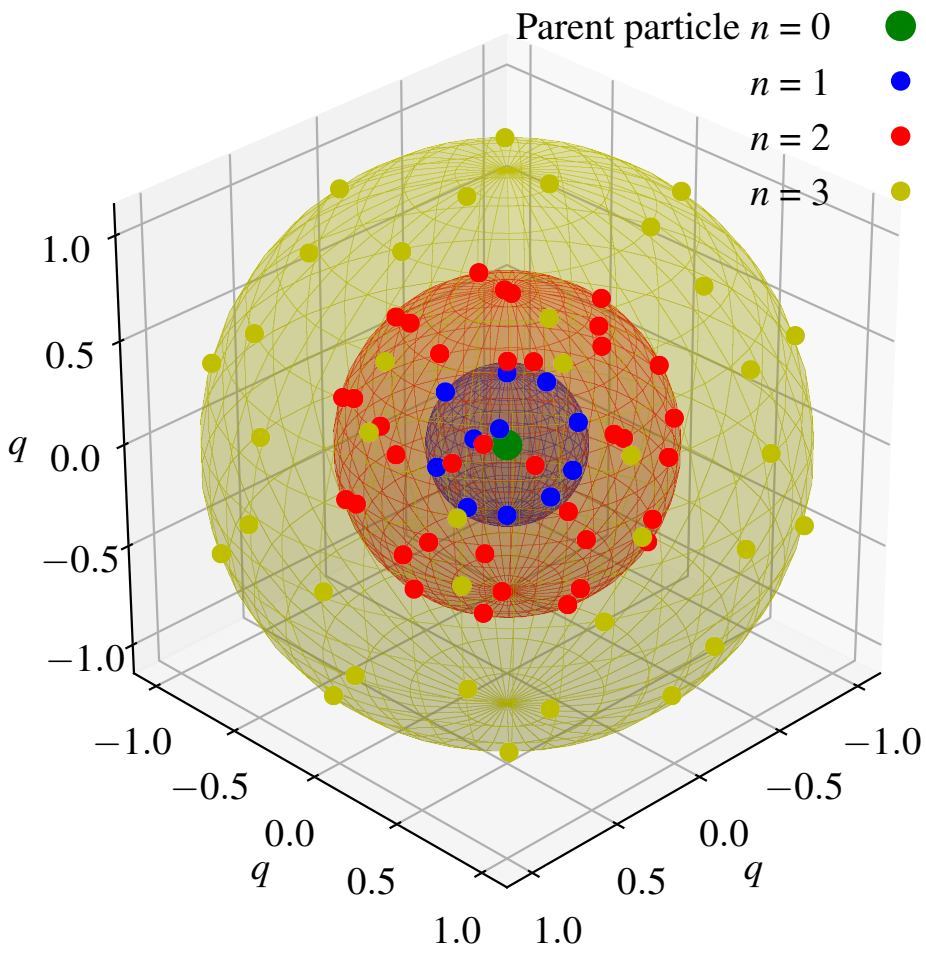

Figure 2.5. A 3-D visualisation of the concentric shell structure of the resolution increase grid. For this plot we have chosen $N = 85$, rather than the 311 used in most of our simulations, for clarity. The shells n = 1-3 hold 11, 37 and 36 particles respectively and are situated at radii of $0.35q$,$0.73q$ and $1.30q$.

daughter particles which we find exaggerates the extremes in density immediately after the resolution increase, although again this is largely smoothed in a short relaxation time.

Since this work is interested in star formation we are keen to avoid over-densities in the initial conditions since they may lead to too many star forming clumps forming in the early stages of the simulation. We have developed a method that uses a spherical grid that leaves a minimal imprint and almost entirely eliminates over-densities.

We build our grid in q-space, where q is a dimensionless distance linked to physical space by

$$q = \frac{r}{h}, \tag{2.63}$$

where r is the physical distance from the centre of the grid (the site of the original particle). Defining truncated kernel functions in terms of q is common in the SPH community (Monaghan, 1992; Price, 2012). This means that we can use the same grid for all parent values of h. The radius of compact support for the SPH smoothing kernel (in this case the M4 cubic spline) is $2h$ which translates to $2q$ in q-space, this is the maximum allowed size of the grid.

The grid is made up of particles sitting on a set of concentric shells, each assigned a shell number n. The grid requires an axially uniform distribution but a radial dependence that causes the effective density to drop off with the smoothing kernel. An example of one of our grids is plotted in Figure 2.5, in this example $N = 85$. To characterise a grid we need to define two quantities, the radius of each shell, q_n, and the the nearest neighbour separation on each shell, s_n. The site of the original particle is denoted by $n = 0$, therefore q_0 is equal to zero, however, s_0 can have any value greater than 0 and less than $2q$.

The radial drop in effective density is achieved by calculating the nearest neighbour separation, $s(q)$, using the normalised inverse of the kernel function, $w(q)$, as the fractional increase above s_0 with increasing radius

$$s(q) = s_0 \left(\frac{w(q)}{w(0)} \right)^{-\frac{1}{3}}, \tag{2.64}$$

where $w(0)$ is the smoothing kernel evaluated at q_0 – the centre of the grid.

Particle separation is constant on each of the shells in the grid so the s_n values can be easily calculated from Equation 2.64. However, there is some choice in how we determine the separation of neighbouring shells. We define this separation as the mean value of $s(q)$ between those shells,

$$q_n - q_{n-1} = \frac{1}{q_n - q_{n-1}} \int_{q_{n-1}}^{q_n} s(q) \mathrm{d}q. \tag{2.65}$$

Since q_0 is zero, we can solve the above equation to find the other values of q_n in turn, until a value greater than 2 is reached; we discard this last result. Since the analytic solution is non-trivial we solve the following by iteration,

$$q_{n_{\mathrm{new}}} = \left[\frac{1}{q_n - q_{n-1}} \int_{q_{n-1}}^{q_n} s(q) \mathrm{d}q \right] + q_{n-1}, \tag{2.66}$$

starting with $q_n = q_{n-1} + s_{n-1}$, and subsequently substituting $q_{n_{\mathrm{new}}}$ for q_n, for each of 30 iterations. Figure 2.6 shows $w(q)$ and its normalised cubic inverse (Equa-

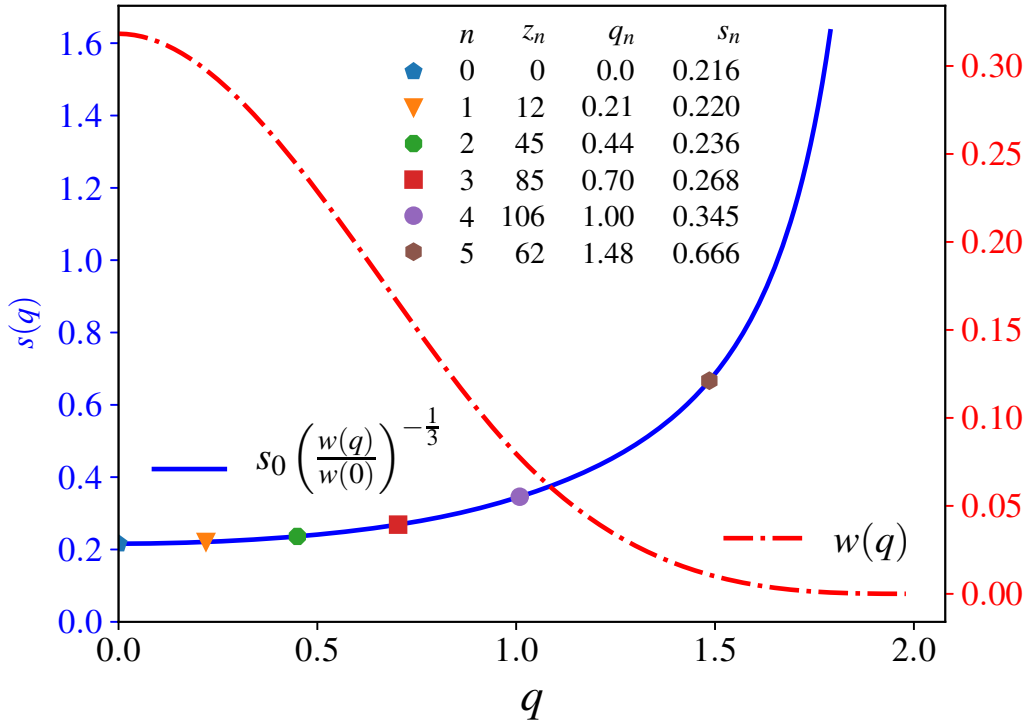

Figure 2.6. The M4 cubic spline (red dot-dash line and right hand axis) and its normalised inverse cubic (blue solid line and left hand axis). The right hand axis values are arbitrary since the value of the kernel is dependent on the smoothing length. The normalised curve is multiplied by the characteristic nearest neighbour separation (s_0) at the centre of the grid so that the left axis gives the separation at any given radius (s_q). In this example s_0 is $0.216q$, this gives $N = 311$. The legend table lists the following shell properties: shell number (n), number of particles (z_n), radius (q_n), and the nearest neighbour separation (s_n).

tion 2.64). The shell locations q_n are marked for $s_0 = 0.216q$ which gives $N = 311$.

The shells are populated by z_n particles whilst ensuring that every particle is as far as possible from its nearest neighbours. We approximate the desirable nearest neighbour separation for a number of particles on a shell as

$$2q_n sin\sqrt{\frac{\pi}{z_n}}, \tag{2.67}$$

choosing z_n to achieve the best match between s_n and this value. This means that the choice of s_0 defines the number of particles in a grid. We solve iteratively for many s_0 values to create grids for new values of N.

There are many ways of distributing particles evenly over the surface of a sphere. Raskin & Owen (2016) place particles on the vertices of platonic solids in an approach for building spherically symmetric initial conditions for SPH that follow a radial density dependence. This has the advantage of offering complete symmetry with

every particle's situation on the shell being identical. However, this platonic solid approach does not allow for any number of particles to be placed on a shell. It is also possible to use spiral methods, such as a spherical Fibonacci point set, to place any number of particles on a shell. These spiral approaches lead to slight variations in each particle's relative environment on the shell. This variance depends on both N and the specific spiral method. We use an 'electron repulsion' approach in which we allow the particles on the shell to repel each other until they approach an energetic minimum.

We avoid any imprinting of the grid on the new initial conditions by generating 72 grids and cycling through them for each particle. Randomly rotating the grid in spherical polar coordinates for each parent particle would achieve the same end. We make an estimate of the new smoothing lengths for each daughter particle and, finally, re-calculate the values of h by interpolation.

It is important to note that any method that has a random element to the placement of new particles will not conserve momentum between the extracted particles and the created initial conditions. This is true of this method and that of Rey-Raposo et al. (2014). The approaches used by Kitsionas & Whitworth (2002) and Dobbs (2015) involve completely symmetric grids and hence conserve momentum (although the instantaneous displacement of the daughter particles inside a galactic potential causes a similar issue). We point out that momentum is conserved throughout the simulations. As with these other methods, all quantities other than density and mass are inherited directly from the parent particle. It would be possible to set these other quantities by interpolating values using the original particle distribution. We plan to implement this in the future.

Seifried et al. (2017) highlight the differences that occur when they increase resolution before or after molecular clouds form. This makes it likely that in this work we miss out on some of the small scale properties of the clouds present in the initial conditions.This is not straight forward to improve upon, since the timescales over which clouds form in the progenitor simulations are prohibitively long. Also H_2 can begin to form very early in the process of cloud formation (Dobbs, Pringle & Burkert, 2012).

Chapter 3

Star formation: simulations of galaxy sections with photoionisation I

We now present simulations of 500 pc^2 spiral arm sections with photoionising feedback. In this chapter we concentrate on the star formation in these simulations. In Chapter 4 we focus on the same set of simulations but consider the effects of feedback on the interstellar medium (ISM) and giant molecular clouds (GMCs).

3.1 Introduction to simulations

The results presented in this chapter and Chapter 4 are based on the same set of simulations. They all use one of three sets of initial conditions extracted as described in Section 3.1.1: a region with a spiral arm passing through its centre (SR), the same region at a higher resolution (HR), and a larger inter-arm region (IA). These are summarised in Table 3.1. The SR and IA initial conditions use N = 311 and the HR initial conditions use N = 823 when increasing resolution as described in Section 2.4. The mass of each SPH particle in these simulations is then 1.00 $M_\odot$ and 0.37 $M_\odot$

Table 3.1. Summary of initial conditions details.

IC reference	Mass ($M_\odot$)	x-y plane size (kpc)	Particle Mass ($M_\odot$)	Number of Particles
SR	4×10^6	0.5 × 0.5	1.00	4×10^6
HR	4×10^6	0.5 × 0.5	0.37	10×10^6
IA	5×10^6	1.0 × 1.0	1.00	5×10^6

respectively. An example of the extraction of the SR region is shown in Figure 3.1.

3.1.1 Extraction from galaxy scale simulation

The initial conditions of the simulations are one of the central facets of this work. Careful preparation of these initial conditions provides a region of neighbouring GMCs in which to study the effects of feedback between them.

We extract square regions from galaxy scale simulations by Dobbs & Pringle (2013). The simulations of Dobbs & Pringle (2013) followed molecular cloud evolution in a spiral galaxy, by modelling a gaseous disc with a galactic potential. The simulations include ISM heating and cooling, self gravity and stellar feedback modelled as supernovae (SNe) feedback. We extract initial conditions after 240 Myr have elapsed, at this point the simulations have reached a rough equilibrium in terms of molecular cloud properties, and the amounts of gas in different phases (Dobbs et al., 2011). The extracted particles are split following the prescription described in Section 2.4 and the galactic potential along with all the physics used by Dobbs et al. (2011) is maintained for all the presented simulations.

We use regions of 0.5-1 kpc in size at full depth through the x-y plane, which is the maximum size for which we are able to resolve the ionisation, given the particle numbers and according to our resolution tests (Section 2.3.4). Whilst Dobbs (2015) trace SPH particles back in time to select their initial conditions, we do not do this here since we only run these simulations for relatively short timescales and the shape of the region does not change substantially.

3.1.2 Summary of simulations

We perform a fiducial run both with no feedback and with photoionistion named SR and SR_ion respectively. These are centred on a section of spiral arm of size 0.5 kpc $\times$ 0.5 kpc at a galactic radius of 2 kpc. We compare these to a variety of other simulations each with one key modification to simulation parameters or initial conditions. Each simulation is summarised in Table 3.2.

We perform three main comparison runs to the fiducial runs using identical initial conditions. We typically assume that all mass that ends up in sink particles forms stars, however, in the SR_50% run, we only allow half of this gas to form stars. This should lead to half as much stellar mass and, therefore, half as much ionising radiation, although this is dependent on the sample distribution. We use this run to identify the relative effects of varying levels of photoionisation.

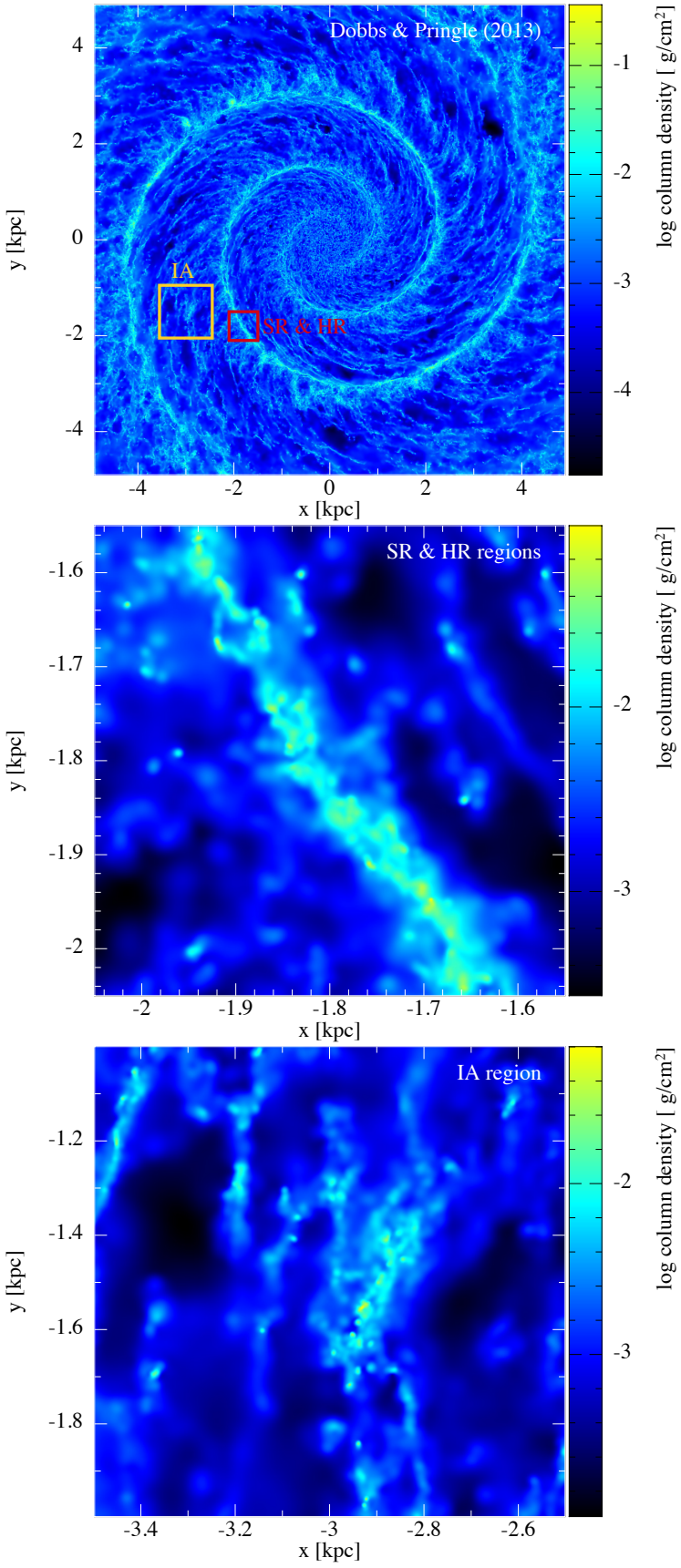

Figure 3.1. The top panel shows a galaxy simulation from Dobbs & Pringle (2013) that has evolved for 240 Myr. The smaller red box is the spiral arm region enlarged in the middle panel and the larger yellow box is the interarm region enlarged in the bottom panel. The resolution of these boxes is increased as described in Section 2.4.

As discussed in Section 2.3.3 we cap all lines of sight at 100 pc, therefore ignoring long range ionisation, which reduces the computational expense by a factor of a few to ten, depending on the size of a simulation and the number of ionising sinks. Emerick, Bryan & Low (2018) suggest that such long range ionisation can be vital to drive outflows in dwarf galaxies. We therefore perform a run, SR_los, with no distance cap to assess the importance of long range ionisation in this work. In the IA_ion run we use a limit of 500 pc to reflect the much larger distances between star formation locations in an inter-arm region.

We also use an alternative sample of stars in SR_alt, which has a different order of massive star creation. The massive star injection interval (Section 2.3.2) is ΔM_i = 305 $M_\odot$ for all simulations except this SR_alt run that uses an alternative sample of stars, of the same total mass, for which ΔM_i = 301 $M_\odot$.

Table 3.2. Summary of the details of the simulations. Column 3 gives the accretion radius of the sink particles.

Run	Feedback	Radius (pc)	Feature varied
SR	none	0.78	Fiducial runs
SR_ion	ionising	0.78	
SR_50%	ionising	0.78	Star formation efficiency 50%
SR_los	ionising	0.78	No distance limit for photons
SR_alt	ionising	0.78	Alternative massive star sampling
HR	none	0.78	High resolution
HR_ion	ionising		
IA	none	0.78	inter-arm region
IA_ion	ionising	0.78	
SR_2	none	0.45	Medium accretion
SR_2_ion	ionising	0.45	radius

The HR and HR_ion runs use the fiducial initial conditions but with three times the mass resolution. These runs are a means to check the work on resolution choice discussed in Section 2.3.4 in anisotropic initial conditions with multiple ionising sources. The IA and IA_ion runs use initial conditions from a separate inter-arm region. Due to lower densities and fewer sink particles forming we are able simulate a larger region of 1.0 kpc × 1.0 kpc (see Figure 3.1). These models investigate how the impact of photoionisation varies inside and outside spiral arms.

We also vary the accretion radius of our sink particles. Different radii vary the scale over which sinks form. Smaller radii will lead to a larger number of smaller

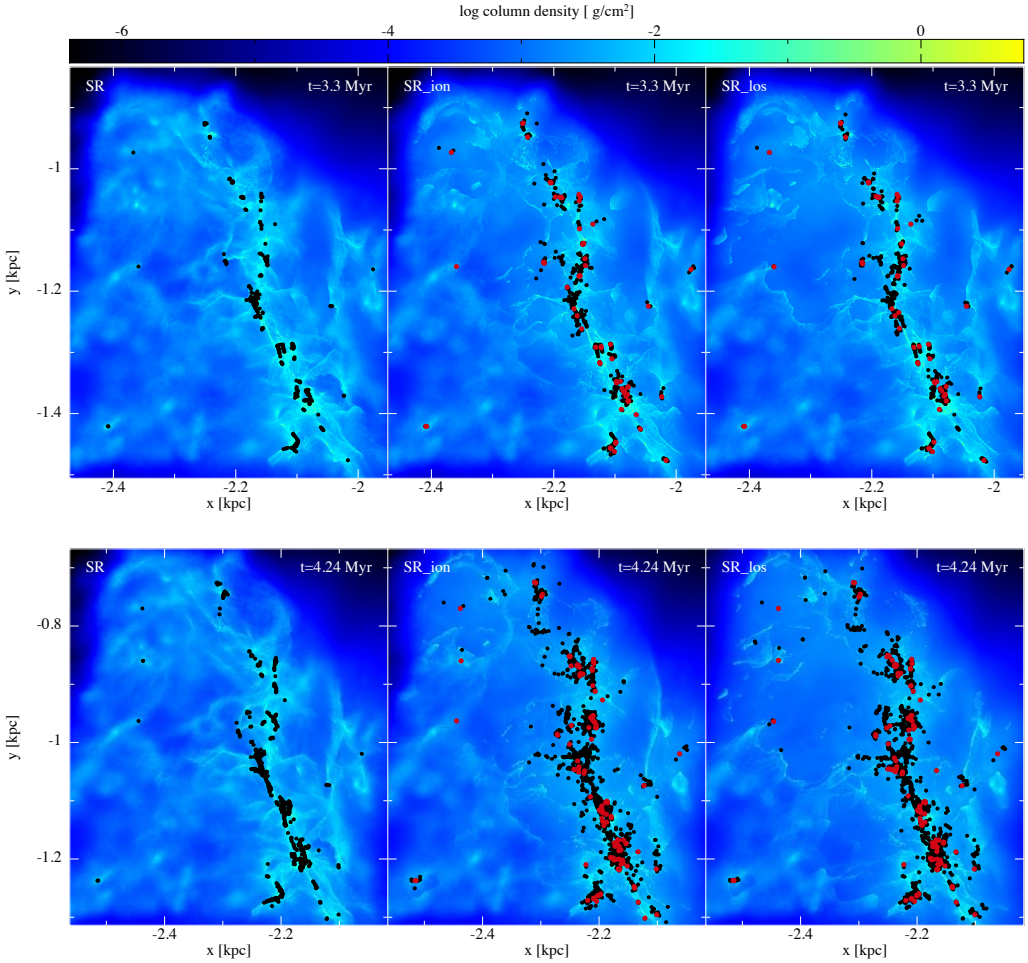

Figure 3.2. The gas surface density is shown for the standard resolution runs at 3.3 Myr (top row) and 4.2 Myr (bottom row), with no feedback (left), ionising feedback limited to a range of 100 pc (middle), and with no distance limit (right). Ionising sinks are distinguished by the larger, red dots. The runs with ionisation show sharper features in the gas, and more sink particles, including sink particles at locations which otherwise do not show star formation without ionisation at the same timeframe. Long range features are more visible in the right hand panel compared to the middle.

sinks. There is a computational benefit to fewer sink particles but it also decreases the resolution on which cluster behaviour can be analysed. Modifying sink parameters can also change the total sink mass in simulations, we aim to get an idea of the scale of these differences. Our standard sink accretion radius is 0.78 pc whilst the SR_2 simulations use 0.45 pc.

3.1.3 Initial non-statistical analysis

In this section we mostly concentrate on comparisons between the SR run with and without ionisation. Figure 3.1 shows the initial conditions for the SR run. For this section of spiral arm, the lower region of the arm is fairly continuous, whereas

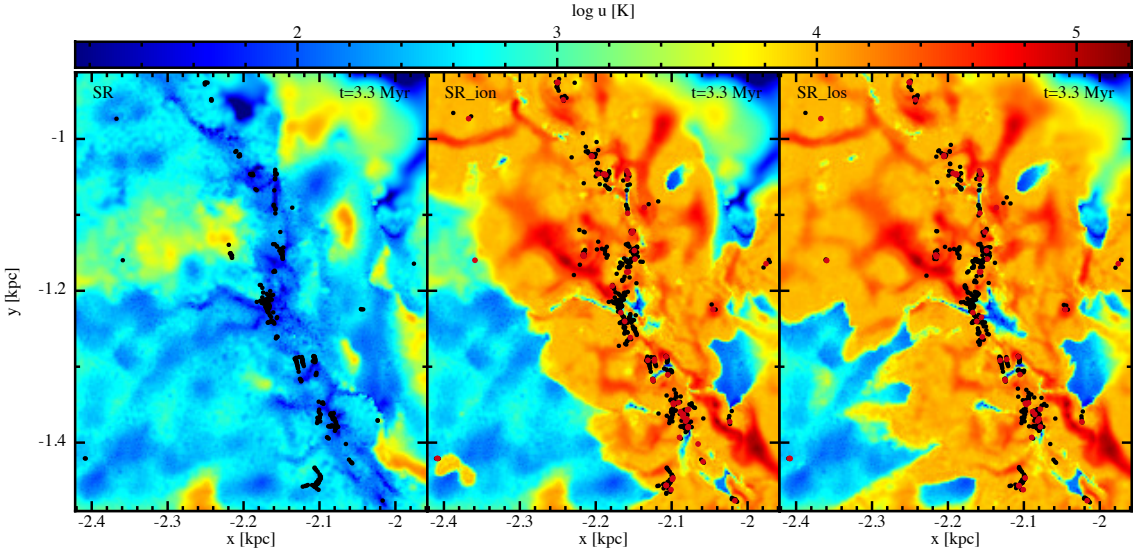

Figure 3.3. We show a cross-section slice at z=0 of temperatures after 3.3 Myr for the same three simulations as Figure 3.2.

the upper part has some emptier regions and shells (caused by SN feedback in the progenitor simulation). In Figure 3.2 we show simulations of this region at times of 3.3 Myr and 4.24 Myr. The figure shows models without photoionisation in the left panel, with photoionisation in the middle and without an ionisation line of sight limit on the right. The larger red dots represent the ionising sink particles and the smaller black dots represent non-ionising sinks. The gas in the upper half of the spiral arm is visibly dispersed while the lower half appears to be relatively untouched.

In the SR_los run very large scale ionised cavities are present, especially in the upper half of the region. The largest galactic HII regions which have both measured radii and distances in the WISE catalog (Anderson et al., 2014) are tens of pc across. Approximately 10% of these regions are larger than 10 pc in diameter and $\approx 1\%$ are larger than 50 pc. The size of our largest simulated HII regions is consistent with the largest WISE objects.

Filaments near to ionising sources are more compact and clearly defined where they have been compressed by the ionised gas. We also see a much larger number of sink particles in the runs with photoionisation. This is due to both triggered sink formation which leads to star formation over a wider region of space, and the reduction of accretion onto ionising sinks which leads to a larger number of lower mass sink particles.

The smaller accretion radius simulations (SR_2) contain a higher number of smaller sink particles, meaning better sink particle resolution. This method leads to lower star formation rates (SFRs) , which are closer to observed rates, however, it

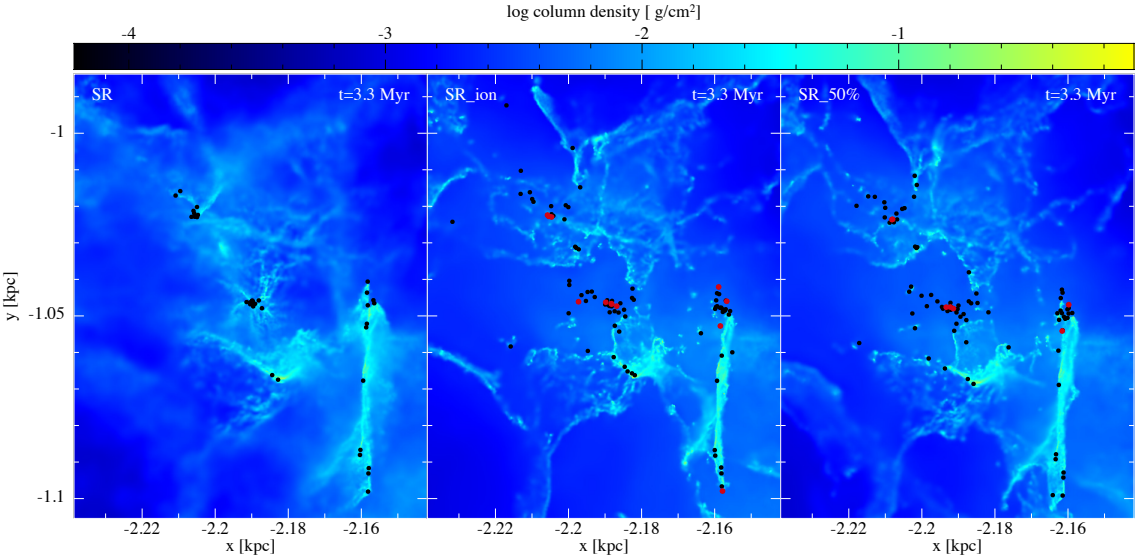

Figure 3.4. A sub-region (≈ 100 pc^2) is displayed where the cluster formation is heavily affected by ionisation. The left and middle panel show the same runs as Figure 3.2, but the right panel now shows the SR_50% run.

also increases computational expense. The lower SFR also means that the SR_2_ion run has a lower ionising flux than the SR_ion run. The alternative sample of massive stars (SR_alt run) also leads to a lower total flux as a result of the stochastic sampling. For the statistical analysis in this work on star formation (rates, efficiencies, and locations) and cloud properties (mass functions, cloud evolution and virial parameters) the differences between simulations are predominantly governed by the total ionising flux emitted. Therefore, for most of our analysis we choose to focus on the SR_50% run, rather than the SR_2_ion and SR_alt runs, since the flux difference between this and the fiducial run is consistent over time and easily quantifiable.

We see the way in which photoionisation modifies the internal energy of the gas in the temperature maps in Figure 3.3. Inside the spiral arm only very localised regions are able to remain cool. The lack of cold gas in the upper half of the SR_ion run emphasises the high impact of photoionisation in this region. The wider extent of heating in the right hand panel (SR_los model) shows the additional impact of long range radiation.

Figure 3.4 shows a small part of a region that is heavily affected by photoionisation. In the no feedback case (left panel) we see groups of sink particles lying along, or at, the intersection of filaments. With ionising feedback, the filaments surrounding the star particles are significantly disrupted, and the remaining dense gas appears to be compressed into sharper features. The morphology of these regions is not too dissimilar to previous single cloud simulations of low mass ($\sim 10^4$ M$_\odot$)

clouds (Dale et al., 2014; Geen et al., 2018).

3.2 Global properties

3.2.1 Star formation rates and efficiencies

In Figure 3.5 we compare the instantaneous star formation rate surface density ($\Sigma_{\rm SFR}$), absolute star formation efficiency (SFE) and the number of sink particles between the SR, SR_ion and SR_50% runs. We calculate the instantaneous $\Sigma_{\rm SFR}$ as

$$\Sigma_{\rm SFR}(t_n) = \frac{M_*(t_n) - M_*(t_{n-1})}{A\ (t_n - t_{n-1})}, \tag{3.1}$$

where t_n is the elapsed time at a given timestep, $M_*(t_n)$ is the total sink mass in the simulation at a given time and A is the surface area of the initial conditions (which we treat as constant in time) for the simulation in the x-y plane. We calculate the absolute SFE as

$$\mathrm{SFE}(t_n) = \frac{M_*(t_n)}{M_*(t_n) + M_{\rm gas}(t_n)}, \tag{3.2}$$

where $M_{\rm gas}$ is the total gas mass in the simulation.

As seen in Figure 3.5, the SFRs in the SR and SR_ion runs are comparable for the first 2.5 Myr, after which time the star formation in the SR run begins to approach a steady state. However, the SR_ion run continues to accelerate until 4 Myr, peaking at double the rate, after which the SFR rapidly drops. There is very little difference in the peak $\Sigma_{\rm SFR}$ between the SR_ion and SR_50% runs, the gradient, however, both before and after the peak, appears to be dependent on the total photoionising flux in the simulation. This trend is also seen in the SR_2_ion and the SR_alt runs.

We discuss the differences for the inter-arm initial conditions (IA) in Section 4.2. We also see this spike in star formation in the SR_2_ion run suggesting it is not a numerical effect resulting from the choice of sink radius.

3.2.2 Accelerated and displaced star formation

Triggering is a much used term that often is given subtly different meaning by authors. From an observers perspective it is typically considered to be star formation that arises as a direct result of feedback, i.e. in a shell around an HII region, or where two such shells collide. From a simulator's perspective it can be interpreted as star formation that occurs in simulations with feedback but not in those with-

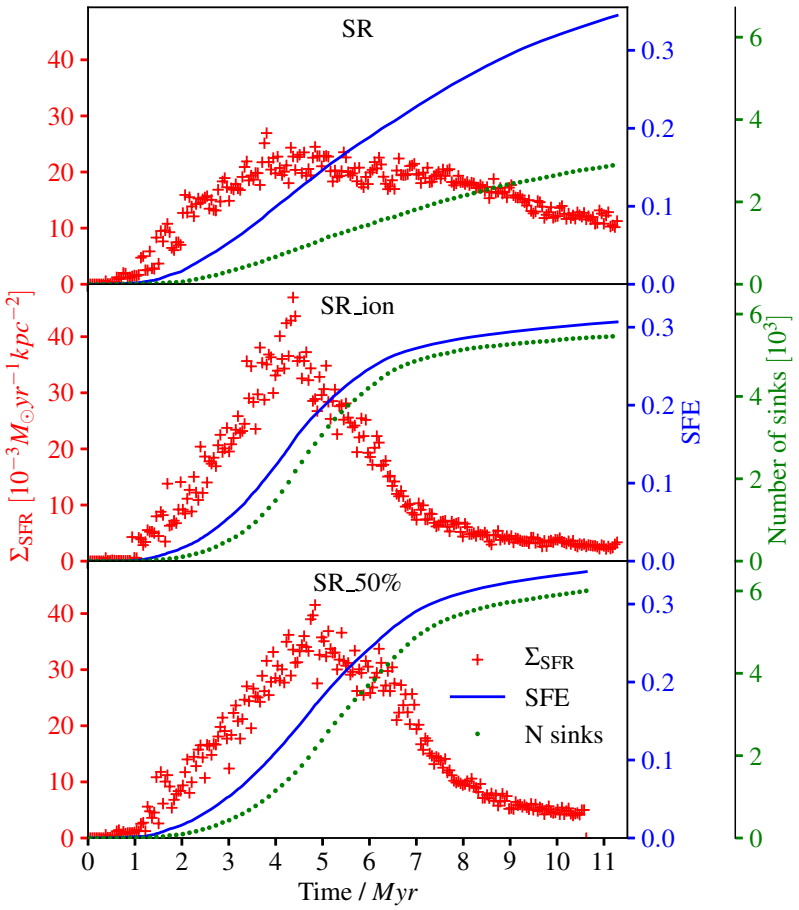

Figure 3.5. The instantaneous SFR surface density is plotted over time without feedback (top), with photoionisation (middle) and in the SR_50% run (bottom) as red crosses. We also plot the absolute star formation efficiency (blue line) and the number of sink particles (green dots).

out, although this is complicated by higher accretion rates in simulations without feedback.

Dale, Haworth & Bressert (2015) point out that while identifying triggered star formation (SF) in simulations is straight forward, doing the same for observations, especially on scales below individual GMCs, is not. They also point out that that the only environments that exist without stellar feedback are in simulations, and hence they question the usefulness of the distinction. For comparison of simulations with and without feedback it remains a useful concept, but also one to approach with caution.

In this work both the increase in SFR and the modified stellar distribution that photoionisation produces suggest a significant amount of triggered star formation in the surrounding interstellar gas. The triggering does not last indefinitely in our simulations, presumably as dense gas on the verge of forming stars has already

produced star formation, and further ionisation does not lead to any more collapse, and thus the star formation rate decreases. Dale, Ercolano & Bonnell (2012) use the terms 'weak triggering' and 'strong triggering' to refer to temporary and permanent changes in the star formation process. They consider changes to the SFR weak triggering and changes in the SFE and number of stars (IMF) strong triggering. We find that photoionisation causes weak triggering that increases the SFR in all our runs, we refer to it as accelerated star formation throughout this thesis. We refer to the strong triggering effect that leads to modified stellar distributions as displaced star formation.

As shown in Figure 3.5, many more, and less massive, sinks form in the SR_ion run. We identify three reasons for this:

1. Photoionisation clears away gas from the sinks shutting down accretion.
2. Groups of sink particles in feedback runs are less bound than with feedback (Section 3.2.6); as a result of this and the relaxed sink particle merger criterion discussed in Section 2.2.12, there are fewer mergers in the feedback case.
3. in the SR_ion run many additional sink particles form around ionisation fronts due to triggered star formation.

In Figure 3.6 we estimate the distances over which this triggered star formation appears to occur in our simulations. For each sink particle in the runs with photoionisation we find the nearest sink at the equivalent timeframe for the no feedback run, and record these minimum separations. In the top panel in Figure 3.6 we plot the fraction of sink particles (by mass) in the SR_ion model which lie above a given distance from any sink particle in the no feedback simulation. We see that in the SR_ion run a significant mass of sink particles is situated more than 5 pc from the location of a sink particle in the SR run. It is important to note that we are not comparing where specific gas particles form sink particles or are accreted in runs with and without feedback, but rather the relative instantaneous locations of sink particles. As a result we do not identify displaced star formation that occurs near other sites of star formation, so this is an underestimate of the degree of triggering by photoionisation. There also may be sink formation at slightly different times in the two runs, which may overestimate the displacement on short timescales, but this should average out over time.

At its peak, between 3 and 5 Myr, the SFR in the SR_ion run is 1.3 times that in the SR run; at this time the fraction of sink mass in the SR_ion run greater than 5 pc from a sink in the SR run, is between 0.2 and 0.3 (as seen in Figure 3.6). We infer from this that the majority of all accelerated star formation is occurring more

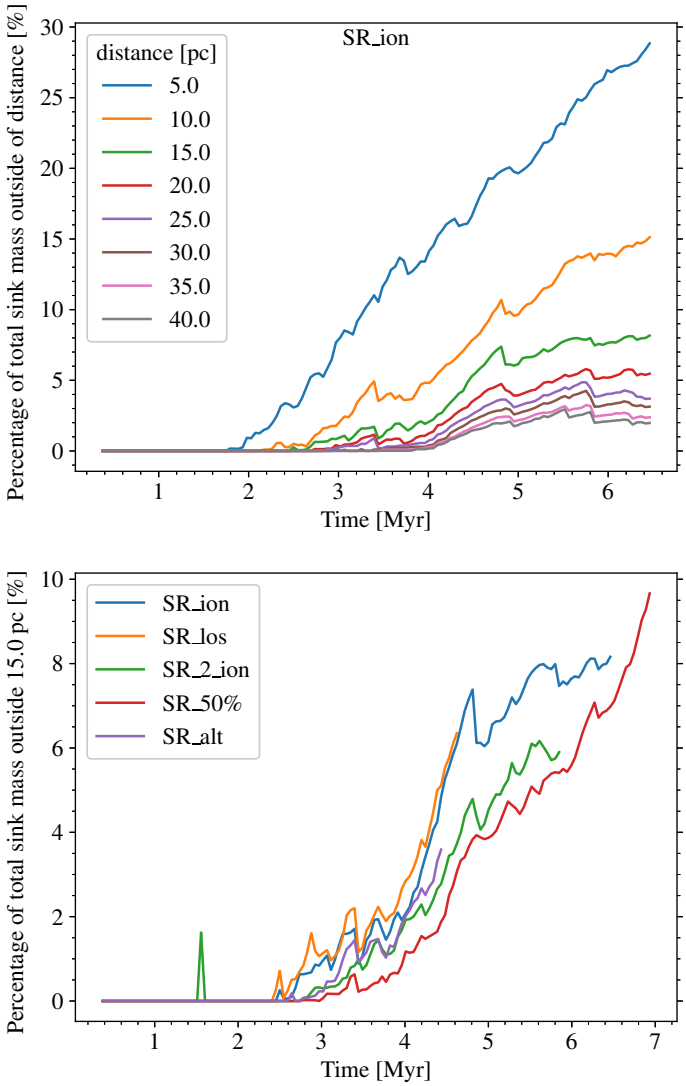

Figure 3.6. Top panel: the percentage of mass in sinks in the SR_ion run that is further than a range of distances from the nearest sink particle in the SR run. Bottom panel: the top panel's 15 pc distance plot now compared to several runs with photoionisation.

than 5 pc from star formation in the no feedback case. In other words, most of the accelerated star formation in these simulations is occurring on scales larger than the majority of single cloud studies.

The bottom panel of Figure 3.6 compares the 15 pc line from the top panel with the equivalent analysis in the other photoionisation runs. We see that the fraction of star formation triggered at distance is dependent on the total photoionising flux. Simulations with more flux produce more stellar mass further away from the equivalent no feedback run. It is worth noting that the SR_los run only has a tiny fraction of stars at larger distances relative to the SR_ion run. Additional triggering induced by long range photons at significant distances from star formation in the SR run

appears to be present but only makes up a tiny fraction of the total star formation.

3.2.3 Molecular cloud compression

The formation of stars in the dense gas surrounding IFs – the collect and collapse model – has been explored analytically by Whitworth et al. (1994) and Hosokawa & Inutsuka (2006). Simulators have looked at fragmentation in the IF for both uniform (Dale, Bonnell & Whitworth, 2007a) and fractal (Walch et al., 2011) initial conditions. Observational evidence for the collect and collapse model is discussed in Section 1.4.2. We make a distinction between collect and collapse triggering and the star formation triggered when ionisation fronts collide with dense gas structures or another ionisation front. There are multiple examples in the simulation of objects similar in appearance to, if much larger than, bright rimmed clouds which are created by radiation-driven implosion (Bertoldi, 1989; Morgan et al., 2008). We see a moderate amount of triggered star formation in such clouds when they are hit by shocks on one side. However, when clouds are compressed by HII regions on multiple sides, we see a much more significant acceleration in star formation.

Some comparable compression effects on clouds, in this case due to stellar winds and SNe, have been noticed by Krause et al. (2018). They present a 'surround and squash' scenario in which they find that SN feedback floods into low density regions created by earlier feedback and compresses the denser regions that the feedback flows around. This 'squashing' effect induces further star formation.

There also many similarities between these simulations and those of Inutsuka et al. (2015). They suggest that low-mass molecular clouds are much more likely to reach the densities required for SF when compressed by shocks. They also suggest that a 'network of expanding shells' can lead to the creation of new GMCs. They note that this only occurs either when the magnetic fields in the shell are close to alignment with the gas it is moving into or when gas is compressed by multiple shocks. They summarise this with the schematic in Section 3.2.3.

The density maps in Figure 3.7 show the last timeframe (3.3 Myr) at which the SFRs are comparable between the SR and SR_ion runs (upper panels) and the time at which the SFR for the SR_ion run peaks (4.24 Myr, lower panels). The ionisation runs on the right are overlaid with contours of the ionised fraction of gas. The SR run does eventually form stars in some of these regions, in one case the onset of star formation is delayed by ≈ 2 Myr and, once started, the process takes an additional ≈ 2 Myr. By comparison, this region is converted into stars in 1 Myr in the SR_ion simulation, meaning that without photoionisation this star formation is delayed by

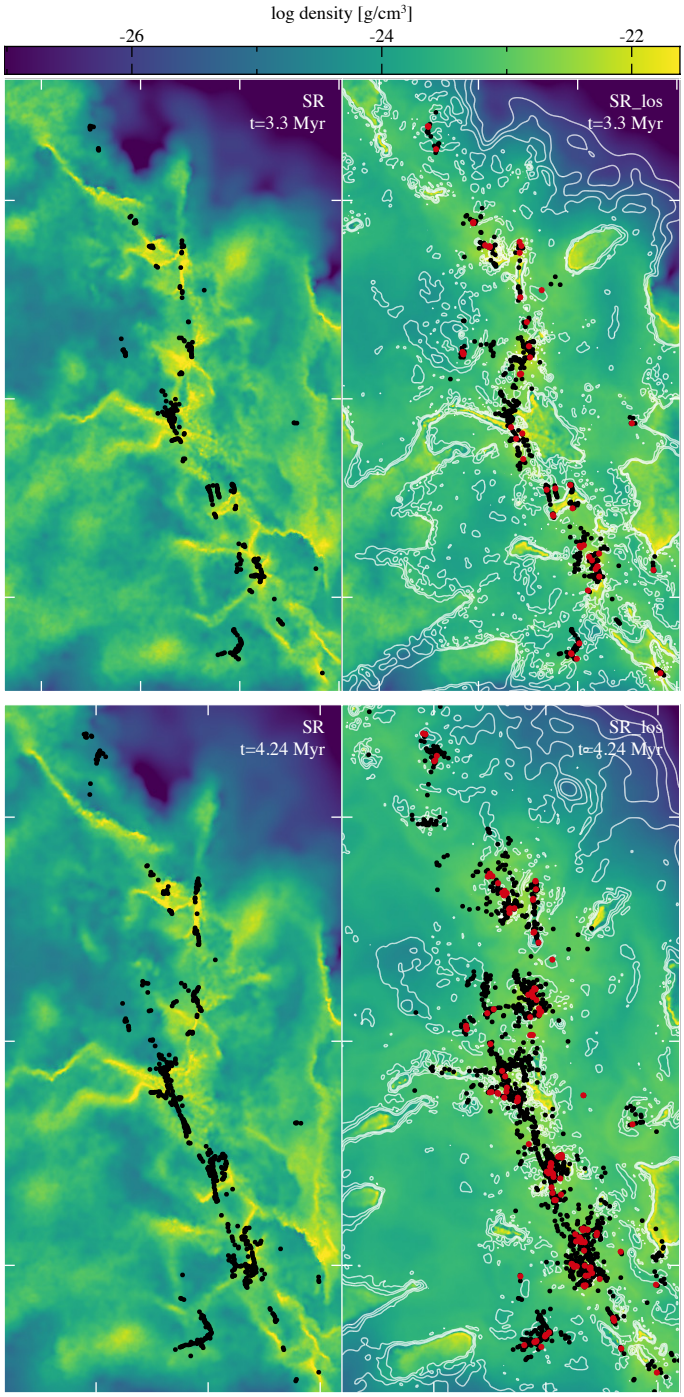

Figure 3.7. Left panels: run with no photoionisation (SR). Right panels: No range limit photoionisation run (SR_los) with ionised gas fraction overlaid in contours. The top and bottom panels are at 3.3 Myr and 4.24 Myr respectively. The contours in the top right panel allow for the identifcation of pockets of dense gas that are resisting ionisation. Comparison with the bottom panels shows that when dense pockets are compressed by HII regions from multiple sides triggerred star formation is very likely to occur within a Myr. Gas that only has an HII region on one side may or may not undergo more modest triggered star formation on this timescale. The cross sections are shown about z=0.

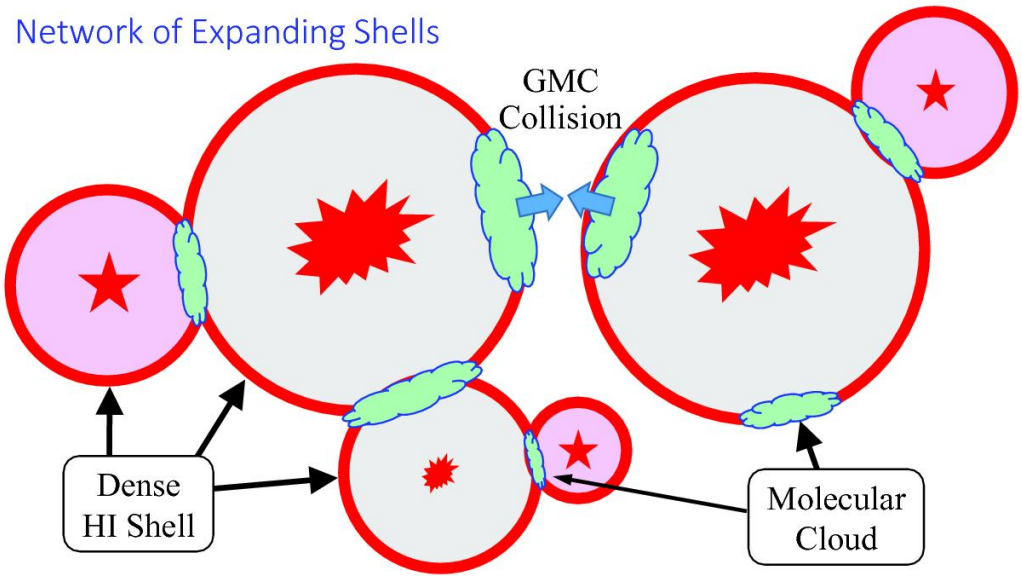

Figure 3.8. Schematic demonstrating the effect of multiple colliding shells. A network of expanding shells can lead to GMC collisions and also GMC formation by compression from multiple sides or from one side if magnetic fields align (Inutsuka et al., 2015).

3 Myr.

3.2.4 Comparison with observations

In Figure 3.9 we compare the star formation rates in our models with observations. We overplot the star formation rate versus surface density at different times for the different models on observations of star formation using the data from Bigiel et al. (2008). In their work, Bigiel et al. (2008) measure surface densities and star formation rates in regions on a 750 pc scale, similar to our simulations. The SFR surface densities ($\Sigma_{\rm SFR}$) change as the total gas surface density decreases over time, an effect more pronounced in the SR_ion run than the SR run. The combination data in Figure 3.9 represents a weighted addition of the SR_ion and IA_ion simulations such that the total gas surface density ($\Sigma_{\rm gas}$) is equal to that for the whole galaxy from which our initial conditions are extracted.

The gas in our simulations is forming stars faster and more efficiently compared to nearby galaxies, as is common in most hydrodynamical simulations of star formation. This is also evident from the high absolute SFEs of over 30%, shown in Figure 3.5. These effects are exaggerated by the assumption that all mass in sink particles is stellar mass, although the SR_50% simulation goes a long way to addressing this issue. Photoionisation only reduces the SFE on timescales longer than lifetimes of the majority of O stars.

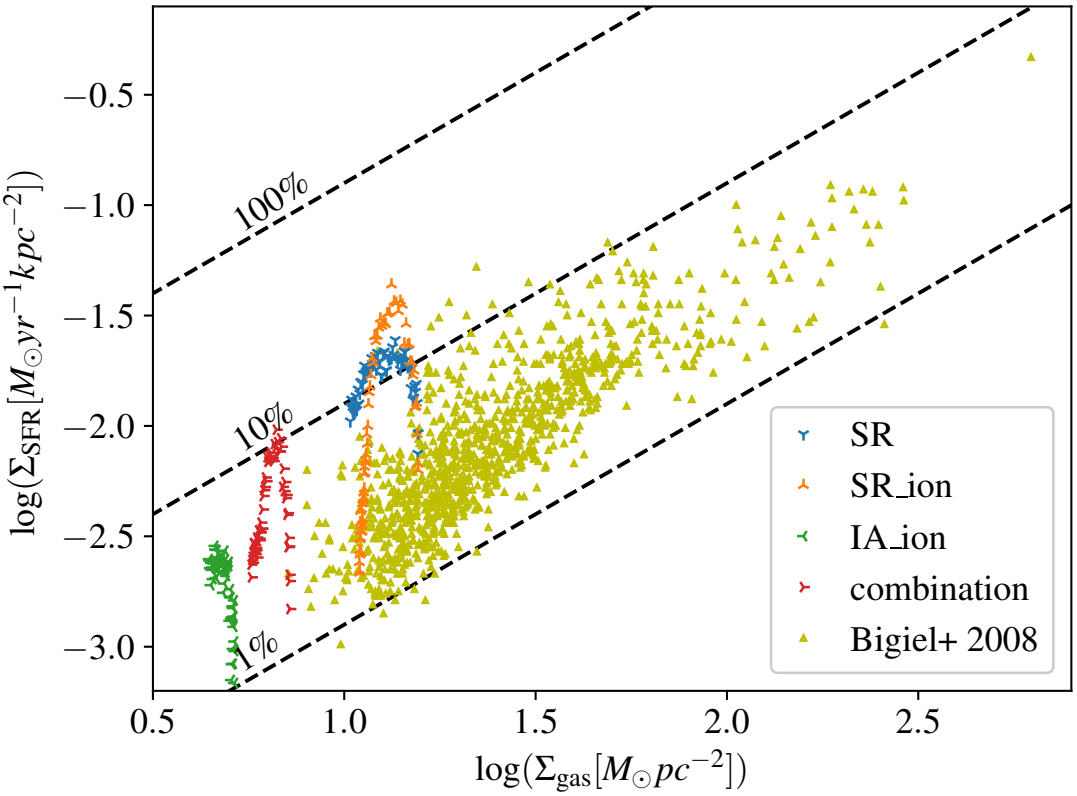

Figure 3.9. The relation between SFR surface density ($\Sigma_{\rm SFR}$) and total gas surface density ($\Sigma_{\rm gas}$) is plotted for our simulations and using observational data from Bigiel et al. (2008). Multiple points plotted for our simulations represent the time evolution of the region. We plot the spiral arm (with and without feedback), an inter-arm region and a weighted combination of the two such that $\Sigma_{\rm gas}$ is equal to the entire galaxy our initial conditions are extracted from. The diagonal dotted lines, also from Bigiel et al. (2008), give the absolute star formation efficiency over a 10^8 year period.

There are a number of reasons why our simulations overestimate the star formation rate. Firstly we only model one form of feedback, whilst so far ignoring SNe, winds and radiation pressure. Around 3-15% of the sink particles contain ionising sources, depending on the elapsed time and run, this accounts for well over 90% of all ionising photons emitted from stars. In reality the non-ionising sinks would emit small amounts of ionising photons along with winds and radiation pressure. If accounted for this is likely to reduce accretion onto the non-ionising sinks significantly. A second, and probably more important, issue is that these simulations begin in the absence of any photoionising feedback. In reality there would be a population of ionising sources at the start of the simulation, which may diminish the extremes we see in the star formation rate.

Furthermore our initial conditions contain no turbulence below the resolution of the galaxy simulations they were extracted from, meaning that the smallest size scale of turbulence in the initial clumps is of order 3-10 pc. Initial turbulence on

these scales could lead to more fragmentation of dense gas structures early on and therefore lower SFRs and/or more sites of star formation. The accretion radius is also a factor in the high SFE, however, the SR_2 and SR_2_ion runs suggest that this is only a small effect.

3.2.5 Cluster sink particle evolution

There is a noticeable difference in the average mass of cluster sink particles in simulations with and without photoionisation. Figure 3.10 shows a selection of sink particles, that form before 3.2 Myr, from the SR and SR_ion runs that highlight this. We identify two main causes of this difference.

1. The ability of photoionisation to reduce pressure around an ionising sink and move gas particles away.
2. The formation of sinks in a larger number of locations, also resulting from photoionisation, which means that all sinks are more likely to share accretion reservoirs.

The continuing accretion onto cluster sink particles particularly in simulations without feedback highlights problems with treating cluster sink particles too much like individual stars. This remains the norm within the field and makes comparisons of SFRs in such simulations less valuable. While sub-grid cluster sink models are becoming increasingly sophisticated in their treatment of feedback (Gatto et al., 2017; Howard, Pudritz, Sills & Harris, 2019, along with this work), ignoring the gas component of cluster sinks leads to over-estimations of the number of massive stars and hence feedback along with ignoring large amounts of dense gas inside clusters.

3.2.6 Stellar clusters

These simulations are not well suited for the study of stellar distributions and dynamics This is largely a result of our sink particles being fairly massive so that clusters are not resolved with a large number of sink particles. We nevertheless provide a short analysis of the effects of photoionisation on stellar clusters in the simulations, to provide some general, insight. We make no attempt to identify clusters based on the origins of the sink particles. Instead we build a minimum spanning tree of all of our sink particles and cut all branches of this tree above some distance. We call this the cut-off distance. Repeating this for a range of cut-off distances allows us to assess multiple sets of clusters defined by different size scales for the same set of sinks. We show in Figure 3.11 cluster properties versus this cut-off dis-

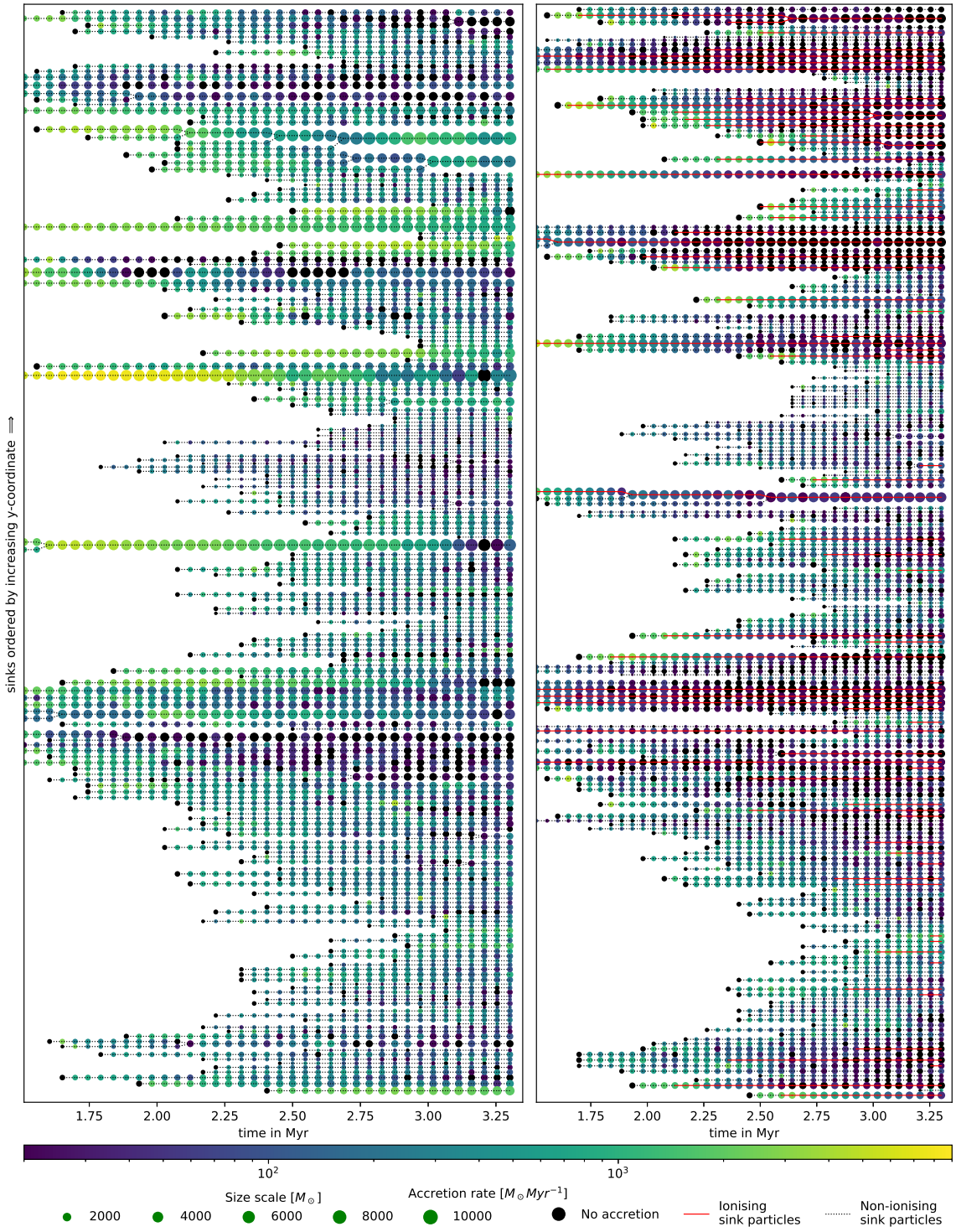

Figure 3.10. Sink evolution over time for a selection of sinks from the SR and SR_ion runs. The size of each circle represents the mass of the sink, their colour represents the rate of accretion. The lines joining points show mergers of sinks and their colour whether they are ionising (red) or non-ionising (black). The average mass of sinks in the SR_ion run is lower and the timespan over which accretion occurs is shorter.

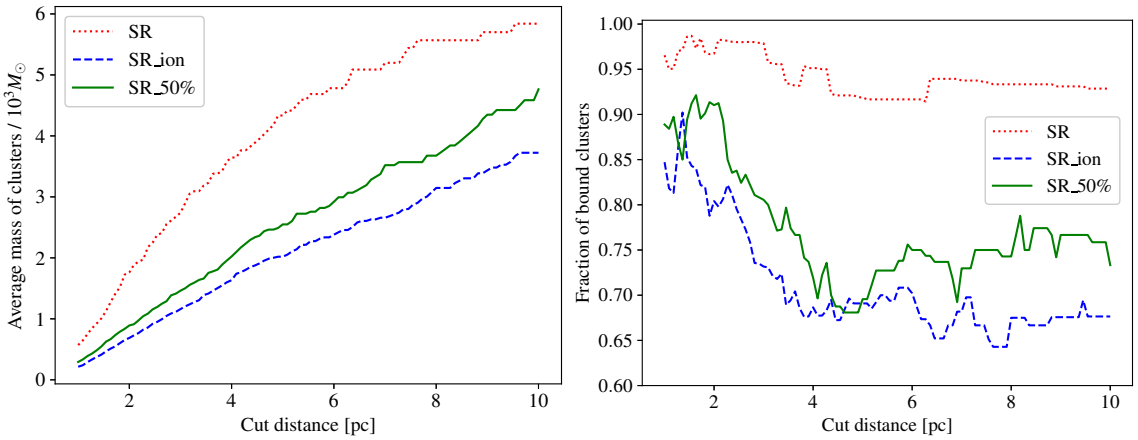

Figure 3.11. The properties of clusters are shown versus the cut-off distance we take for the minimum spanning tree (which sets the extent of the cluster) at a time of 3.3 Myr. We show the average cluster mass in the upper panel and the fraction of clusters that are bound in the lower panel.

tance, which is a proxy for the size scale of the clusters. All of the cluster analysis presented in this section considers only the sink particles and ignores the gas.

In Figure 3.11 (top panel), we show the average mass of the cluster versus the distance criterion. The figure indicates that clusters in the model with no feedback (SR) have higher masses, and therefore densities, than their counterparts in the simulations with ionisation. In the lower panel of Figure 3.11 we show the fraction of bound clusters for the different cut-off distances. As would be expected with short cut-off distances the clusters tend to be bound in all the models, although there are fewer bound clusters with ionisation. As the cut-off distance increases, the fraction of bound clusters stays fairly constant with no feedback, but drops off by around 20% in the models with ionisation. So, similarly to the behaviour for the gas, the ionising feedback appears to lead to fewer bound clusters. And again, the model with 50% ionisation, SR_50%, shows a significant difference to the no feedback case, indicating that smaller amounts of ionising feedback can still have a significant impact.

Observations suggest that 40 to 90 % of stars form in clusters, depending on the criteria for a cluster (Bressert et al., 2010), although Kruijssen (2012) suggest the fraction is less than this, around 30%. The latter estimate would mean that we form too many bound clusters, although we again note that the stellar accretion and mergers are not well resolved or represented in our simulations, and again we may be missing other forms of feedback which may influence cluster evolution. While our bound fractions are unlikely to be accurate, the tendency towards a significantly lower fraction of bound clusters in the presence of photoionisation is very clear.

Chapter 4

The interstellar medium: simulations of galaxy sections with photoionisation II

In this chapter we continue our analysis of the simulations introduced in Chapter 3, but now consider the impact of photoionising feedback on clouds and the wider ISM. We begin by looking at clouds on multiple scales in the spiral arm (Section 4.1), then we compare this to an inter-arm region (Section 4.2), and then we look at the distribution of gas properties throughout the entire ISM (Section 4.3).

4.1 Cloud structure and morphology

In this section we look more quantitatively at the cloud structure of the gas. We apply a friends of friends algorithm to identify clouds and clumps within the simulations. The algorithm groups particles within a certain distance of each other, and identifies them as a coherent structure. We also require that each structure has a minimum number of particles which we set to 100. For the results here, we tested three different minimum distances, 0.24, 0.37 and 0.55 pc which lead to structures with slightly different ranges of masses and densities. Using a distance of 0.55 pc, we group particles into regions which are similar to molecular clouds, with median number densities of 100 cm^{-3}. For a distance of 0.24 pc, the structures picked out tend to be more similar to clumps within a cloud, and have median number densities of around 1000 cm^{-3}.

In Figure 4.1 we show mass functions for the clouds and clumps selected with number densities of 1000 cm^{-3} distance criteria (top), 300 cm^{-3} (middle) and 100

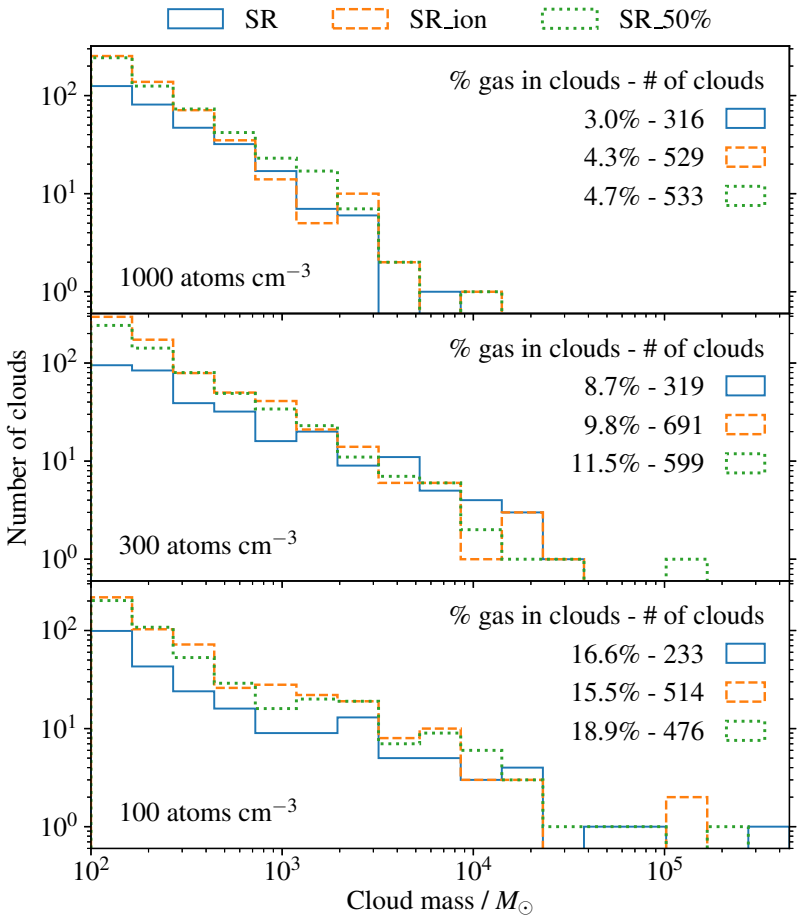

Figure 4.1. Cloud mass functions are shown for three cloud densities for the SR runs (continuous blue), the SR_ion run (dashed orange), and the SR_50% run (dotted green). The clouds are defined using a friends of friends algorithm with a maximum particle separation criteria of 0.24 pc, 0.37 pc and 0.55 pc (top to bottom), and the median number density of clouds for each of these criteria is $\approx$ 100, 300 and 1000 cm^{-3} respectively. This is a snapshot at 4.24 Myr chosen, since this roughly corresponds to the peak in the difference in the number of clouds between the SR and SR_ion runs. We also quote the fraction of all gas in clouds and the number of clouds for each case.

cm^{-3} (bottom) for the simulations with and without ionisation. The mass functions are shown at a time of 4.24 Myr. From Figure 4.1 we see that there are more clouds and clumps in the simulation with photoionisation. Particularly there are more low mass clumps, but there are also a few more high mass clouds. Thus the global effect of photoionisation appears to break up the clouds and clumps into smaller structures, however, in some cases the photoionisation causes the merger of two or more clouds (i.e. the largest cloud in middle panel). We can see this a little in Figures 3.2 and 3.4, where the ionisation tends to make the filaments thinner and denser, and in some cases break up the filaments.

We perform the two-sample K-S test on the cloud distributions for the SR_ion

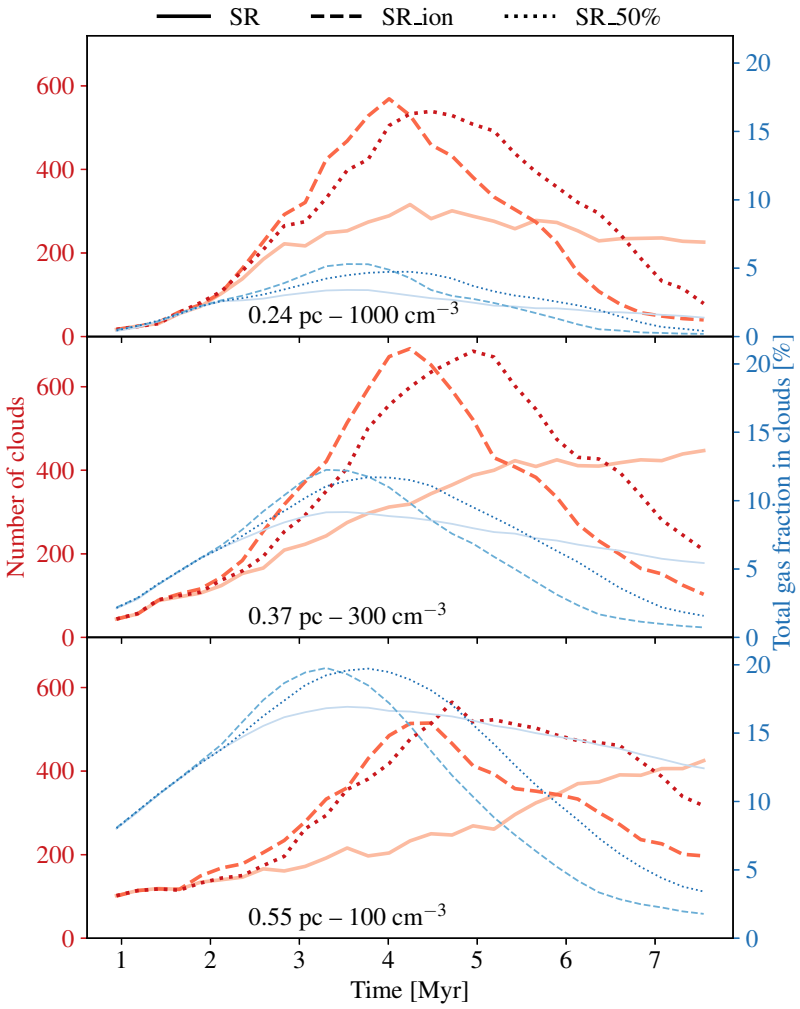

Figure 4.2. The evolution of the number of clouds (thicker red) and the gas fraction contained in them (thinner blue) is shown with time. We present the same runs and use identical criteria to define the clouds as in Figure 4.1.

.

and SR_50% runs, each relative to the SR run but at multiple epochs. We find that at 4.24 Myr (Figure 4.1) the p-values from the K-S test for the SR_ion run are 0.008, 0.00003 and 0.34 for clouds of median number density 1000, 300, and 100 cm^{-3} respectively. This suggests that clouds as defined by our middle criterion, median number density 300 cm^{-3}, are the most disrupted and clouds as defined by a median number density of 100 cm^{-3} are less affected. This trend is supported consistently throughout the time evaluation of the simulations. The objects defined by the densest criterion (clumps) are affected less than those by the middle criterion; this could be due either to dense gas resisting feedback or because these objects are dominated by the process of sink particle formation which does not vary between simulations. The K-S test results for the SR_50% run suggest a similar trend – as

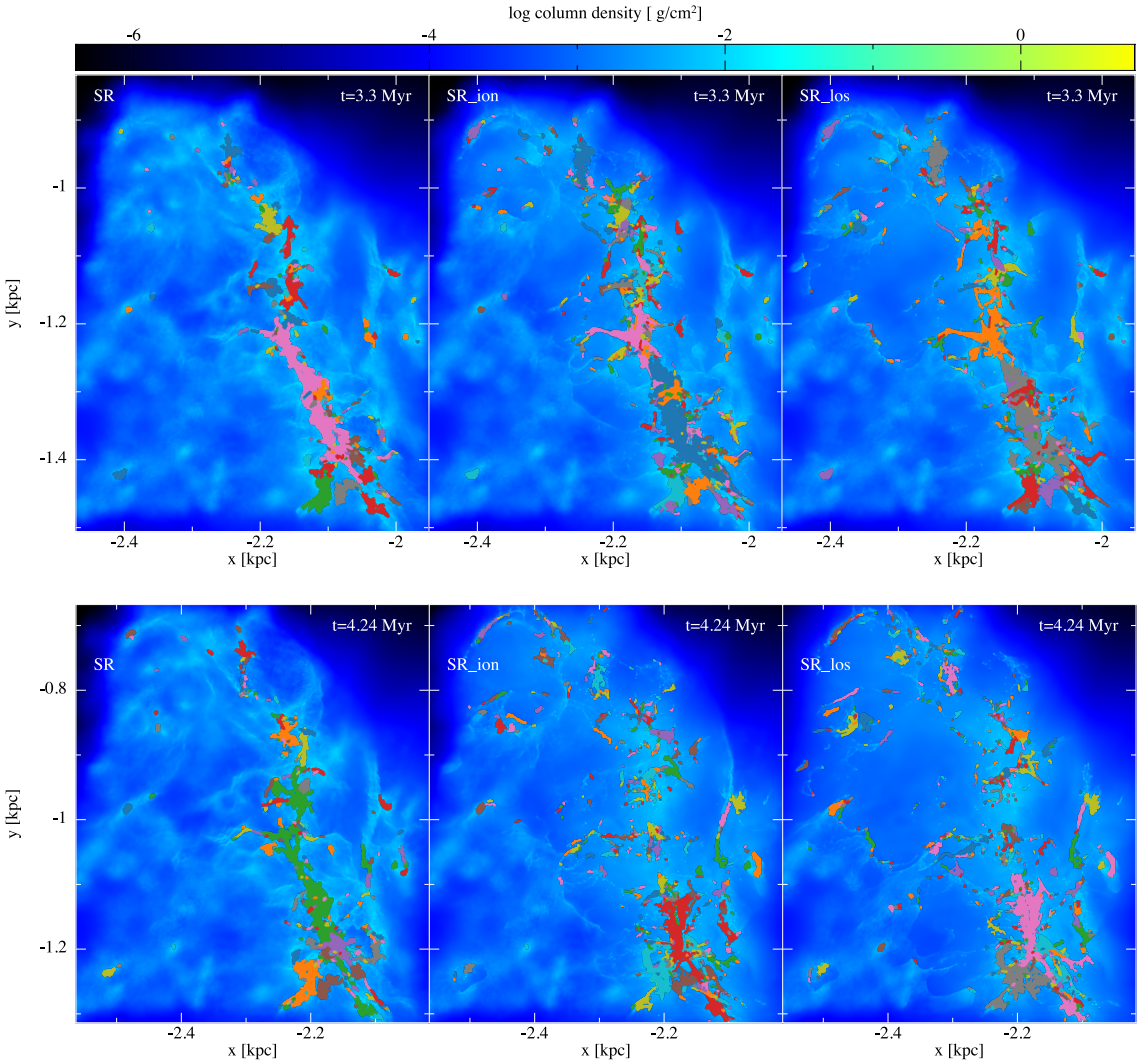

Figure 4.3. As in Figure 3.2, we show the simulations with no feedback (left), SR_ion (centre), and SR_los (right), but with clouds of median number density ≈ 100 cm^{-3} overplotted. These clouds were identified using a friends of friends algorithm with a nearest neighbour distance of 0.55 pc.

expected, the significance of the cloud disruption is lower in this run.

We show the global cloud properties over time in Figure 4.2 for the same simulations and cloud definitions as in Figure 4.1. The peak difference in cloud numbers between the no feedback and photoionisation runs for all cloud densities is around a factor of 2. This difference is not produced solely by breaking up of clouds but also by the formation of new clouds under pressure from HII regions. Figure 4.2 also shows that photoionisation causes additional gas to be agglomerated into clouds, both newly formed and pre-existing. This effect is far more pronounced in the densest objects. At the peak in both the SR_ion and SR_50% runs there is approximately twice as much gas in clumps (clouds of number density 1000 cm^{-3}). In the SR_ion

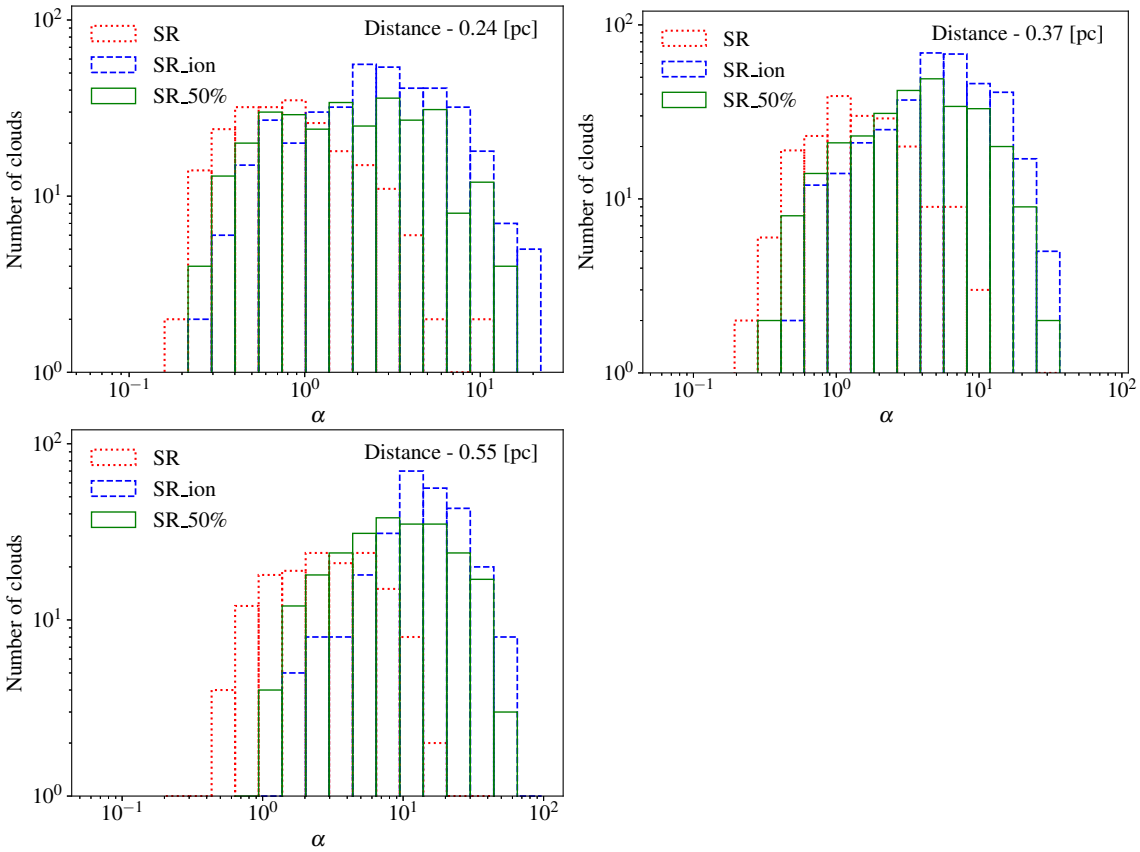

Figure 4.4. The distribution of the kinetic to gravitational potential energy ratio is shown for all clouds of more than 100 particles (100 $M_\odot$ in these cases). To be considered part of a cloud, a particle must have a number density of at least 50 cm^{-3} and be within the minimum distance of at least one other particle within the cloud. Top, middle and bottom panels correspond to the panels in Figures 4.1 and 4.2. The fiducial runs with and without photoionisiation are plotted along with the 50% SFE run.

runs the total gas fraction peaks at around 3.3 Myr, the peak in the number of clouds is at around 4.2 My. The SR_50% run shows very similar behaviour but it is delayed by around 1 Myr.

In Figure 4.3 we overplot the clumps found with the 0.55 pc distance criteria in the SR, SR_ion and SR_los runs. In the no feedback model, there is clearly one very massive cloud, whereas, with ionisation, this cloud has been broken up into multiple structures. Furthermore for the cases with ionisation - particularly the SR_los run - we see clumps in new regions often in spurs off the spiral arm. Again this is likely due to the impact of photoionisation compressing these regions. We find minimal difference between the statistical properties of the SR_ion and SR_los runs and conclude that for an isolated section of spiral arm, long range ionisation is not critical. We use line of sight limits that are as short as possible, while still being comfortably larger than the typical initial separations of clumps and clouds

for each set of initial conditions. Emerick et al. (2018) examined the importance of long-range ionisation in low-mass dwarf galaxies, they conclude that long-range ionisation is particularly important in driving galactic winds.

Global galaxy simulations indicate that stellar feedback is an important source of kinetic energy in the ISM and necessary for preventing GMCs from becoming too gravitationally dominated (Dobbs et al., 2011). In Figure 4.4 we investigate whether the ionisation changes the ratio of the kinetic to gravitational energy (i.e. virial parameter α) in the clumps and clouds in our simulations. Observers typically calculate the virial parameter as,

$$\alpha = \frac{5\sigma_v^2 R}{GM}, \tag{4.1}$$

where σ_v is the velocity dispersion of the gas, R is the radius of the cloud, G is the gravitational constant, and M is the mass of the luminous gas. Since we are not comparing our values to observations it is simpler to calculate α directly. We normalise the gas particle velocities for each cloud and sum the resulting kinetic energies. We find the gravitational energy as the sum of the energy stored between each particle pair. This also means that we do not need to make an estimate of R for each of our clouds, although we should point out that for highly non-spherical clouds our values of α are poor approximations.

We show results for the distance criteria of 0.24 pc (top) i.e. smaller clumps, 0.37 pc (middle) and 0.55 pc (lower), which includes larger molecular clouds. As well as the SR and SR_ion simulations, we also include the 50% ionisation model, SR_50%. In all cases, we see that ionisation has a notable effect on the virial parameter of the clouds. The distribution of α shifts to higher values; the clouds and clumps with these high values may well be very transient. For the clumps (top panel Figure 4.4), there are still many bound objects in the cases with ionisation. However, for the clouds (bottom panel), the numbers of bound clouds are noticeably less with ionisation, and overall the clouds tend to be unbound. We find this is still true for the SR_50% simulation. Even though there is a smaller and perhaps more realistic amount of ionisation than is modelled in our fiducial case, this still has a significant impact on the gas.

We also consider the high resolution runs (HR and HR_ion) and we find that there are no significant statistical differences between these and the fiducial runs. We were only able to run the HR_ion simulation to 3.5 Myr due to the much higher computational expense.

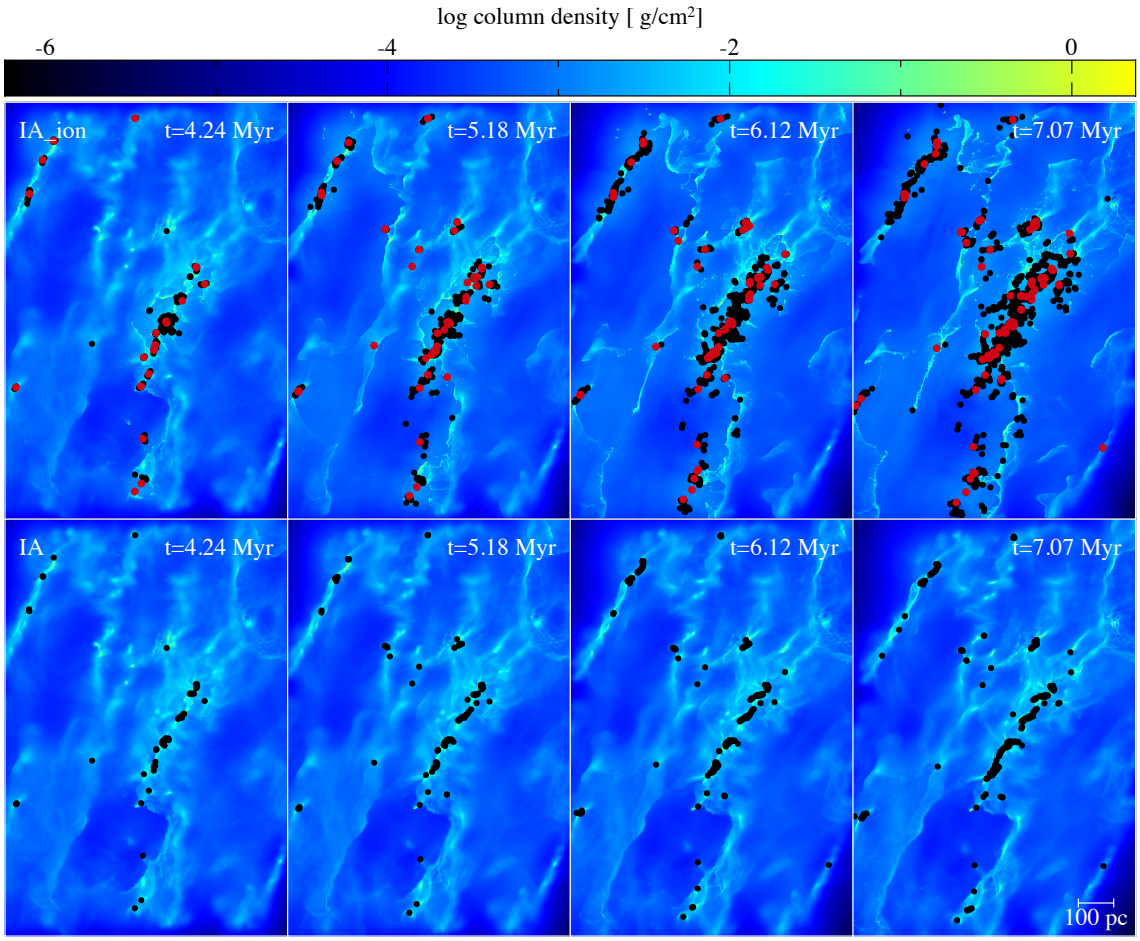

Figure 4.5. The column density is shown for the inter-arm region of the photoionisation run (top) and the no feedback run (bottom) over time. The frames start at 4.24 Myr when the first ionisation fronts are still fewer than 100 pc from their sources. Again, the ionisation appears to produce more sink particles, and sharper features in the gas, but this happens over longer timescales compared to the section of spiral arm. The larger red dots are ionising sink particles and the smaller black dots are non-ionising sink particles.

4.2 Comparisons with an inter-arm region

The inter-arm region evolves very differently in the presence of photoionising radiation, as shown in Figure 4.5. We again see the wider distribution of star forming regions, and, in this case, we can clearly see photoionisation causing a more filamentary structure in the SR_ion run.

In our spiral arm region (SR), all of the runs show that photoionisation accelerates star formation in the surrounding gas. Since a key difference between the IA and SR initial conditions is the separation of the star forming regions, it is interesting to explore this effect in these regions. In Figure 4.6 we plot the number of clouds, and total fraction of gas in clouds for the inter-arm region, as previously

presented in Figure 4.2 for the spiral arm region. We see increases in the total gas in clouds, number of clouds and star formation rates when photoionisation is included (IA_ion), however, not in the same proportions as in the spiral arm. In both the simulations with and without feedback (IA and IA_ion runs), the SFE has not begun to plateau after 10 Myr, whereas the SR_ion run has reached 90% of its final SFE by 7 Myr.

Duarte-Cabral & Dobbs (2016) explore the differences between arm and inter-arm clouds in very similar simulations to these, but lacking photoionisation, by analysing the simulations presented in Dobbs (2015). They find that while predominantly clouds are very similar in the arms and inter-arms, there are some variations. Of interest to this work, they find that the most filamentary clouds are found in the inter-arms and suggest gravitational shear as the main cause of this.

We see the same effect in our simulations, but notice how photoionisation further defines the shape of these filaments and increases their mean density. By comparison of Figures 4.2 and 4.5, we see a greater total increase in gas in clouds with feedback in the inter-arm runs relative to the arm runs, this additional dense gas is also longer lasting. The additional definition to the filaments seen in Figure 4.5 is unmistakable.

We compare velocity dispersions of GMCs between the IA, IA_ion, SR, and SR_ion runs at the times at which the total gas in clouds peaks for the runs with photoionisation (3.3 Myr for SR and 5.9 Myr for IA). We find that GMCs (clouds of median number density 1000 cm^{-3}) have higher velocity dispersions in the arms than inter-arms which, like Duarte-Cabral & Dobbs (2016), is in agreement with observations of M51 by Colombo et al. (2014) and within the Milky Way by Rigby et al. (2019); this difference is reduced in the feedback runs. We notice similar behaviour in clumps although it is less pronounced and reduced less by photoionisation.

While the increase in total gas in clouds in the IA_ion run is greater than the SR_ion run and the number of clumps is increased by a similar amount, the effect on the SFR is much less stark. The peak in the SFR in the feedback case being only 1.3 times higher than without feedback. The SFR per unit area varies between 10 and 20 times smaller in the inter-arm region compared to the spiral arm over time.

Simulating an inter-arm region with supernovae in addition to photoionisation will be particularly interesting owing to the longer time-scale of gas depletion and limited dense gas to absorb the feedback.

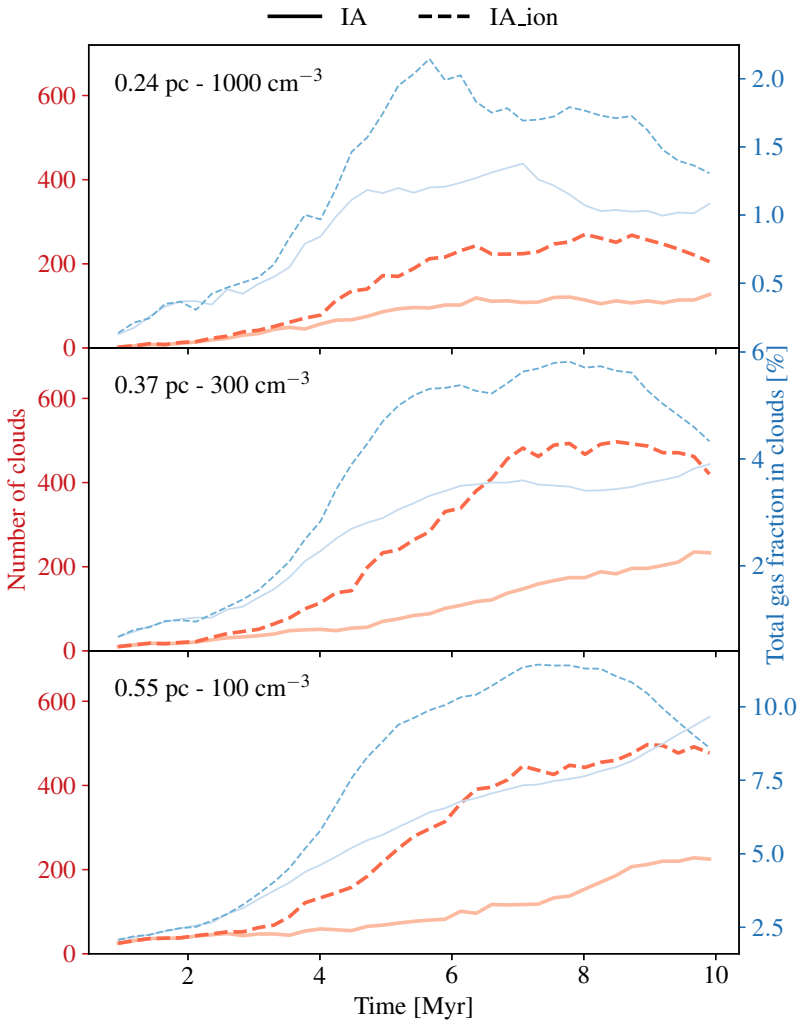

Figure 4.6. The evolution of the number of clouds (thicker red) and the gas fraction contained in them (thinner blue) is shown for the inter-arm region. This is equivalent to Figure 4.2 for the spiral arm region. The evolution of the gas and clouds is similar to the spiral arm case, but occur over a longer timescale.

4.3 Feedback and the phases of the ISM

Next we examine the distribution of this dense gas by considering the probability distribution functions (PDFs) for all gas particles (Figure 4.7) and for gas particles in clouds (Figure 4.8). In Figure 4.7 (top panel) we can see that gas at number densities $> 10^4$ cm^{-3} is 2 to 10 times more prevalent with photoionisation. This is, in part, because gas will not form sinks until higher densities as a result of the increased kinetic and thermal energy in clouds (Section 2.2.12). It is also due to compression by HII regions.

In the bottom panel of Figure 4.7 we see the significant shift of gas from the cold neutral medium (CNM) to the warm neutral medium (WNM) as a result of

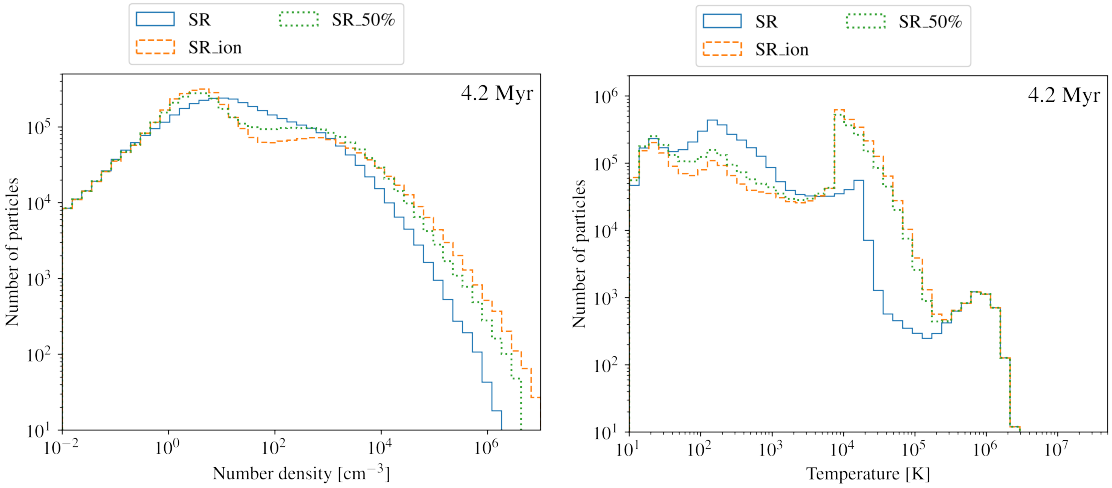

Figure 4.7. Left panel: density PDF for all gas particles in three simulations at 4.2 Myrs. Right panel: the equivalent temperature PDF. This is around the time that both dense gas and SF peak in runs with photoionisation.

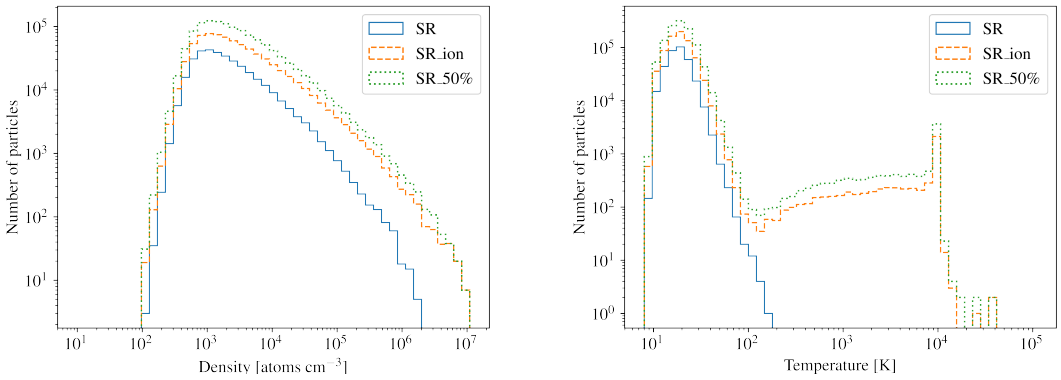

Figure 4.8. As Figure 4.7, except only considering gas in clouds, as defined by the middle separation criterion, 0.37 pc. the equivalent plots for the 0.24 and 0.55 pc cloud criteria present the same overall picture.

photoionisation. Both panels show that the hottest most diffuse gas is unaffected by photoionisation.

The top panel of Figure 4.8 is largely just a truncated version of the equivalent plot in Figure 4.7. However, a key difference is that in the SR_50% run while there is less dense gas in total, there is more associated with clumps and clouds. This could suggest why reducing the Lyman flux by 50% does not reduce the accelerated and displaced SF (Section 3.2.2) by a the same amount. The lower ionising flux does not break up as many clouds but still causes compression throughout a more densely packed group of clouds.

Looking at the temperature distribution of cloud gas (Figure 4.8 bottom panel)

shows a clear difference to the all-gas picture. Many of the clouds in simulations with photoionisation have dense warm envelopes making up a small fraction of the total cloud mass. It is likely that the majority of the gas in these envelopes is at least partially ionised although we have not, as yet, explored the radial profile of clouds. The existence of such dense, ionised gas is of great interest, is it able to recombine and cool, or does it remain ionised and warm the cloud while compressing it?

Chapter 5

Simulations with supernovae

In this chapter we consider the effects of adding SNe to two of the simulations presented in Chapters 3 and 4 – one with and one without photoionising feedback. As the fiducial simulation, the SR run is the obvious choice for considering the effects of SNe without any early onset feedback. For the case with photoionisation we have chosen the SR_50% run since we consider the number of massive stars to be the better approximation. This means that this chapter focuses on just four simulations referred to as follows in this chapter.

1. **No feedback** (previously SR)
2. **Photoionisation** only (previously SR_50%)
3. **SNe** only
4. **Both** forms of feedback

The temperature cross-section at the galactic mid-plane for these four simulations shows clear differences in the way SNe affect the wider ISM; Figure 5.1 shows this cross-section at 6.6 Myr. In the SNe only case the SNe sites cool rapidly leaving very little evidence. However, in the runs with both forms of feedback superbubbles form around the sites of SNe and the gas is unable to cool.

5.1 Considerations for comparisons

One point to consider when comparing simulations 2 and 4 is that 2 was run before the sink sub-grid model was adapted to track massive star ages for SNe. This means that photoionising sinks continue to emit the Lyman flux of massive stars beyond their lifetimes. In run 4, however, the Lyman flux of sinks is reduced appropriately after each SN event. While this is an undesirable complication for comparisons, the 460,000 core-hours required to re-run simulation 2 mean that doing so was not

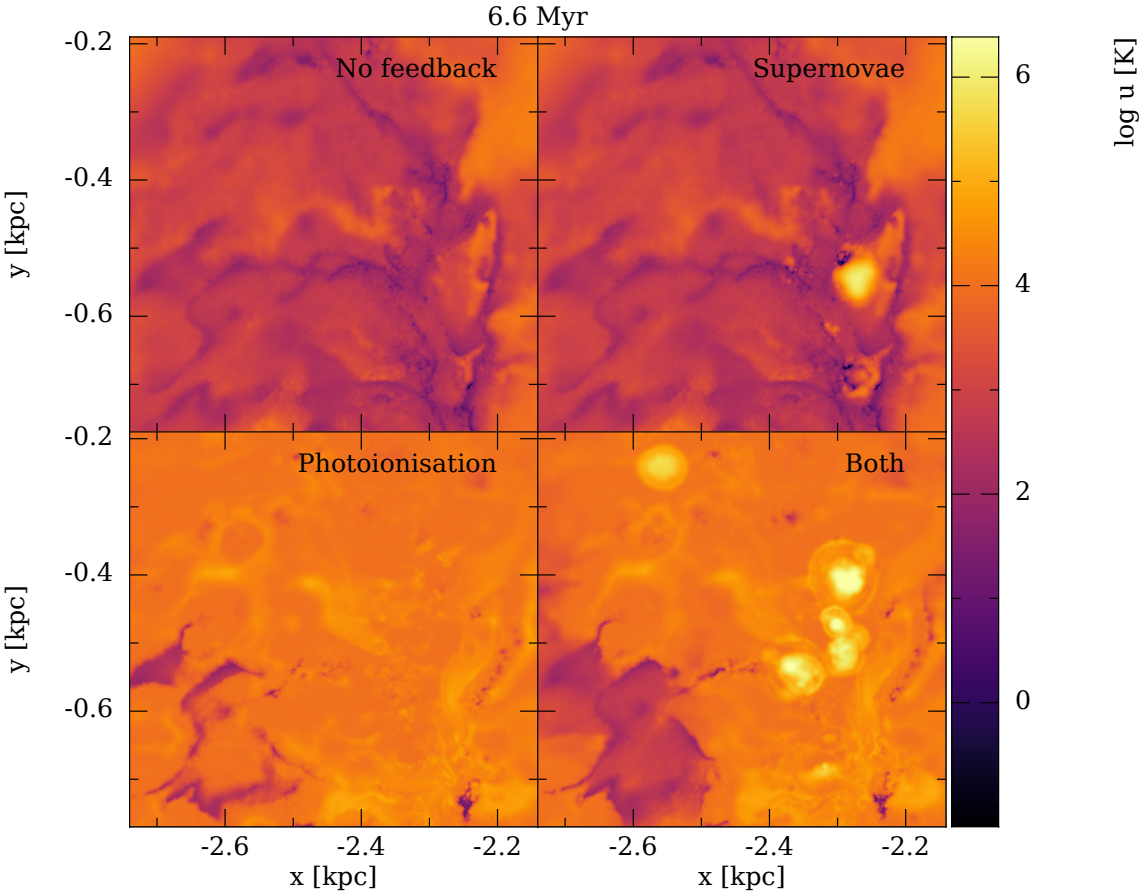

Figure 5.1. Temperature cross-section for runs with and without feedback. Both the right hand panels have been subjected to around 20 SNe.

possible for this thesis. It is also is difficult to justify for future work.

It is also important to consider the different environments in which the SNe occur in simulations 2 and 4. The ambient density in which SNe occur varies by 4 dex in run 2 and 7 dex in run 4. We show the distribution of densities at sites of SNe in Figure 5.2. As is expected the SNe in the run with photoionisation occur at much lower densities on average. Although the SN in the densest environment does occur in this simulation. This is likely to be the result of sink particles motion relative to gas.

The high densities at which SN occur in the run without photoionisation reflect the beginning of stellar feedback in the simulation. If the simulation were to progress further it would be likely that increasing numbers of SNe occured in less dense regions, as seen by Gatto et al. (2017). Gatto et al. (2015) present a scheme in which they modify the SN prescription depending on the ambient density. In high density regions, where the SN is unresolved, they use a momentum driven approach similar to our own, however, in low density regions they inject only thermal energy

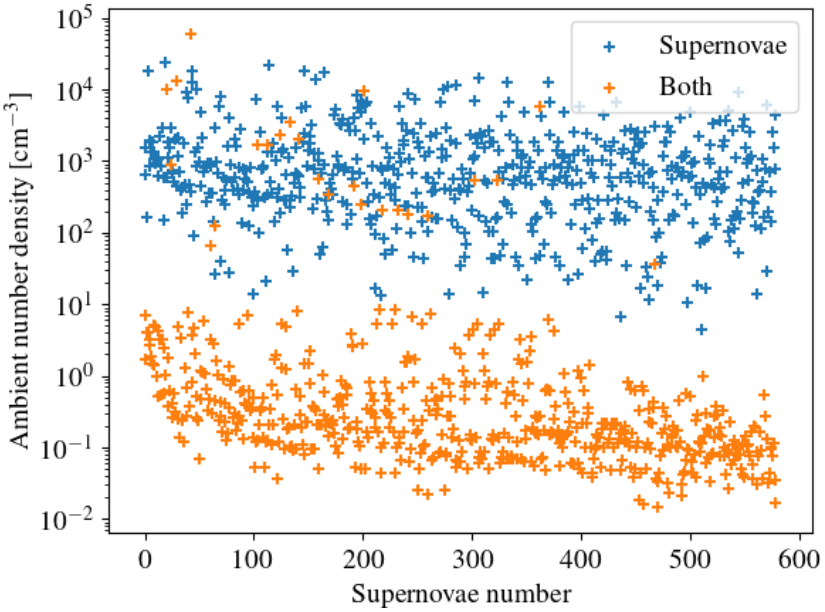

Figure 5.2. Ambient density at sites of SNe for the first 580 SNe to occur in runs 3 and 4, arranged by the order in which they occur. The blue points are for the run without pre-SN feedback and the orange for the run with both forms of feedback

sine the Sedov-Taylor phase can be resolved.

The wide range of ambient densities tests the SNe model (Section 2.3.5) energy injection balance. While this is something that needs to be improved in the future, it is a reasonable starting point. The SNe occurring in denser gas inject a higher fraction of kinetic energy, which is in line with the snowplough phase. However, those occurring in the low density gas receive mostly thermal energy since the low densities mean the Sedov-Taylor phase lasts longer.

5.2 Gas phases

The distribution of gas temperatures is the most intuitive way to compare simulations to the observed phases of the ISM. Figure 5.3 shows temperature PDFs at four epochs in the each of the four simulations, it can be compared with the right panel of Figure 4.7. The progression through time shows how the SNe alone have very little effect on the gas. However, when comparing the runs with photoionisation there are some very clear differences. Maximum gas temperatures are increased by an order of magnitude.

The differences at lower temperatures (10^2 to 10^4 K) are highly unlikely to be

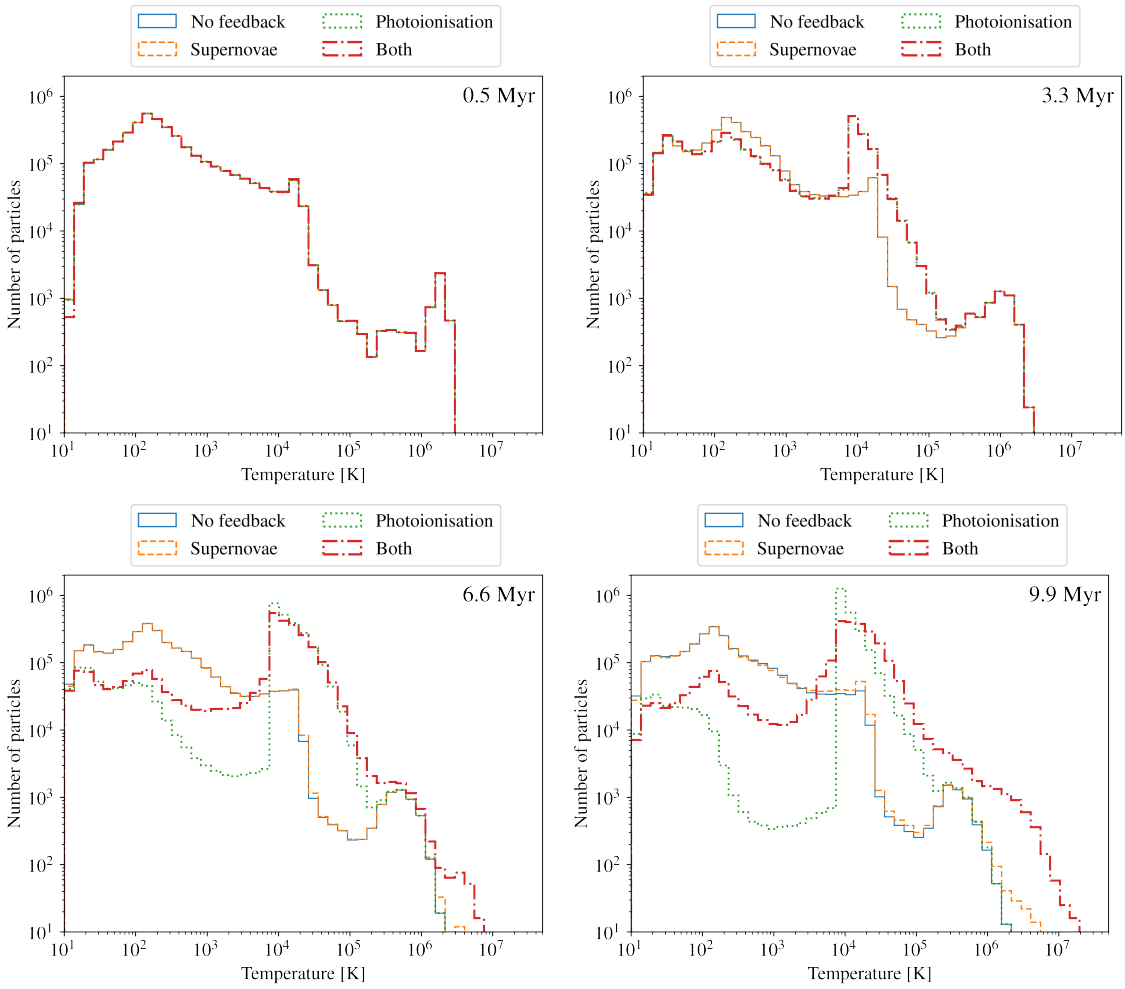

Figure 5.3. Temperature PDFs for all gas particles at four timestamps in the simulations. 0.5 Myr shows the inherited PDF from the galaxy scale simulations (Dobbs & Pringle, 2013). 3.3 Myr is before the first SN and shows the initial impact of photoionisation. 6.6 Myr shows significant photoionisation and the effect of a few tens of SNe. After 9.9 Myr around 1000 SNe have occurred.

a 'real' effect. The large paucity of gas at later times in the photoionisation run (Figure 4.7) is the result of higher Lyman flux, which results from not tracking stellar lifetimes in that simulation (Section 5.1). This large difference does highlight the very high Lyman fluxes of the most massive and shortest lived stars in the simulations, and also the importance of approximating the number of massive stars as accurately as possible.

The energy injected by SNe is resisted very effectively by dense gas, it is channelled into low density regions and or creates them if they do not already exist. This is the same behaviour seem by other authors in simulations with both photoionisation (Walch & Naab, 2015; Lucas et al., 2020) and stellar winds (Rogers & Pittard, 2013).

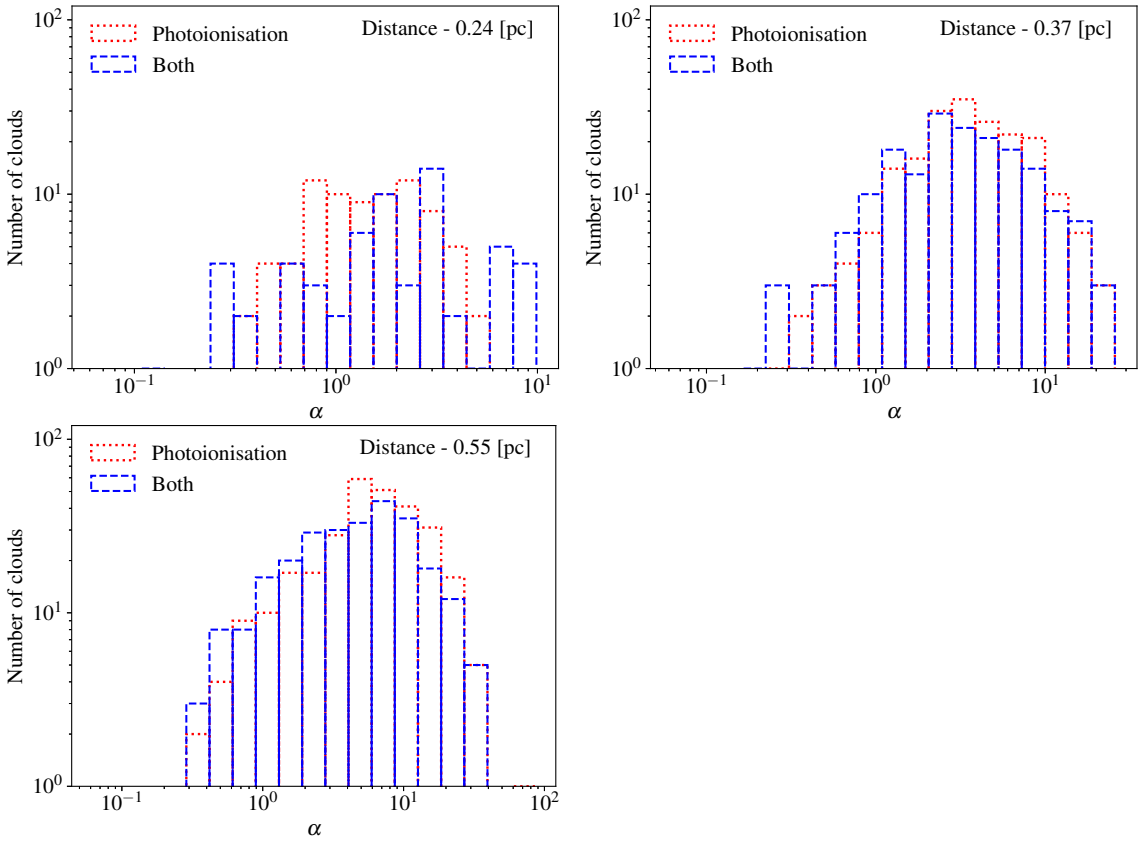

Figure 5.4. Histograms of virial parameter for clouds of the 3 definitions used throughout Chapter 4, at 7.5 Myr.

5.3 Cloud properties

We find the clouds using the same friends of friends algorithm used in Chapter 4. When comparing the virial parameter we find very little difference with and without SNe. In the case of the no photoionisation runs, SNe have almost no effect on the virial parameter of clouds on these timescales. In the runs with feedback there is a small impact on clouds defined by the shortest separation criterion, 0.24 pc, with a handful of clouds having a higher virial parameter as a result of SNe.

The affect of SNe vary a great deal depending on whether the ISM has already been affected by photoionisation. Gas heated by SNe without previous feedback is able to cool quickly around all but one cluster. However, when SNe occur inside HII regions the lower density gas is unable to cool and creates large superbubbles at temperatures above 10^6 K. Over time these superbubbles begin to overlap and begin to form a network of $> 10^6$ K gas.

Chapter 6

Conclusions and future work

In this thesis we have investigated the impact of two feedback mechanisms on spiral arm star forming regions extracted from whole galaxy scale simulations (Dobbs & Pringle, 2013). We have compared the effects of feedback on star formation (SF), the interstellar medium (ISM), and giant molecular clouds (GMCs) to simulations without feedback to isolate the individual importance of photoionisation and supernovae (SNe) and understand how they work in concert. In this chapter we will first summarise the conclusions we have made from this work (Sections 6.1 and 6.2) then we will lay out plans for improvements to methods and future simulations (Section 6.3).

6.1 Photoionisation

In Chapters 3 and 4 we presented comparisons between simulations, with and without photoionising feedback, of 0.5 kpc^2 regions extracted from galaxy scale simulations. Our simulations contain a number of molecular clouds, and photoionising feedback is able to affect the surrounding gas and neighbouring clouds. We are also able to study the behaviour of ionisation in a region with many clouds, i.e. the spiral arm, versus a relatively low density inter-arm region. We explore the effects of photoionisation not just on individual clouds forming stars, but also their neighbours which may or may not be forming stars themselves.

We focus predominantly on three cases: no feedback, photoionising feedback and a prescription with half the total Lyman flux. We find that the interactions between ionisation fronts and neighbouring clouds are highly influential on the star formation rate, cloud distribution and cloud dynamics, but only minimally affect the overall star formation efficiency. In particular we find that:

1. Star formation is accelerated by photoionising radiation largely due to the pressure of HII regions on clumps/clouds that would not otherwise form stars for some time, often at large distances from sites of star formation in runs without feedback. This process occurs over timescales of several Myr. After this period of acceleration, star formation decreases rapidly because much of the dense gas is used up. Thus we find that ionisation produces a significant amount of triggered star formation in our simulations.
2. The number of cluster sink particles is nearly doubled by the effects of photoionisation, but the accretion on to them is much less than in the no feedback case. The latter seems in basic agreement with simulations by Gatto et al. (2017) who find that winds reduce accretion on to clusters and limit their mass and Zamora-Avilés et al. (2019) who find the same for photoionisation.
3. Long range ionisation causes the formation of clouds at very high distances (hundreds of pc) from the nearest ionising sink particle. However, these clouds contain only a tiny proportion of the total star formation. When limiting the maximum distance over which ionisation can act, we see that reducing the range of ionising photons to 100 pc does not modify the global statistical properties of gas and star formation.
4. Photoionisation increases both the number of clouds and clumps and to a lesser extent the total gas fraction within clouds. This increased fraction of gas in clouds indicates that fragmentation is not the only cause of the increased number of clouds, but that new clouds are being created, or at least having their collapse accelerated, by pressure that results from photoionisation.
5. Including photoionising feedback produces stellar clusters which are less compact, and heavily reduces the fraction of bound clusters relative to the no feedback case.
6. In interarm regions, cloud evolution and star formation follow a similar pattern to the spiral arm region but on a larger scale and with a smaller increase in star formation. Although the distances between star forming clumps are larger in the interarm regions, this is offset by the lower densities between clouds, allowing ionisation fronts to travel large distances.
7. Final star formation efficiencies are only modestly affected by photoionisation, however, the conversion of gas into stars occurs in around half the time in the runs with photoionisation.

Compared to previous work, the ionisation has a greater effect of enhancing star formation in our simulations, although in common with previous simulations, we also

see ionisation breaking up and disrupting the clouds. One of the main reasons for the increased star formation is that our clouds are not isolated, and unlike previous work (Dale et al., 2014; Geen et al., 2016; Ali & Harries, 2019; Zamora-Avilés et al., 2019), the feedback does not escape into an empty region, but impacts other material. We do see a large decrease in star formation, but only after a few Myr due to much of the dense gas being used up.

6.2 Supernovae

In Chapter 5 we presented two additional simulations in which SNe occur at the end of each massive star's lifetime – one with and one without photoionisation. We compare each of these to a corresponding simulations without SNe from Chapters 3 and 4. The simulations progress for 10 Myr and the effect of SNe on SF on this timescale is negligible. The dense gas is also affected very little.

The diffuse ISM, however, is very different in the runs with SNe, particularly in the run with photoionisation as well. The gas in HII regions heated by the supernovae is unable to cool and large volumes of ionised gas are heated to 10^6 K. Over several Myr these regions begin to connect forming a network of hot ionised gas. These findings are in agreement with other authors (Rogers & Pittard, 2013; Walch & Naab, 2015; Lucas et al., 2020) who find that energy from SNe is able to propagate much further if channels have been created by earlier feedback.

6.3 Future work

In this section we will discuss some of the limitations of the work presented in this thesis and ways in which they can be addressed in the future. We will also discuss ideas for future simulations and further analysis of the simulations presented here.

6.3.1 Cluster sink particles

Sink particles are a necessary evil in the world of numerical simulations of star formation. They have their drawbacks when used as a proxy for stars or star systems, and yet allow for the simulation of entire clouds by approximating the behaviour of stars. They are even less well suited to represent clusters; the major issue being that clusters, especially those in the early stages of SF, contain high fractions of gas.

In our main simulations with photoionisation, the cluster sink particles assume star formation efficiencies (SFEs) of 50% and 100%, with hindsight, both are high

considering that the sinks formed are on scales of small clouds rather than dense cores or even clumps. When using the assumed sink SFE of 50%, gas inside the sinks is ignored. This gas would likely be very effective at shielding neighbouring gas around the sinks from Lyman flux.

Continued improvement of the cluster sink particle sub-grid model is a major focus for future work. On the simplest level this means identifying the best ratio of star to gas mass in the sink particles. The next consideration is how to evolve gas inside sinks. Properties of gas in the sub-grid cannot be found by interpolation, as they are for gas particles.

Cluster sink particles should ideally exert pressure on their surroundings. Traditional sink particles do have boundary conditions but they do not exert pressure (Bate et al., 1995). Again this leads to the need to approximate gas properties within sink particles.

If a cluster sink particle is to be an accurate sub-grid model of a star forming clump or even a small GMC it needs to emit feedback as such, rather than as the sum of the cluster within. One way to approach this would be to analyse the matter and radiation that escapes from a range of single cloud simulations and build a catalogue of clouds/clusters. Similar catalogues exist, such as the galaxy synthesis models in STARBURST99 (Leitherer et al., 1999), such tools provide the basis for sub-grid models for the star formation community on all scales. The community has already performed many simulations that could potentially be post-processed to quantify cloud ejecta.

6.3.2 Simulation scale and duration

Within these simulations only a small fraction of the massive stars underwent SNe. To better explore the effects of SNe on the wider ISM it would be preferable to run simulations for longer time periods, which in turn requires larger regions.

As the simulations evolve there is a lack of gas flowing into the spiral arm due to the limited extent of the initial conditions. At the start of the simulations there are no massive stars and hence no feedback. This also means that the first SNe does not occur until over 4 Myr have elapsed. In single cloud simulations this is not a problem, but allowing the ISM to evolve without any form of feedback for so long is not ideal.

For running simulations over longer time scales it is also necessary to ensure that gas in the spiral arm is replenished. Dobbs (2015) achieve this by selecting a box defining a spiral arm section and tracing the contained smoothed particle

hydrodynamics (SPH) particles back through 30 Myr. When evolved these initial conditions allow the spiral arm to be constantly replenished.

6.3.3 Pre-population

In reality, there would be a population of ionising stars at the outset of our simulations which are immediately affecting the gas via feedback. Inclusion of these is likely to avoid the large peak in star formation seen here, and again lead to a decrease in the star formation earlier in the simulations.

This could be done by determining sites of star formation through post-processing of the galaxy scale simulations. The extracted initial conditions could then be pre-populated with cluster sinks containing massive stars of known ages.

6.3.4 Compressed clouds observational signatures

The increased cloud mass in the simulations presented in this thesis raises some interesting questions. So far we have shown that some clouds on all scales have envelopes of warm, non-molecular, and at least partially ionised gas at high densities. Further analysis of the cloud profiles will allow for us to understand how many clouds in our simulations have these envelopes, and what their exact ionised fraction is. If an ionised, dense gas envelope is a common feature of translucent clouds this could potentially be something to look for in observations of star forming regions.

6.3.5 Stellar winds

We are currently developing a stellar winds module for SPHNG and will use it to compare the effects of winds with photoionisation on the same scale as this work. It will also be useful for higher resolution single cloud simulations, as part of the goal to improve the way in which cluster sink particles emit feedback.

Bibliography

Ali A. A., Harries T. J., 2019, MNRAS, 487, 4890

Ali A. A., Harries T. J., Douglas T. A., 2018, MNRAS, 477, 5422

Alves J., Lombardi M., Lada C. J., 2007, Astron. Astrophys., 462, L17

Anderson L. D., Bania T. M., Balser D. S., Cunningham V., Wenger T. V., Johnstone B. M., Armentrout W. P., 2014, ApJS, 212, 1

André P., Di Francesco J., Ward-Thompson D., Inutsuka S.-i., Pudritz R. E., Pineda J., 2014, in Beuther H., Klessen R. S., Cornelis P. D., Henning T. K., eds, Protostars Planets VI. University of Arizona Press, Tucson, pp 27–52

Arce H. G., Mardones D., Corder S. A., Garay G., Noriega-Crespo A., Raga A. C., 2013, ApJ, 774, 39

Baba J., Morokuma-Matsui K., Saitoh T. R., 2017, MNRAS, 464, 246

Baczynski C., Glover S. C., Klessen R. S., 2015, MNRAS, 454, 380

Baldwin J. A., Ferland G. J., Martin P. G., Corbin M. R., Cota S. A., Peterson B. M., Slettebak A., 1991, ApJ, 374, 580

Bally J., 2016, ARA&A, 54, 491

Barnes J., Hut P., 1986, Nature, 324, 446

Bate M. R., Burkert A., 1997, MNRAS, 288, 1060

Bate M. R., Bonnell I. A., Price N. M., 1995, MNRAS, 277, 362

Bate M. R., Bonnell I. A., Bromm V., 2003, MNRAS, 339, 577

Beals C. S., 1936, MNRAS, 96, 661

Bending T. J. R., Dobbs C. L., Bate M. R., 2020, MNRAS, 1691, 1672

Benjamin R. A., et al., 2003, Publ. Astron. Soc. Pacific, 115, 953

Benz W., 1990, in Buchler J. R., ed., Numerical Modelling of Nonlinear Stellar Pulsations: Problems and Prospects. Kluwer, Dordrecht, p. 269

Benz W., Bowers R., Cameron A., Press W.H. 1990, ApJ, 348, 647

Berger M. J., Colella P., 1989, Rev. Française Sociol., 82, 64

Bergin E. A., Hartmann L. W., Raymond J. C., Ballesteros-Paredes J., 2004, ApJ, 612, 921

Bertoldi F., 1989, ApJ, 346, 735

Bigiel F., Leroy A., Walter F., Brinks E., de Blok W. J. G., Madore B., Thornley M. D., 2008, AJ, 136, 2846

Binney J., Tremaine S., 2008, Galactic dynamics. Princeton University Press, Princeton

Bisbas T. G., et al., 2015, MNRAS, 453, 1324

Black J. H., Dalgarno A., 1976, ApJ, 203, 132

Blitz L., 1993, in Levy E., Lunine J. I., Bania T. M., eds, Protostars Planets III. University of Arizona Press, Tucson, p. 125

Braine J., Rosolowsky E., Gratier P., Corbelli E., Schuster K. F., 2018, A&A, 612, A51

Bressert E., et al., 2010, MNRAS, 409, 54

Bryan G. L., et al., 2014, Astrophys. Journal, Suppl. Ser., 211

Castor J. I., Abbot D. C., Klein R. I., 1975, ApJ, 195, 157

Chabrier G., 2003, ApJ, 586, 133

Chevance M., et al., 2020, MNRAS, 493, 2872

Churchwell E. D., et al., 2009, Publ. Astron. Soc. Pacific, 121, 213

Cioffi D. F., Mckee C. F., Bertschinger E., 1988, J. Chem. Inf. Model., 334, 252

Clark B. G., 1965, ApJ, 142, 1398

Colombo D., et al., 2014, ApJ, 784, 3

Colombo D., Rosolowsky E., Ginsburg A., Duarte-Cabral A., Hughes A., 2015, MNRAS, 454, 2067

Colombo D., Rosolowsky E., Ginsburg A., Duarte-Cabral A., Hughes A., 2016, SCIMES: Spectral Clustering for Interstellar Molecular Emission Segmentation (ascl:1609.006)

Courant R., Friedrichs K., Lewy H., 1928, Math. Ann., 100, 32

Cox D. P., Gomez G. C., 2002, ApJS, 142, 261

Cox D. P., Smith B. W., 1974, ApJ, 189, L105

Cuppen H. M., Walsh C., Lamberts T., Semenov D., Garrod R. T., Penteado E. M., Ioppolo S., 2017, Space Sci. Rev., 212, 1

Dale J. E., Bonnell I. A., Whitworth A. P., 2007a, MNRAS, 375, 1291

Dale J. E., Ercolano B., Clarke C. J., 2007b, MNRAS, 382, 1759

Dale J. E., Ercolano B., Bonnell I. A., 2012, MNRAS, 427, 2852

Dale J. E., Ercolano B., Bonnell I. A., 2013, MNRAS, 430, 234

Dale J. E., Ngoumou J., Ercolano B., Bonnell I. A., 2014, MNRAS, 442, 694

Dale J. E., Haworth T. J., Bressert E., 2015, MNRAS, 450, 1199

Dalgarno A., Mccray R. A., 1973, ApJ, 181, 95

Dalgarno A., Roberge W. G., 1979, ApJ, 233, L25

Dalla Vecchia C., Schaye J., 2008, MNRAS, 387, 1431

Dame T. M., Hartmann D., Thaddeus P., 2001, ApJ, 547, 792

De Avillez M. A., Breitschwerdt D., 2005, Astron. Astrophys., 436, 585

Deharveng L., Zavagno A., Caplan J., 2005, Astron. Astrophys., 433, 565

Dehnen W., 2001, MNRAS, 324, 273

Dickey J. M., J L. F., 1990, ARA&A, 28, 215

Dobbs C. L., 2015, MNRAS, 447, 3390

Dobbs C. L., Pringle J. E., 2013, MNRAS, 432, 653

Dobbs C. L., Bonnell I. A., Pringle J. E., 2006, MNRAS, 371, 1663

Dobbs C. L., Glover S. C. O., Clark P. C., Klessen R. S., 2008, MNRAS, 389, 1097

Dobbs C. L., Burkert A., Pringle J. E., 2011, MNRAS, 417, 1318

Dobbs C. L., Pringle J. E., Burkert A., 2012, MNRAS, 425, 2157

Domínguez J. M., Crespo A. J. C., Gómez-Gesteira M., Marongiu J. C., 2011, Int. J. Numer. Methods Fluids, 67, 2026

Draine B. T., 2011, Physics of the Interstellar and Intergalactic Medium. Princeton University Press

Draine B. T., Bertoldi F., 1996, ApJ, 168, 269

Duarte-Cabral A., Dobbs C. L., 2016, MNRAS, 458, 3667

Dunne B. C., Chu Y.-H., Chen C.-H. R., Lowry J. D., Townsley L., Gruendl R. A., Guerrero M. A., Rosado M., 2003, ApJ, 590, 306

Elmegreen B. G., 2000, ApJ, 530, 277

Elmegreen B. G., Lada C. J., 1977, ApJ, 214, 725

Emerick A., Bryan G. L., Low M.-M. M., 2018, Astrophys. J. Lett., 865, L22

Ewen H. I., Purcell E. M., 1951, Nature, 168, 356

Feddersen J. R., Arce H. G., Kong S., Shimajiri Y., Nakamura F., Hara C., Sasaki K., Kawabe R., 2018, ApJ, 862, 121

Fehlberg E., 1969, NASA Technical Report R-315, Low-order Classical Runge-Kutta Formulas with Stepsize Control and their Application to some Heat Transfer Problems. Washington, USA

Field G. B., Goldsmith D. W., Habing H. J., 1969, ApJ, 155, L149

Filippenko A. V., 1997, ARA&A, 35, 309

Finkbeiner D. P., 2003, Astrophys. Journal, Suppl. Ser., 146, 407

Fryxell B., et al., 2000, ApJS, 131, 273

Gatto A., et al., 2015, MNRAS, 449, 1057

Gatto A., et al., 2017, MNRAS, 466, 1903

Gavagnin E., Bleuler A., Rosdahl J., Teyssier R., 2017, MNRAS, 472, 4155

Gazol A., Vázquez-Semadeni E., Sánchez-Salcedo F. J., Scalo J., 2001, ApJ, 557, L121

Geen S., Hennebelle P., Tremblin P., Rosdahl J., 2016, MNRAS, 463, 3129

Geen S., Watson S. K., Rosdahl J., Bieri R., Klessen R. S., Hennebelle P., 2018, MNRAS, 481, 2548

Geen S., Pellegrini E., Bieri R., Klessen R., 2020, MNRAS, 492, 915

Gil de Paz A., et al., 2007, ApJS, 173, 185

Gingold R. A., Monaghan J. J., 1977, MNRAS, 181, 375

Gingold R. A., Monaghan J. J., 1982, J. Comput. Phys., 46, 429

Glover S. C. O., Mac Low M., 2007, ApJS, 169, 239

Goodman A. A., Rosolowsky E. W., Borkin M. A., Foster J. B., Halle M., Kauffmann J., Pineda J. E., 2009, Nature, 457, 63

Gorski K. M., Hivon E., Banday A. J., Wandelt B. D., Hansen F. K., Reinecke M., Bartelmann M., 2005, ApJ, 622, 759

Gould R. J., Salpeter E. E., 1963, ApJ, 138, 393

Grond J. J., Woods R. M., Wadsleyand J. W., Couchman H. M., 2019, MNRAS, 485, 3681

Haid S., Walch S., Seifried D., Wünsch R., Dinnbier F., Naab T., 2018, MNRAS, 478, 4799

Hartmann J., 1904, ApJ, 19, 268

Hartmann D., Burton W. B., 1997, Atlas of Galactic Neutral Hydrogen. Cambridge University Press

Haworth T. J., Harries T. J., 2012, MNRAS, 420, 562

Heiles C., 2001, ApJ, 551, L105

Helfer T. T., Thornley M. D., Regan M. W., Wong T., Sheth K., Vogel S. N., Blitz L., C-J Bock D., 2003, Astrophys. Journal, Suppl. Ser., 145, 359

Hennebelle P., Iffrig O., 2014, A&A, 570, A81

Heyer M. H., Morgan J., Schloerb F. P., Snell R. L., Goldsmith P. F., 1992, ApJ, 395, L99

Heyer M., Krawczyk C., Duval J., Jackson J. M., 2009, ApJ, 699, 1092

Hindson L., et al., 2016, Publ. Astron. Soc. Aust., 33, 20

Hopkins P. F., 2015, MNRAS, 450, 53

Hopkins P. F., Grudić M. Y., 2019, MNRAS, 483, 4187

Hosokawa T., Inutsuka S.-i., 2006, ApJ, 648, L131

Howard C. S., Pudritz R. E., Sills A., Harris W. E., 2019, MNRAS, 486, 1146

Hubber D. A., Batty C. P., McLeod A., Whitworth A. P., 2011, Astron. Astrophys., 529, A27

Huggins W., Miller W. A., 1864, Philos. Trans. R. Soc. London, 154, 437

Ikeuchi S., Habe A., Tanaka Y. D., 1984, MNRAS, 207, 909

Inutsuka S.-i., Inoue T., Iwasaki K., Hosokawa T., 2015, A&A, 580, A49

Jamet L., Stasińska G., Pérez E., Gonzalez Delgado R. M., Vílchez J. M., 2005, Astron. Astrophys., 444, 723

Janka H.-T., 2012, Annu. Rev. Nucl. Part. Sci., 62, 407

Jeans J. H., 1902, Philos. Trans. R. Soc. London Ser. A, 199, 1

Kahn F. D., 1954, Bull. Astron. Institutes Netherlands, 12, 187

Keeler J. E., 1899, ApJ, 9, 133

Kennicutt R. C., Evans II N. J., 2012, ARA&A, 50, 531

Kennicutt R. C., et al., 2003, Publ. Astron. Soc. Pacific, 115, 928

Kessel-Deynet O., Burkert A., 2000, MNRAS, 315, 713

Kim C. G., Ostriker E. C., Kim W. T., 2013, ApJ, 776, 1

Kim J.-G., Kim W.-T., Ostriker E. C., 2018, ApJ, 859, 68

Kitsionas S., Whitworth A. P., 2002, MNRAS, 330, 129

Koda J., et al., 2009, ApJ, 700, L132

Koyama H., Inutsuka S.-i., 2002, ApJ, 564, L97

Kramer C., Stutzki J., 1998, A&A, 329, 249

Krause M. G., et al., 2018, Astron. Astrophys., 619, 1

Kroupa P., 2001, MNRAS, 246, 231

Kruijssen J. M. D., 2012, MNRAS, 426, 3008

Krumholz M. R., 2018, MNRAS, 480, 3468

Krumholz M. R., Matzner C. D., 2009, ApJ, 703, 1352

Krumholz M. R., Thompson T. A., 2012, ApJ, 760

Krumholz M. R., Thompson T. A., 2013, MNRAS, 434, 2329

Krumholz M. R., Dekel A., McKee C. F., 2012, ApJ, 745, 69

Larson R. B., 1981, MNRAS, 194, 809

Leitherer C., et al., 1999, ApJS, 123, 3

Leroy A. K., Walter F., Brinks E., Bigiel F., de Blok W. J. G., Madore B., Thornley M. D., 2008, AJ, 136, 2782

Löhner R., 1987, Comput. Methods Appl. Mech. Eng., 61, 323

Low C., Lynden-Bell D., 1976, MNRAS, 176, 367

Lucas W. E., Bonnell I. A., Dale J. E., 2020, MNRAS, 493, 4700

Lucy L. B., 1977, AJ, 82, 1013

Maeda F., Ohta K., Fujimoto Y., Habe A., 2020, MNRAS, 493, 5045

Makino J., 1990, J. Comput. Phys., 88, 393

McCrea W. H., McNally D., 1960, MNRAS, 121, 238

McDowell M. R. C., 1961, Obs., 81, 240

McKee C. F., Ostriker J. P., 1977, ApJ, 218, 148

Meidt S. E., et al., 2015, ApJ, 806, 72

Miller G. E., Scalo J. M., 1979, ApJS, 41, 513

Miville-Deschênes M.-A., Murray N., Lee E. J., 2017, ApJ, 834

Monaghan J. J., 1985, Comput. Phys. Reports, 3, 71

Monaghan J. J., 1992, ARAA, 30, 543

Monaghan J. J., 1997, J. Comput. Phys., 136, 298

Morgan L. K., Thompson M. A., Urquhart J. S., White G. J., 2008, Astron. Astrophys., 477, 557

Muller C. A., Oort J. H., 1951, Nature, 168, 357

Murray N., 2011, ApJ, 729, 133

Nakamura F., et al., 2012, ApJ, 746

Nelson R. P., Langer W. D., 1999, ApJ, 524, 923

Öberg K. I., 2016, Chem. Rev., 116, 9631

Pineda J. E., Rosolowsky E. W., Goodman A. A., 2009, ApJ, 699, L134

Plaskett J. S., Pearce J. A., 1930, MNRAS, 90, 243

Pomarès M., et al., 2009, Astron. Astrophys., 494, 987

Portegies Zwart S. F., Verbunt F., 1996, A&A, 309, 179

Portegies Zwart S. F., Verbunt F., 2012, SeBa: Stellar and binary evolution (ascl:1201.003)

Press W., 1986, in Hut P., McMillan S., eds, Lecture Notes in Physics, Vol. 267, The Use of Supercomputers in Stellar Dynamics. Springer, Berlin, Heidelberg, p. 184

Price D. J., 2007, Publ. Astron. Soc. Aust., 24, 159

Price D. J., 2012, J. Comput. Phys., 231, 759

Price D. J., Monaghan J. J., 2007, MNRAS, 374, 1347

Price D. J., et al., 2018, Publ. Astron. Soc. Aust., 35

Raga A. C., Cantó J., Rodríguez L. F., 2012a, Rev. Mex. Astron. y Astrofis., 48, 149

Raga A. C., Cantó J., Rodríguez L. F., 2012b, MNRAS, 419, L39

Raskin C., Owen J. M., 2016, ApJ, 820, 102

Rees M. J., 1976, MNRAS, 176, 483

Rey-Raposo R., Dobbs C., Duarte-Cabral A., 2014, MNRAS, 446, L46

Rey-Raposo R., Dobbs C., Agertz O., Alig C., 2017, MNRAS, 464, 3536

Rigby A. J., et al., 2019, Astron. Astrophys., 632, A58

Rodríguez M., García-Rojas J., 2010, ApJ, 708, 1551

Rogers H., Pittard J. M., 2013, MNRAS, 431, 1337

Roman-Duval J., Jackson J. M., Heyer M., Rathborne J., Simon R., 2010, ApJ, 723, 492

Rosolowsky E., 2005, Publ. Astron. Soc. Pacific, 117, 1403

Rosolowsky E., Leroy A., 2006, Publ. Astron. Soc. Pacific, 118, 590

Rosolowsky E. W., Pineda J. E., Kauffmann J., Goodman A. A., 2008, ApJ, 679, 1338

Rosswog S., 2009, New Astron. Rev., 53, 78

Saitoh T. R., Makino J., 2009, ApJ, 697, L99

Salpeter E. E., 1955, ApJ, 121, 161

Sanford R. F., Merrill P. W., Wilson O. C., 1938, Publ. Astron. Soc. Pacific, 50, 58

Schaller M., Gonnet P., Chalk A. B., Draper P. W., 2016, in proceedings of the PASC conference. Association for Computing Machinery, Lausanne, Switzerland, p. 2

Schinnerer E., et al., 2019, The Messenger, 3, 36

Schoenberg I. J. 1946, Q. Appl. Math., 4, 45

Scoville N., Hersh K., 1979, ApJ, 229, 578

Sedov L. I., 1959, Similarity and Dimensional Methods in Mechanics. Academic press, New York

Seifried D., et al., 2017, MNRAS, 472, 4797

Seifried D., Walch S., Haid S., Girichidis P., Naab T., 2018, ApJ, 855, 81

Shu F. H., Adams F. C., Lizano S., 1987, ARA&A, 25, 23

Shull J. M., 1987, in Hollenbach D. H., Thronson Jr H. H., eds, Panel Discussion: Phases of the Interstellar Medium. Reidel, Dordrecht, p. 225

Snow T. P., Mccall B. J., 2006, ARA&A, 44, 367

Solomon P. M., Rivolo A. R., Barrett J., Yahil A., 1987, ApJ, 319, 730

Sormani M. C., Treß R. G., Klessen R. S., Glover S. C., 2017, MNRAS, 466, 407

Sousbie T., 2011, MNRAS, 414, 350

Spitzer L., 1978, Physical processes in the interstellar medium. Wiley-Interscience, New York

Springel V., 2010, MNRAS, 401, 791

Springel V., Yoshida N., White S. D., 2001, New Astron., 6, 79

Stahler S., 2004, The formation of stars. Wiley-VCH, Weinheim

Sternberg A., Hoffmann T. L., Pauldrach A. W. A., 2003, ApJ, 599, 1333

Strömgren B., 1939, ApJ, 89, 526

Taylor G., 1950, Proceedings of the Royal Society of London. Series A, Mathematical and Physical Sciences, 201, 192

Teyssier R., 2001, Astron. Astrophys., 385, 337

Toonen S., Nelemans G., Portegies Zwart S., 2012, Astron. Astrophys., 546, A70

Trumpler R. J., 1930, Publ. Astron. Soc. Pacific, 42, 214

Van Dishoeck E. F., 2018, in Cunningham M., Millar T., Aikawa Y., eds, Proc. Int. Astron. Union. No. 332. Cambridge University Press, UK, p. 3

Vázquez-Semadeni E., 2012, EAS Publ. Ser., 56, 39

VonNeumann J., Richtmyer R. D., 1950, J. Appl. Phys., 21, 232

Walch S., Naab T., 2015, MNRAS, 451, 2757

Walch S., Whitworth A., Bisbas T., Wünsch R., Hubber D., 2011, Proc. Int. Astron. Union, 270, 323

Walter F., Brinks E., De Blok W. J. G., Bigiel F., Kennicutt R. C., Thornley M. D., Leroy A., 2008, AJ, 136, 2563

Whitehouse S. C., Bate M. R., 2006, MNRAS, 367, 32

Whitehouse S. C., Bate M. R., Monaghan J. J., 2005, MNRAS, 364, 1367

Whitworth A. P., Bhattal A. S., Chapman S. J., Disney M. J., Turner J. A., 1994, A&A, 290, 421

Wild J. P., 1952, ApJ, 115, 206

Williams J. P., de Geus E. J., Blitz L., 1994, ApJ, 428, 693

Wilson R. W., Jefferts K. B., Penzias A. A., 1970, ApJ, 161, L43

Winkler P. F., Williams B. J., Reynolds S. P., Petre R., Long K. S., Katsuda S., Hwang U., 2014, ApJ, 781, A65

Zamora-Avilés M., et al., 2019, MNRAS, 487, 2200

Zavagno A., et al., 2010, Astron. Astrophys., 518, L81

Zinnecker H., Yorke H. W., 2007, ARA&A, 45, 139

van de Hulst H., 1945, Natuurkunde, 11, 210